Intelligent Power Assist Algorithms for Electric Bicycles

by

Xuan Fan

A dissertation submitted in partial satisfaction of the

requirements for the degree of

Doctor of Philosophy

in

Engineering-Mechanical Engineering

in the

Graduate Division

of the

University of California, Berkeley

Committee in charge:

Professor Masayoshi Tomizuka, Chair
Professor J. Karl Hedrick
Professor Xin Guo

Fall 2010

Intelligent Power Assist Algorithms for Electric Bicycles

by

Xuan Fan

Abstract

Intelligent Power Assist Algorithms for Electric Bicycles

by

Xuan Fan

Doctor of Philosophy in Engineering-Mechanical Engineering

University of California, Berkeley

Professor Masayoshi Tomizuka, Chair

This dissertation considers intelligent power-assist algorithm designs for electric bicycles. Traditional electric power-assist bicycles (EPBs) employ proportional power-assist strategy. The ratio is usually set to 1:1, which means that the motor will provide the same amount of assistive torque as the amount of the human's pedaling torque. This strategy is too rigid and does not consider the interaction between the bicycle, the human and the environment. Intelligent power-assist algorithms are needed to address such issues. In this dissertation, we focus on the uphill riding scenario, since it is the situation where the cyclist faces the most difficulties. The dynamic properties of electric bicycles will be studied and an appropriate model will be developed for intelligent power-assist algorithm design purposes. Two types of intelligent power-assist algorithms will be introduced to help the human ride uphill more easily. One is the robust disturbance observer (DOB) based power-assist algorithm, which can observe and compensate for the environmental disturbance that the bicycle system is subjected to during uphill riding. The robust DOB provides flexibility to the power assistance and within the motor's capability, it can make riding uphill feel like riding on the level ground. The other intelligent power-assist algorithm is based on repetitive control technique. The human's pedaling torque is repetitive by nature of the crankset's mechanical design. The pedaling torque reaches it local minimum and maximum twice during one complete pedal cycle. During uphill riding, the difference between the maximum torque and minimum torque is so large as to cause severe fluctuation in the torque profile, and, in turn, result in fluctuations in the velocity and

acceleration profiles. We call the fluctuant human torque input "nonuniform human input" and compensate for the fluctuation with a repetitive control based power-assist algorithm. Repetitive control designs in both the time domain and the pedal-angle domain are considered. An experimental EPB system was built to verify the effectiveness of these two types of algorithms. Details of the experimental setup will be introduced. Simulation and experimental results will be shown in this dissertation.

Contents

List of Figures

List of Tables

Chapter 1

Introduction

The history of motorized bicycles can be traced back to the latter part of the 19th century, according to the entry "motorized bicycle" in Wikipedia [4]. While early attempts had been made with steam engines to motorize tricycles and quadracycles, modern designs use electric motors on bicycles as a source of power supply. The emergence of electric bicycles has greatly enhanced human mobility. The added battery and motor can extend the moving range of a bicycle without exhausting the cyclist. Given the fact that electric bicycles can substitute motor vehicles for mid-range transportation needs with zero emission, they can be a viable solution to the world's energy crisis. The term "electric power-assisted bicycle (EPB)" refers to the kind of electric bicycles which have both the cyclist and the electric motor as the propelling torque supply, as opposed to the ones that have the motor as the only source of energy supply. EPBs are intended to assist the rider in pedaling, rather than to completely free him/her from pedaling. EPBs are the subject of this research in which different novel power-assist algorithms will be designed and implemented to help the human in uphill riding situations. The terms "electric power-assisted bicycle (EPB)" and "electric bicycle" will be used interchangeably in this dissertation.

Typical EPBs are equipped with a torque sensor to detect the rider's pedaling force, a speed sensor to detect the bicycle speed, an electric motor as the assistive power source, a battery as the power supply, a control unit, and other necessary devices and mechanisms for mixing the rider's torque and the motor torque. The control unit determines the amount of assist torque based on the rider's torque and the bicycle speed. Basic algorithms used in commercial EPBs set the motor's assistive torque

proportional to the rider's torque. However, these algorithms can not always achieve the desired comfort level of the cyclists. For example, proportional assistance may not suffice when a rider bikes up a steep slope.

This dissertation is dedicated to developing intelligent power-assist algorithms for EPBs in uphill riding condition. Intelligent power-assist algorithms are different from traditional EPB power-assist algorithms in that they can adaptively handle interactions between human, machine, and the environment. Two main foci of our research are environmental disturbance rejection, and non-uniform human input compensation. The rest of this dissertation is organized as follows: Section 1.1 introduces commercial EPBs, their development over the years and the state of the art. Sections 1.2 and 1.3 are background introduction on environmental disturbance rejection and non-uniform human input compensation, respectively. More detailed discussion on these two topics, including algorithms, designs, simulations and experiments, will be provided in Chapters 4 and 5. Chapter 2 introduces the hardware setup used for the experiments. Chapter 3 discusses about the EPB system dynamics used for the intelligent power-assist algorithms designs. Chapter 6 provides conclusions of the dissertation.

1.1 Introduction of commercial EPBs

The first prototype of electric power-assisted bicycles (EPBs) was developed by the Yamaha Corporation in 1989 [5]. The product was released in July of 1993 and publically sold in April 1994. This was the first commercialized electric bicycle in the world. The Yamaha Corporation called this kind of electric bicycles PAS (Power Assist System). The next year, several other companies also released their own electric bicycle products, including those from Honda, Sanyo, Panasonic, Bridgestone, etc. Over the years, the original lead-acid batteries used on electric bicycles have been replaced by nickel-cadmium (NiCd or NiCad) cells, and later by nickel-metal hydride (NiMH) cells. Safety, reliability, comfort, simplicity, and light weight have always been the main driving factors in the development of electric bicycle industry.

According to the entry "hybrid vehicle" in Wikipedia [6], there are two types of hybrid bicycles. One is called series hybrid bicycles, where the power transfer from the cyclist to the battery and that from the battery to the motor happen in series. The cyclist's

pedaling power is converted into battery energy through a generator and the battery then powers the motor to drive the whole bicycle system. Such a design constitutes a chainless bicycle. However, this is not the desirable type of design for EPBs. Nearly all the EPBs use a parallel hybrid bicycle type of design, where the human and the motor propel the bicycle through different channels parallely. The torques from the two sources are combined through either a mechanical drivetrain torque mixing mechanism, or a front wheel hub motor, in which case the torque mixing mechanism is not necessary. There are quite a few models of EPBs available in the market. Typically, the motor can be placed in three places on an electric bicycle: on the frame, in the rear wheel hub, and in the front wheel hub. Figure 1.1 shows an electric bicycle (Optibike 850XLi [7]) which has its motor and battery encapsulated inside the frame enclosure. Some kind of gear and one-way clutch system is used to deliver

Figure 1.1: Optibike 850XLi

the motor torque onto the chain-sprocket system, while avoiding the possibility of the motor driving the pedals. The benefit of using a design like this is that the motor's torque input can also take advantage of the bicycle gearing system, which consequently increases the battery and motor efficiency. Electric bicycles that have the motor in the front wheel hub avoid the necessity of using torque mixing apparatus. However, the torque coming from the motor can not take advantage of any bicycle gearing, which can be quite useful for hill climbing. Figure 1.2 shows one of these commercially available models that use front wheel hub motors. Electric bicycles can also have the motor on the rear wheel hub, as shown in Fig. 1.3 [8]. Mechanical

Figure 1.2: Giant Suede-E electric bicycle

torque mixing mechanism is also required in this configuration. At the same time, the motor torque can not take advantage of the bicycle gearing either. There are also many electric bicycle do-it-yourself conversion kits available on the market, where consumers can convert their own traditional bicycle into a fully equipped electric bicycle.

Figure 1.3: Golden Motor electric bicycle model MT-2009

1.2 Environmental disturbance rejection

Most of the EPBs that are commercially available use the proportional power-assist scheme. Usually, the ratio of human power and motor assistive power is set to 1:1, which means that the power provided by the motor would be the same as the amount of the human power. One problem with the current power-assist scheme is its lack of flexibility with respect to the environmental condition. For example, when the cyclist is going up a steep hill, the 1:1 power-assistance may not suffice in terms of providing a smooth ride for the cyclist. Low speeds will invite difficulties in bicycle maneuvering [9]. Also, changes in cyclists from ride to ride will cause, sometimes, huge changes in body weight and thus require quite different amount of assistive power from the motor to compensate for the gravitational drag force. Another intuition is that the adequate assistive power is related to the slope of the hill, which will be changing in the process of riding a bicycle. Based on all these observations, the improved intelligent power-assist systems should be able to deal with the changing environmental drag force (which contains gravitational drag force and road friction force) during uphill riding.

With the environmental drag force being considered as a disturbance to the bicycle system, a disturbance observer (DOB) based power-assist scheme can be utilized to estimate and compensate for the environmental disturbance. DOB is a technique that utilizes the control input and plant output to estimate the disturbance input to the system. It has been successfully applied to various motion control problems [10] [11]. Most of these applications focused on the performance improvement in terms of trajectory tracking precision. Yabushita et al [12] applied a DOB-structured power-assist controller to a tricycle under both uphill running and downhill running conditions, which means that the motor provides not only uphill-running assistive power, but also downhill-running resistive power to the tricycle. However, they did not consider the robust stability issues related to DOB. Komada et al [13] investigated the stability issues and found that by adding the performance improving DOB, stability margins were decreased. This is a typical performance-robustness trade-off existing in nearly every control system. One solution to this problem is the robust DOB design. Ryoo et al [14] proposed a robust DOB design for optical disk drive system. For the EPB system, robustness of the whole system under parameter uncertainties is the most important concern. Disastrous results can happen with a poorly designed power-assist scheme that has little robustness. In Chapter 4, we present a robust DOB design to address the environmental disturbance rejection issue with guaranteed robustness.

Like many other control application problems, actuator saturation exists in the EPB systems. A serious consequence of actuator saturation is the windup of the integral controller. In practice, there are different and usually ad-hoc ways to deal with actuator saturation and integrator windup. These methods are commonly referred to as anti-windup schemes. Guo et al [15] placed a fictitious saturation block inside the controller structure to deal with secondary-stage actuator saturation in dual-stage control of a hard disk drive. In Chapter 4, we take a similar approach and address the motor input saturation with two add-on saturation elements in the robust DOB design as an anti-windup scheme. Experimental results will be shown to verify the effectiveness of the proposed scheme.

1.3 Non-uniform human input compensation

Another issue with uphill riding is the discomfort caused by the non-smooth velocity and acceleration profiles. Due to the design of the crankset on a bicycle, the torque input from human is not constant over a pedal cycle; the pedal torque reaches a local maximum twice over one pedal cycle. The non-smoothness in velocity and acceleration caused by the non-uniform human input becomes more noticeable during uphill riding, and thus, causes discomfort. We note that the non-uniform pattern is almost repetitive from one cycle to another. Thus, we propose two repetitive control based power-assist schemes to compensate for the non-uniform torque generation by the rider.

Repetitive control is often used for periodic disturbance rejection and/or periodic reference signal tracking. It has been successfully applied in many motion control problems involving rotary motions, such as hard disk drives [16] and Compact Disc players [17]. It has also been applied to noncircular machining [18]. A more general review about the methods to deal with periodic disturbances and recent applications of repetitive control can be found in Tomizuka [1]. Repetitive controllers are designed based on the internal model principle (IMP). Through incorporating the internal model of the disturbance signal in the controller denominator, repetitive controllers pose an infinitely high gain at the disturbance frequency in the open loop frequency response, and, thus, reject the repetitive disturbance with the closed loop.

In Chapter 5 of this dissertation, we consider two ways of modeling the sinusoidal-

like signal in the human input, i.e., one as a sinusoidal signal, and the other as a nonsinusoidal periodic signal. These two modeling methods give different internal models for the oscillatory component of the human's torque input. To be specific, when modeled as a sinusoidal signal, the oscillation source has an internal model of $1 - 2cos\omega_h q^{-1} + q^{-2}$, where q^{-1} is a backward shift operation and ω_h is the frequency of the sinusoid. The internal model for a non-sinusoidal periodic signal is $1 - q^{-N}$, where N is the period of the periodic signal.

Since the human input's frequency is changing from time to time while the bicycle is in motion, the above-mentioned models are both time-varying. We deal with the two time-varying internal models in two respective ways. For the sinusoidal model, the changing frequency is considered as a changing parameter, and an adaptive handling manner is adopted. For the nonsinusoidal periodic model, each pedal revolution is sliced into N_s sectors so that the period of the signal in the discrete time domain is N_s and fixed. This way, the sampling period for the repetitive control depends on the pedaling speed and the bicycle dynamics become time-varying. Repetitive controllers based on the two different internal models will be considered in Chapter 5 and their performance will be compared with simulation results. Experimental results for the nonsinusoidal periodic model based design will be shown for validation purposes.

Chapter 2

Hardware Setup

2.1 Experimental EPB system

A Giant Suede-E electric bicycle was acquired for the research. Figure 2.1 shows the locations of the major parts used to control and motorize the EPB. It has a

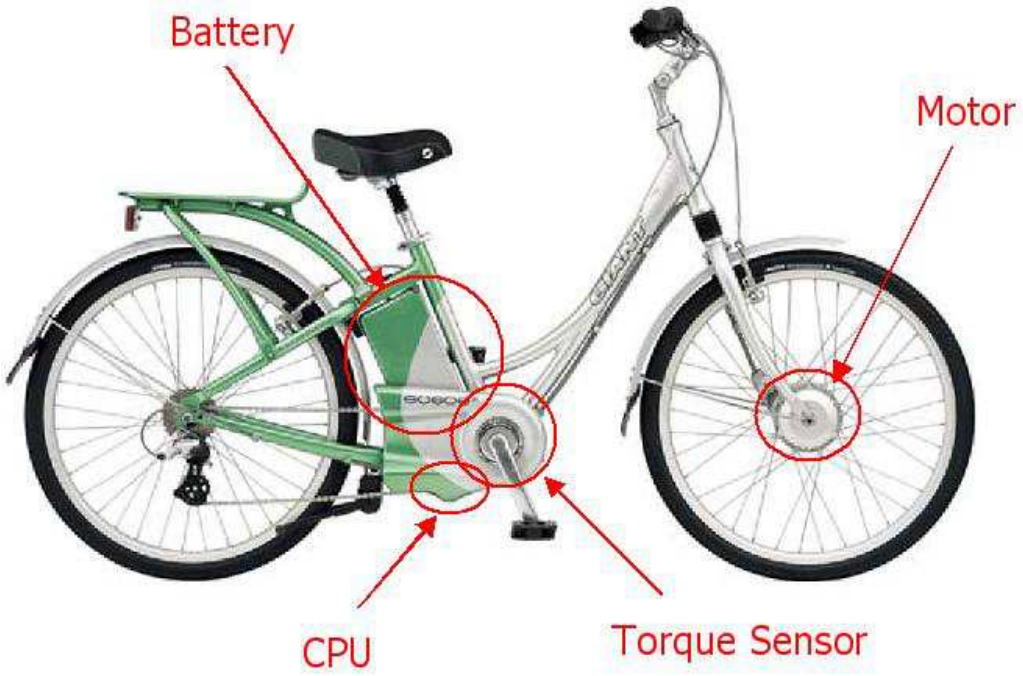

Figure 2.1: EPB anatomy

36-volt nickel-metal hydride (NiMH) battery attached to the bicycle frame and a 9A/36V electric hub motor in the front wheel. The central processing unit (CPU) located underneath the crankset controls the motor torque based on the sensing signal from the torque sensor inside the sprocket case. The CPU on the Giant EPB is an integrated circuit chip which contains the circuitries for the motor driver, the torque sensor signal collection and the actual controller which controls the amount of assistive torque provided through the motor. The controller employs traditional proportional assistance algorithm, as introduced in Chapter 1. For experimental tests of the intelligent power-assist algorithms, we disengage the original CPU and use a laptop computer as the new CPU, which calculates real-time power-assist control input signal based on all measurements. Data acquisition and communication between the laptop computer and the bicycle are done using a National Instruments (NI) USB-6211 data acquisition (DAQ) board (shown in Fig. 2.2). The board contains 16 analog

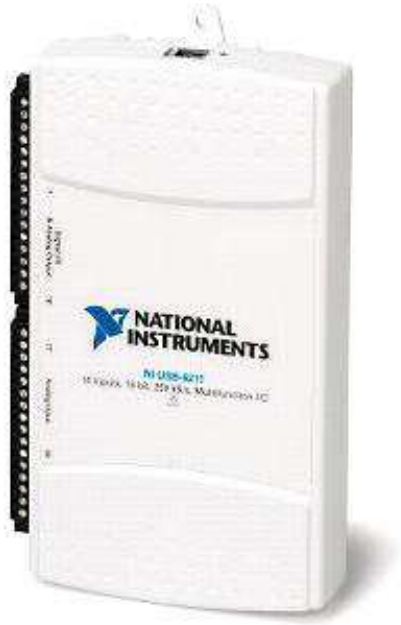

Figure 2.2: NI USB-6211 DAQ board

inputs (16-bit, 250kS/s), 2 analog outputs (16-bit, 250kS/s), 4 digital inputs, 4 digital outputs and 32-bit counters. The versatility of input and output channels makes it suitable for the application. Two bicycle trainers were used to hold the bicycle and provide resistance to each of the two wheels. They make it possible to acquire sensor measurements in the laboratory. The experimental system is shown in Fig. 2.3. The

Figure 2.3: Experimental EPB system

laptop computer is placed inside the metal mesh basket on the bicycle's back seat. Cord strings are used to fasten the laptop in real road experiments.

2.2 Front wheel electric hub motor

The motor used on the Giant EPB is an electric hub motor, which is located in the front wheel hub (Figure 2.4). It is a brushless DC motor with 36V voltage rating and

Figure 2.4: Electric hub motor in the front wheel

9A current rating. A brushless motor does not have issues with mechanical wear of the brushes as the brushed motors do, but it requires electrical commutation schemes to drive the motor. We call circuits performing such tasks motor drives. The original motor drive was integrated in the EPB's CPU chip. Since we have to disengage the CPU and apply new control algorithms through a laptop computer, a new motor drive circuit needs to be built to replace the original one [19]. Multiple testings and measurements were done to understand the working scheme of the original motor drive. Figure 2.5 shows the commutation scheme of the original motor drive. The first two graphs showed the motor voltage and current associated with each of the three phases. The third graph showed how the three parallel signals from the motor's internal Hall sensors changed for the three phases. A new motor drive was built on a

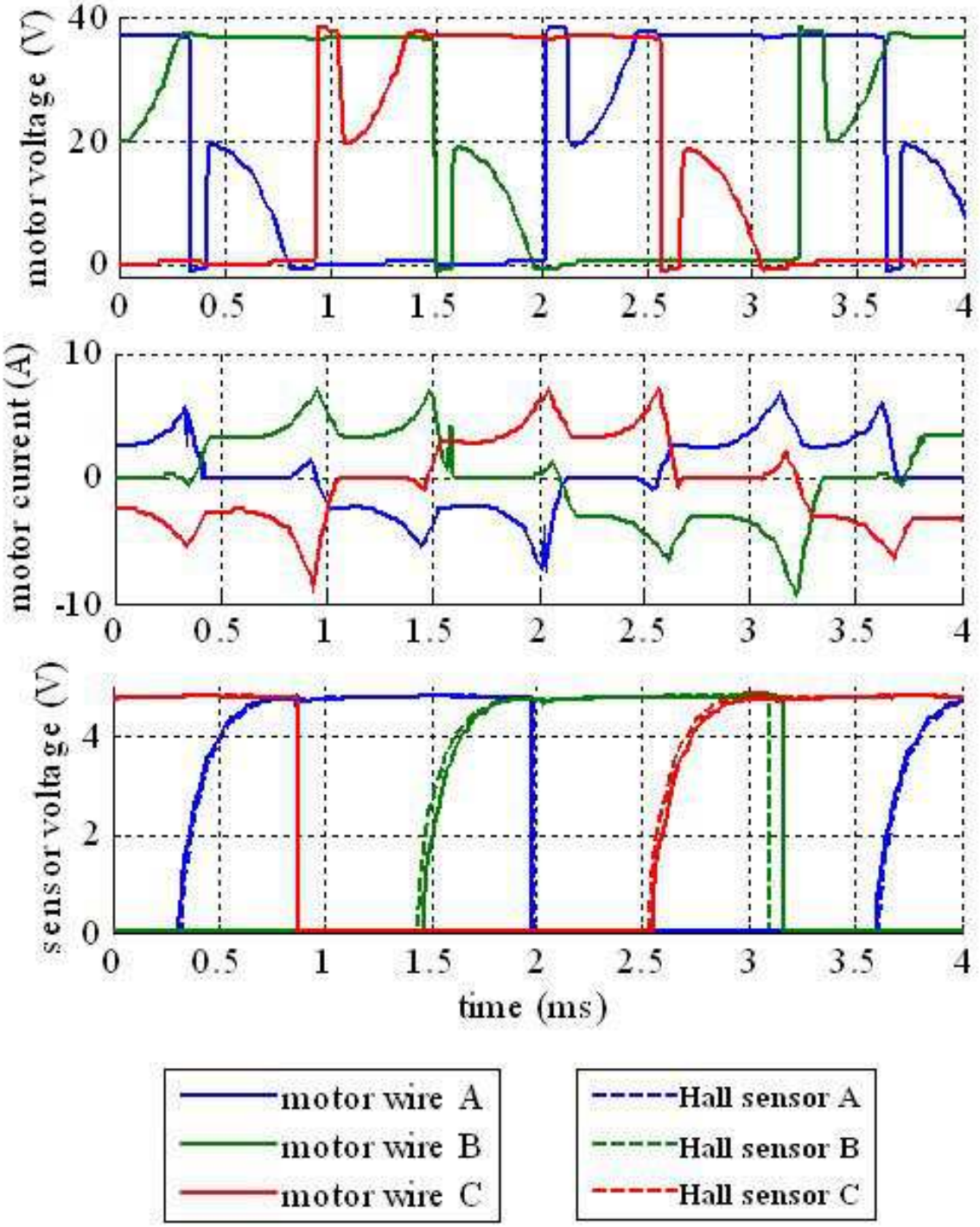

Figure 2.5: Commutation scheme of the original motor drive

stripboard, as shown in Fig. 2.6, to imitate the behavior of the original motor drive utilizing motor current control. With the rebuilt motor drive, we can control the torque output with a voltage input control.

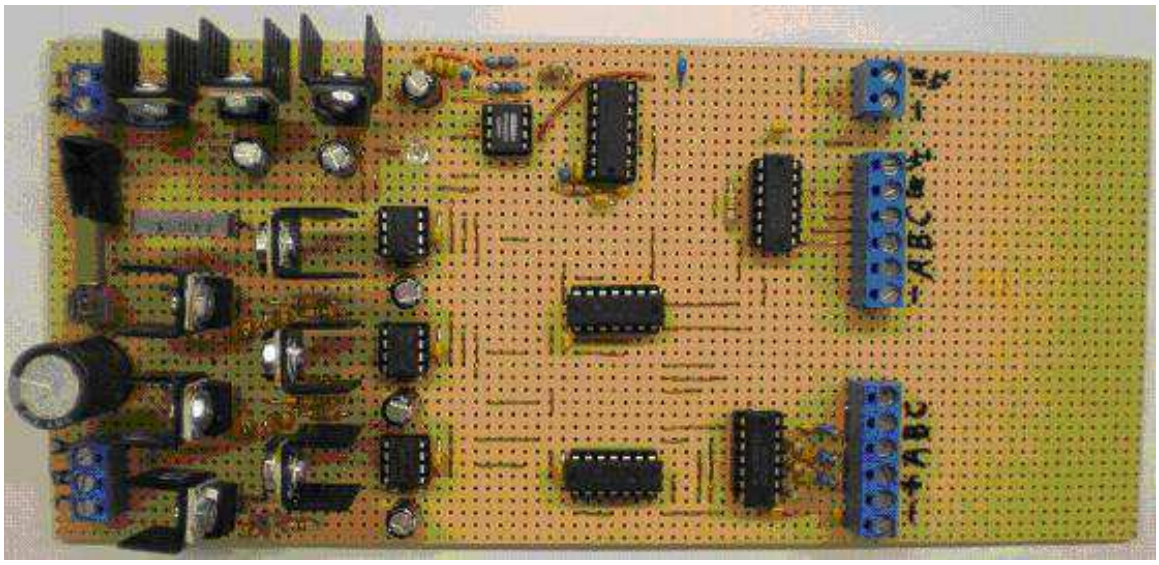

Figure 2.6: Rebuilt motor drive

2.3 Giant Magnetostrictive Materials (GMM) torque sensor

2.3.1 Magnetostriction, Villari Effect and the Principle of GMM Force Sensor

Magnetostriction (refer to Wikipedia [20]) is a property of ferromagnetic materials that causes them to change their shape or dimension when subjected to a magnetic field. The effect was first identified in 1842 by James Joule when observing a sample of nickel. Reversely, if an external force deforms a piece of magnetostrictive material, the magnetic field surrounding the piece will change. This effect is the inverse of magnetostriction called the Villari effect.

Magnetostriction can be found in many ferromagnetic materials. From a physical or scientific point of view, most of these materials are not useful because of the

fairly small changes in dimension or shape. However, a small number of magnetostrictive materials have large changes. These are called "giant magnetostrictive materials"(GMM).

One of the applications of magnetostriction is the GMM force sensor. The principle of a GMM force sensor is depicted in Fig. 2.7. A cylindrical GMM element is placed in

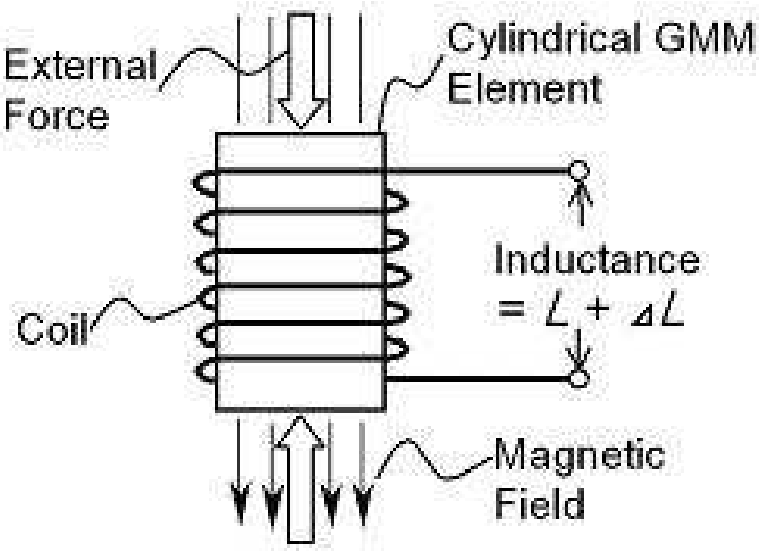

Figure 2.7: GMM force sensor working scheme

a coil as its core. An external force acts on the GMM element. The inductance of the coil will change due to Villari effect when the external force exists. The inductance of the coil and the magnitude of the external force have a fixed relation. Therefore, if the inductance is measured in real time, the external force can be estimated using the known relationship between the two.

2.3.2 GMM torque sensor for EPBs

The torque sensor is a critical component of an EPB, and it detects the human's intention and/or condition. Since the Giant Suede-E EPB that we purchases already has a torque sensor on board, it makes practical and economical sense to utilize the original torque sensor. Efforts were made to understand the type of the torque sensor as well as its underlying working scheme.

Through various experimental testings and observations, as well as literature survey, we identified that the torque sensor installed on the Giant EPB is a GMM force sensor. It is placed inside the sprocket case. The sprocket case contains an inner sprocket connected to the crank and an outer sprocket connected to the gear teeth. The GMM force sensor and three springs are used to transfer forces from the crank and the inner sprocket to the outer sprocket, which drives the chain. The GMM unit senses forces and transduces it into an electric signal, which is measured and analyzed by the laptop through data acquisition devices. Figure 2.8 shows a schematic drawing of the sprocket case that contains the GMM sensor. Since the distance from the GMM force sensor to the axle is known, the torque can be calculated easily based on the force measurement. Thus, the GMM force sensor works as the torque sensor in the EPB.

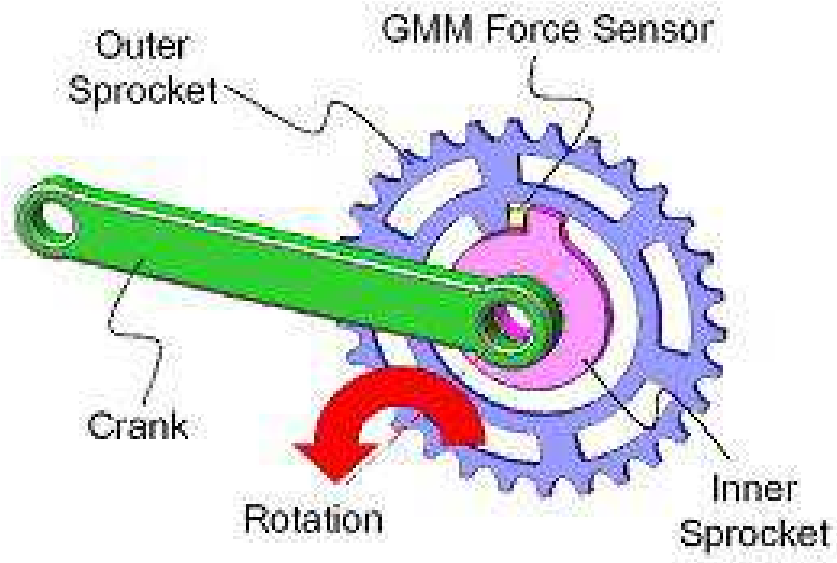

Figure 2.8: Schematic drawing of the sprocket and the GMM sensor

2.3.3 GMM sensor measurement scheme

A constantly excited voltage is supplied to the sensor and a resistor is put in series with the coil. By measuring the changes in the voltage across the resistor, the changes in the inductance can be known. The measuring circuit is shown in Fig. 2.9.

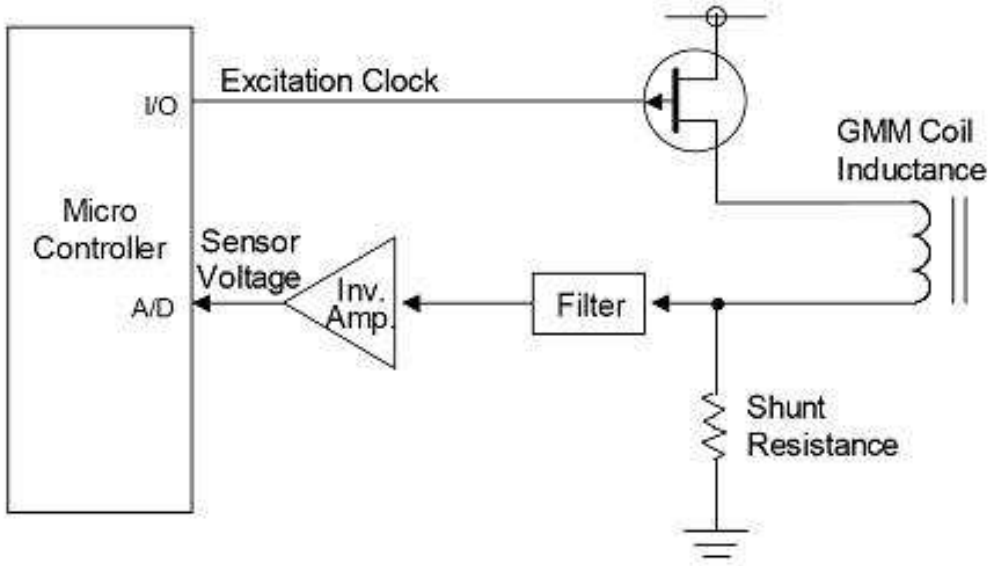

Figure 2.9: GMM force sensor measurement scheme

2.3.4 GMM sensor calibration

The GMM torque sensor was calibrated by using a torque wrench to apply a known torque on the bottom bracket axle. Corresponding voltage measurements were then taken from the GMM torque sensor. The magnitude of the measurement signal will increase if the sensor is under external compression force. For each set of measurement, we hold the torque wrench at a constant torque level (e.g. 50N·m±2%) for 3 seconds and record the maximum torque applied during this period. Correspondingly, the maximum value of each sensor measurement signal is used to indicate the sensing signal level. The experimental calibration results are shown in Fig. 2.10. The GMM sensor is linear within the measured range. Saturation tendency is shown above 85 N·m. Least squares line fitting technique was used to build a linear model for the GMM sensor measurements. The resulting model can be expressed as shown in Eq. (2.1), where V_{GMM} is the output voltage of the GMM sensor, T_{in} is the input torque from human measured in N·m.

$$V_{GMM} = 1.78 + 0.002724 \times T_{in} \tag{2.1}$$

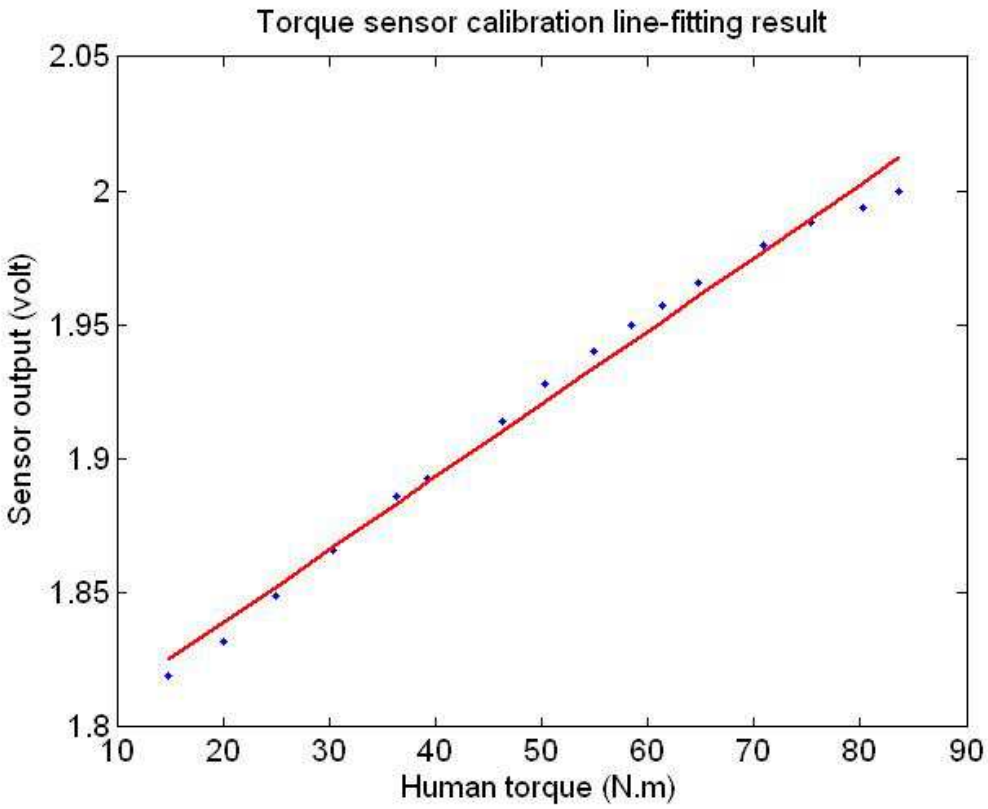

Figure 2.10: GMM force sensor working scheme

2.4 Bicycle velocity sensor

Bicycle velocity is an important feedback signal in the power-assist control loop. In the Giant EPB, the bicycle velocity signal is obtained from the hub motor's internal encoder. The encoder signal generates 243 pulses per front wheel rotation cycle. Pure differentiation of the encoder signal is used as the instantaneous bicycle velocity measurement. In the repetitive controller experiment, measurement noise caused by quantization error and differentiation technique was so prominent that it deteriorated the overall performance of the controller. A fourth order Butterworth filter was used in this case to suppress measurement noise and smooth out the bicycle velocity measurement. The effect of the filter on the velocity measurement will be discussed in Section 2.5.

2.5 Hardware limitations

Physical systems usually have hardware limitations and we should exercise caution on these limitations in both controller design and implementation. The block diagram in Fig. 2.11 shows the configuration of our bicycle experimental system. Crucial limitations in our case can be classified into three categories: 1) sensor limitations, 2) DAQ system I/O interface limitations and 3) motor limitations.

The system has three sensors, an encoder for pedal angle measurement, another encoder for motor rotational angle measurement, and a torque sensor for human generated torque measurement. Encoders have quantization errors by the nature of their design. Velocity measurements obtained through differentiation of an encoder signal become even more noisy. The encoder for motor angle measurement generates 243 pulses per revolution. To acquire the velocity measurement in our EB system, we utilize a 4th-order butterworth filter to suppress the quantization error. Figure 2.12 shows the effect of the filter on the noisy velocity measurements. We can see that the butterworth filter can successfully smoothen the signal while maintaining good fidelity to the underlying velocity information.

As indicated in Fig. 2.10, the torque sensor tends to saturate when the input torque is above 85 N·m. Figure 2.13 shows a profile of torque sensor measurement for human generated torque when riding uphill without motor assistance. We can see that the

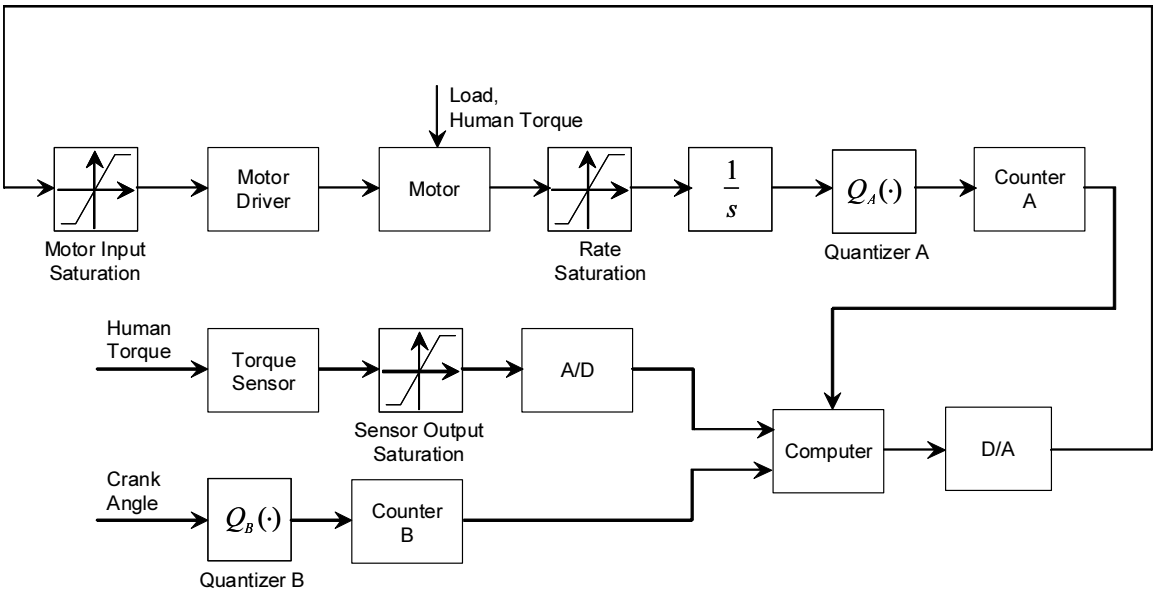

Figure 2.11: Experimental system configuration and limitations

torque sensor saturates above about 90 N·m. In this dissertation, we suppose the human torque measurement is not saturated when motor assistance is applied. Future research is needed to verify this assumption.

The National Instruments data acquisition (DAQ) board (Figure 2.2) have two counters that run fast enough to count pulses from encoders. They don't pose any limitations to our application. The analog I/O ports take input voltages that are within [-10V, 10V]. In our experimental setup, electrical connections have been designed to avoid these constraints. Thus, the DAQ board is not a limiting factor.

The front wheel hub motor for generating assistive torque has two crucial limitations, i.e., input saturation and rate saturation. The input to the motor is limited from 0 to 5 $volts$. This implies that the motor can only provide assistive torque to the bicycle and the maximum input voltage limits the motor's assistive capability. Figure 2.14 shows that the motor has rate saturation and the angular velocity only goes up to about 23 rad/s. Of course there are sophisticated controllers taking those limitations into account from the nonlinear or switching control viewpoints, but our scope in this research is focused mainly on designing novel intelligent power-assist control algorithms. We will only check whether or not the resultant controller violates these limitations and causes performance deterioration.

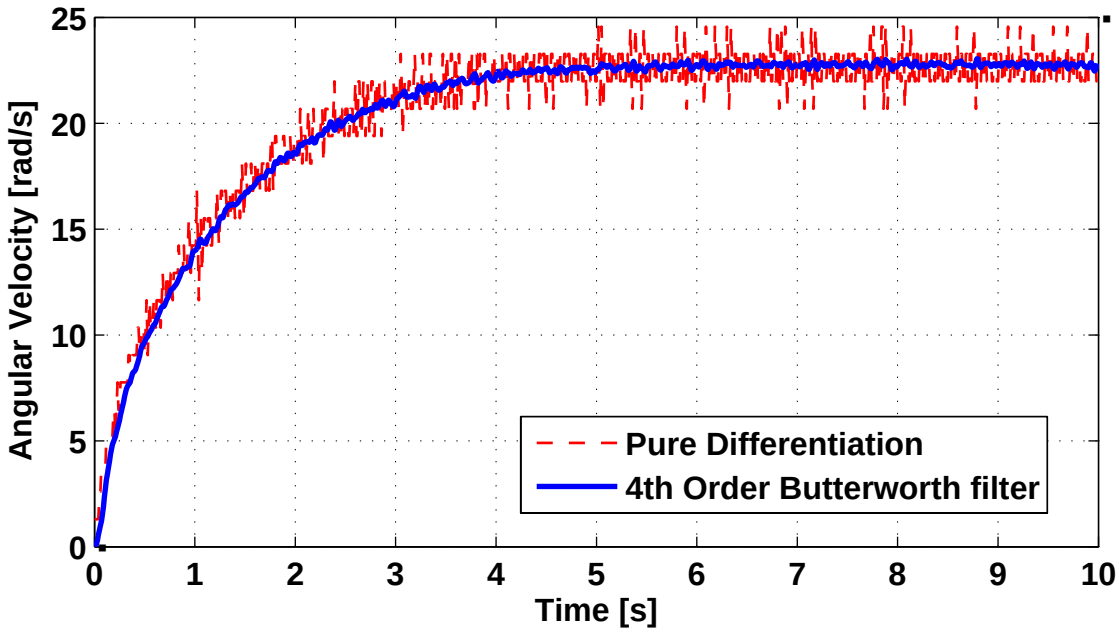

Figure 2.12: 4-th order Butterworth filter for measurement noise rejection

2.6 Intelligent Power Assist Bicycle System

The ultimate goal of our research is to design intelligent power-assist algorithms to help the cyclist ride uphill more easily. The structure of an intelligent power assist bicycle system is shown in Fig. 2.15. The intelligent power-assist unit takes in the information from the bicycle velocity sensor and the GMM human input torque sensor, as well as other sensor information, and makes a decision on the amount of assistive torque to supply through the motor. Our task is to design the suitable power-assist algorithm and realize it on the experimental EPB setup.

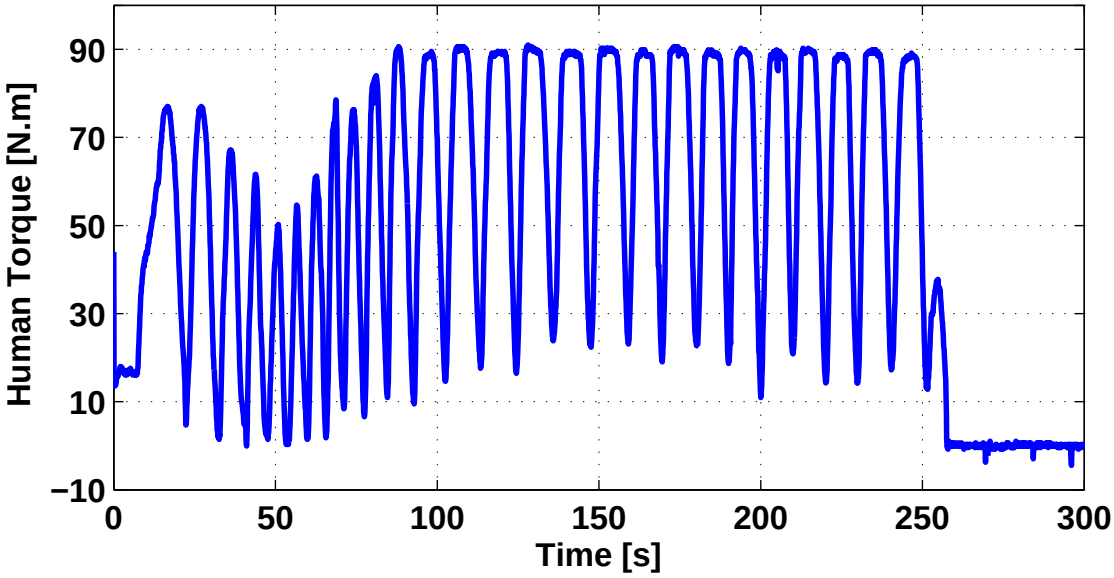

Figure 2.13: An uphill-riding human torque profile

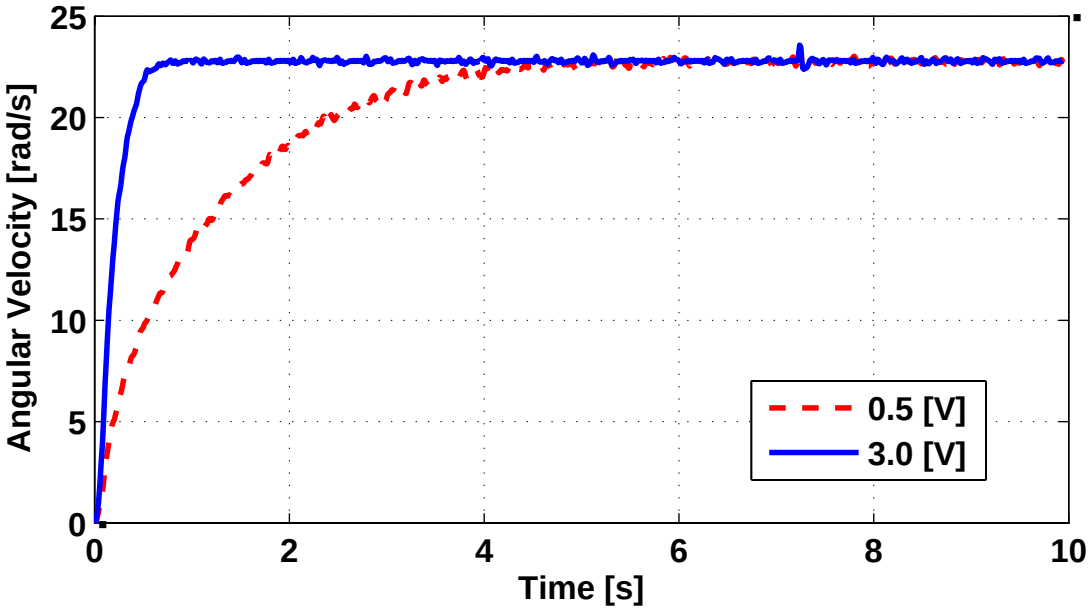

Figure 2.14: Rate saturation for inputs 0.5[V] and 3.0[V]

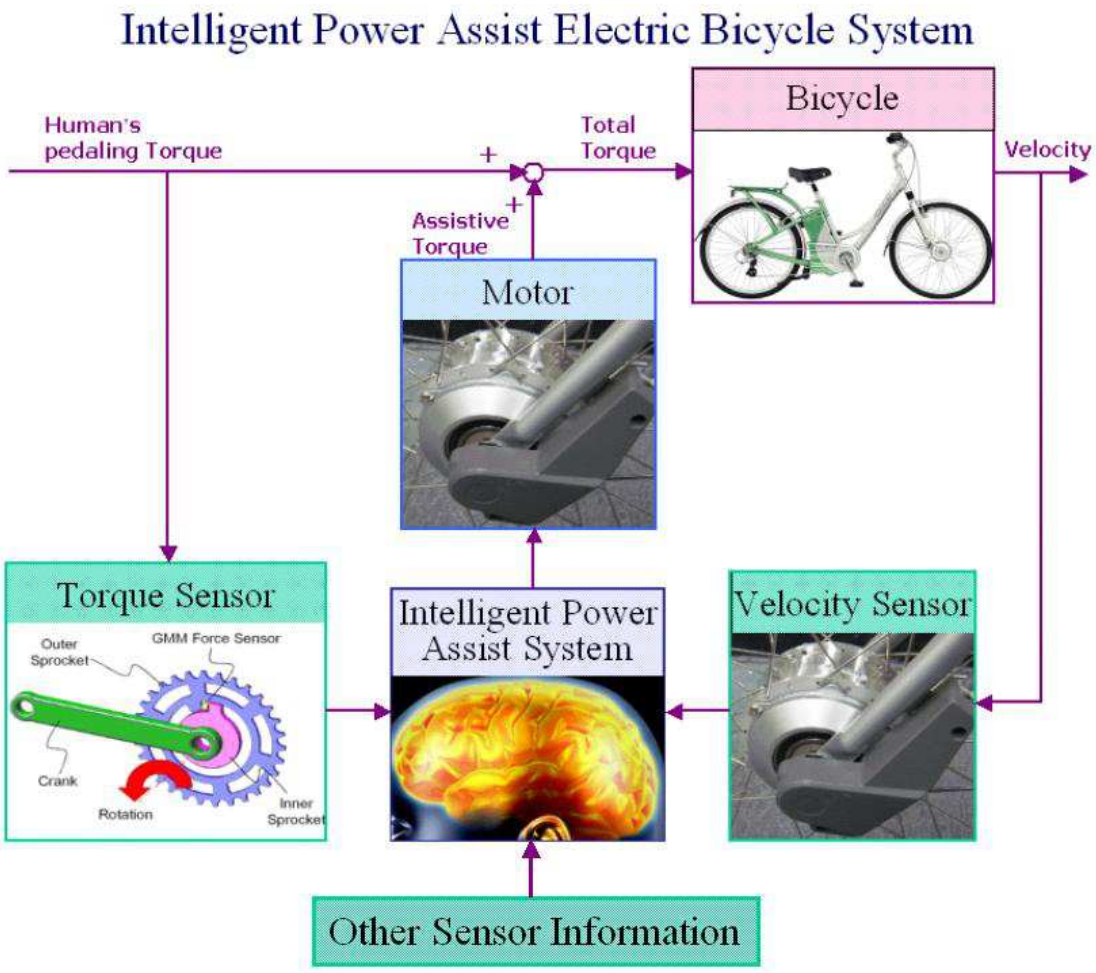

Figure 2.15: Schematic diagram of intelligent power assist bicycle system

Chapter 3

System Dynamics and Parameters

We need to study the dynamics of an EPB to understand its key properties and operating conditions. We also need a model that captures all the relevant dynamic properties of an EPB for intelligent power-assist algorithm design and simulation purposes. Electric power-assist bicycles (EPBs) are essentially just traditional bicycles with an additional power supply (input) in the longitudinal direction, i.e., the motor. A bicycle has three degrees of freedom, which are the roll angle, the steering angle, and the longitudinal velocity. EPBs and traditional bikes have similar maneuvering and stability characteristics. The only difference might be the change in weight distribution caused by the mounting of the battery and the added motor. However, this difference is trivial and the dynamic properties of the two in the roll angle and steering angle degrees of freedom can be considered as the same. Thus, it makes sense for us to study the dynamic properties of a traditional bicycle in order to understand those of an EPB.

Bicycle dynamics were first studied in the late nineteenth century. There is, however, still no complete analytical model that captures the whole dynamics of bicycles. The design of bicycles contains many fine details that are crucial to the stabilization of the system including pneumatic tires, spokes, and the trail (which refers to the horizontal distance between the ground contact points of the front wheel and of the extension of the fork). Approximate models have widely been used for control applications because they are easier to analyze and give necessary fidelity to the complete dynamics. The Point-Mass Model (PMM) [9] is one of the approximation models that are used to study basic bicycle dynamic properties. However, there are certain key phenomenons

that can not be explained by the Point-Mass-Model because the model is overly simplified. Such phenomenons include, for example, the self-balancing behavior and the interaction between steering and roll dynamics. In this chapter, we will first study the roll dynamics and the steering dynamics of a bicycle. We will present the Basic Bicycle Model (BBM), which is more sophisticated and regards the bicycle as a combination of four rigid bodies. It can explain the above mentioned unique phenomenons and will be used as the basis for the EPB dynamics analysis. The BBM will also be used to analyze some stability properties of the bicycle, which will help us understand the purpose of our research focus on uphill riding condition. Simulation results will be shown to verify the analysis.

Section 3.2 will introduce the system dynamic model of an EPB for the design of intelligent power-assist controllers. We will see that in this case, only the bicycle's longitudinal degree of freedom is relevant and the model is a combination of the bicycle's longitudinal dynamics and the motor dynamics. This EPB system dynamic model will be used for intelligent power-assist controller design and simulation purposes later on.

Section 3.3 discusses about the system identification work that we did to identify the values of some of the parameters in the EPB system dynamics, which can not be measured directly. Other parameter values that are measured directly or indirectly will be also provided.

3.1 Basic Bicycle Model

The dynamics of a bicycle are nonlinear by nature. However, a linearized model is valid for small perturbations from the equilibrium position, which is the upright and straight-ahead running condition. The Basic Bicycle Model (BBM) is such a linearized model. In BBM, the bicycle consists of four rigid bodies, which are the front wheel, the rear wheel, the handlebar assembly and the rear frame. The body of the rider is considered to be attached to the rear frame rigidly. Figure 3.1 (picture from [2]) illustrates the four rigid bodies in BBM. As shown in Fig. 3.1, the wheelbase w is the distance between the contact points of the ground with the two wheels. The trail c refers to the horizontal distance between the ground contact points of the front wheel and of the extension of the fork. The head angle λ is the acute angle

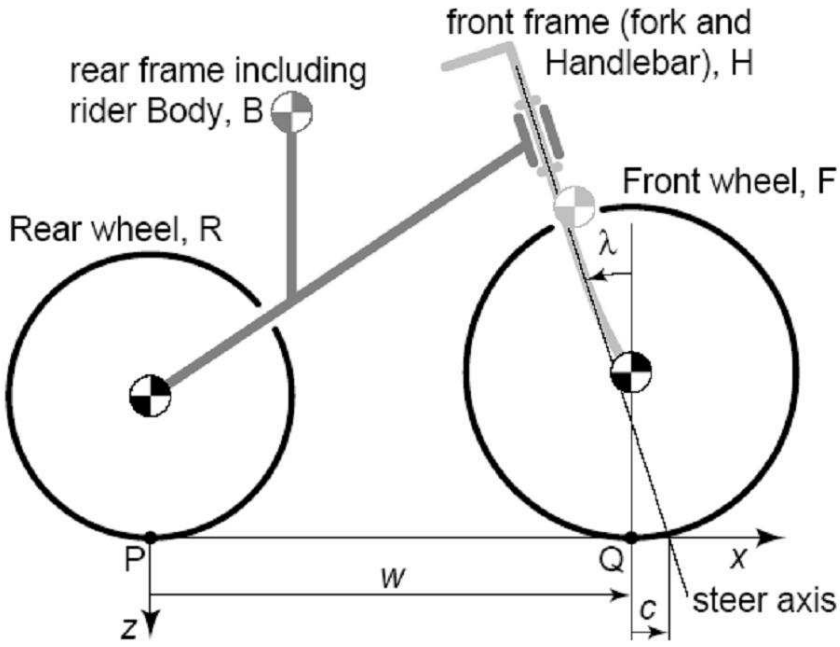

Figure 3.1: The BBM divided into four rigid bodies [2]

that the fork makes with the vertical direction. The bicycle model has three degrees of freedom, which include the steering angle δ, the roll angle φ and the rear wheel rotation angle θ.

As derived and explained in [2] and [3], the linearized governing equations for the roll angle and the steering angle are two coupled second-order differential equations expressed in two degrees of freedom $q = [\varphi, \delta]^T$, as shown in Eq. (3.1).

$$M\ddot{q} + vC\dot{q} + (v^2K_2 + K_0)q = T_{ext}. \tag{3.1}$$

M, C, K_0 and K_2 are two by two constant matrices, whose entries are known functions of the bicycle parameters (refer to [2] and [3] for detailed expressions of these matrices). The right hand side of Eq. (3.1) represents the external torque inputs to the system. $T_{ext} = [T_\varphi, T_\delta]^T$, where T_φ and T_δ are the externally applied torques in the roll dynamics and in the steering dynamics, respectively. The above equations form the BBM introduced in [2] and [3].

The stability of the motion in the upright position with different constant forward velocities was studied in [3]. Figure 3.2 (picture from [3]) shows the changes of the real and imaginary parts of the eigenvalues of the system as a function of the constant

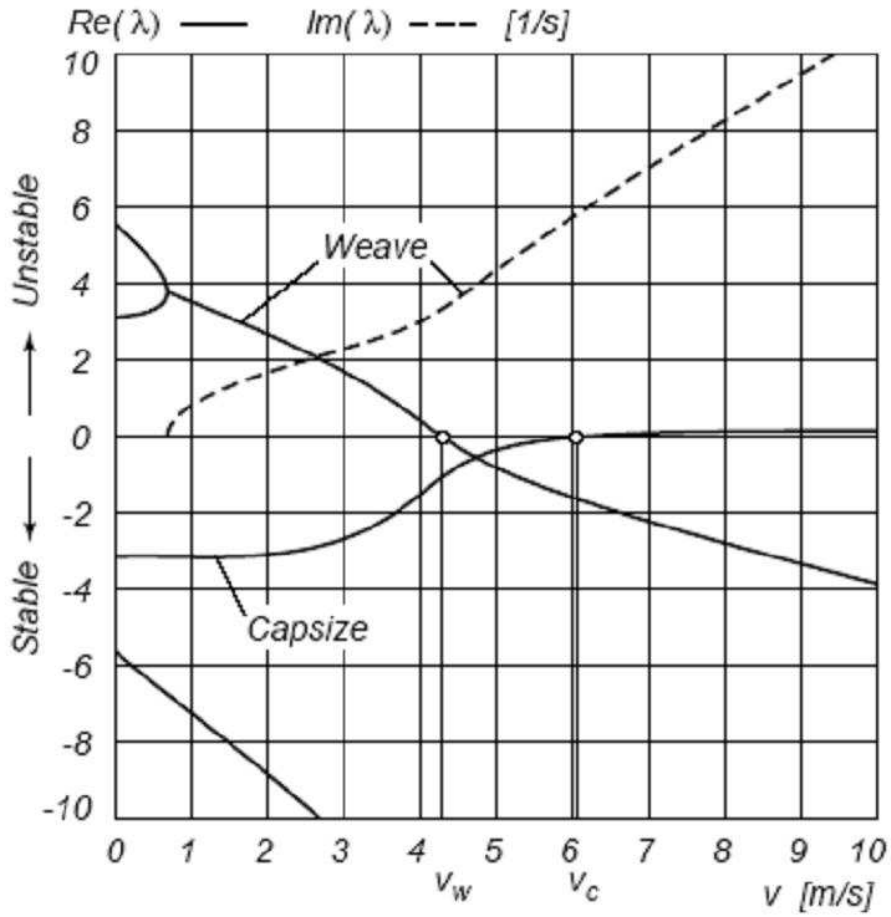

Figure 3.2: Eigenvalues of the system as functions of the constant forward velocity [3]

forward velocity. The system has four eigenvalues. Solid lines in Fig. 3.2 represent real parts of the eigenvalues and the dashed line represents the positive imaginary parts of complex eigenvalue pairs. We can see that within the speed range [4.30 m/s, 6.06m/s], all the eigenvalues of the system have negative real parts, which means that the system is stable around the equilibrium point - the upright position. Self-balancing against small perturbations around the upright position can be expected, which explains the phenomenon shown in [21].

We confirmed the stability characteristics of the BBM shown in Fig. 3.2 through simulations. The pedaling torque input from the rider is simulated by a sinusoidal signal $T_h = (10 \times \sin 2\pi t + 15)N \cdot m$. When the velocity of the bicycle reaches the desired level, the pedaling torque stops and the bike remains at a constant velocity level. By changing different constant forward velocity values, we verified that within the range [4.30m/s, 6.06m/s], the bicycle could balance itself against small perturbations around the upright position. Figure 3.3 shows the response of the system to a small disturbance in the roll dynamics with a forward constant velocity of $v = 5m/s$. We can see that the roll angle converges to zero after a transient period. Thus, the bicycle can balance itself without rider control. Figures 3.4 and 3.5 are the cases with a velocity of 4m/s and 7.5m/s, respectively. In both cases, the forward running velocity falls outside the self-balancing range and the bicycle tips over with small perturbations in the rolling torque. As we can see in Fig. 3.2, as the bicycle speed increases from zero, the two unstable real eigenvalues become a pair of unstable complex conjugate eigenvalues after around $0.6m/s$. Out of the complex conjugate pair, the real and imaginary parts of the complex eigenvalue with a positive imaginary part are shown in Fig. 3.2. This complex pair introduces an oscillatory mode called the weave mode. When this mode has a positive real part, meaning that the weave mode is unstable, a high frequency steering torque will be needed to stabilize the bicycle system, as shown in [9]. Such a maneuvering technique is difficult for the rider and such a phenomenon exists only in the low speed range. To help the rider in uphill riding condition, we should try to bring the bicycle velocity into the self-stabilizing range with the assistive power from the motor. This explains our purpose of focusing our research on the uphill riding situation, which usually involves operating in the low speed range.

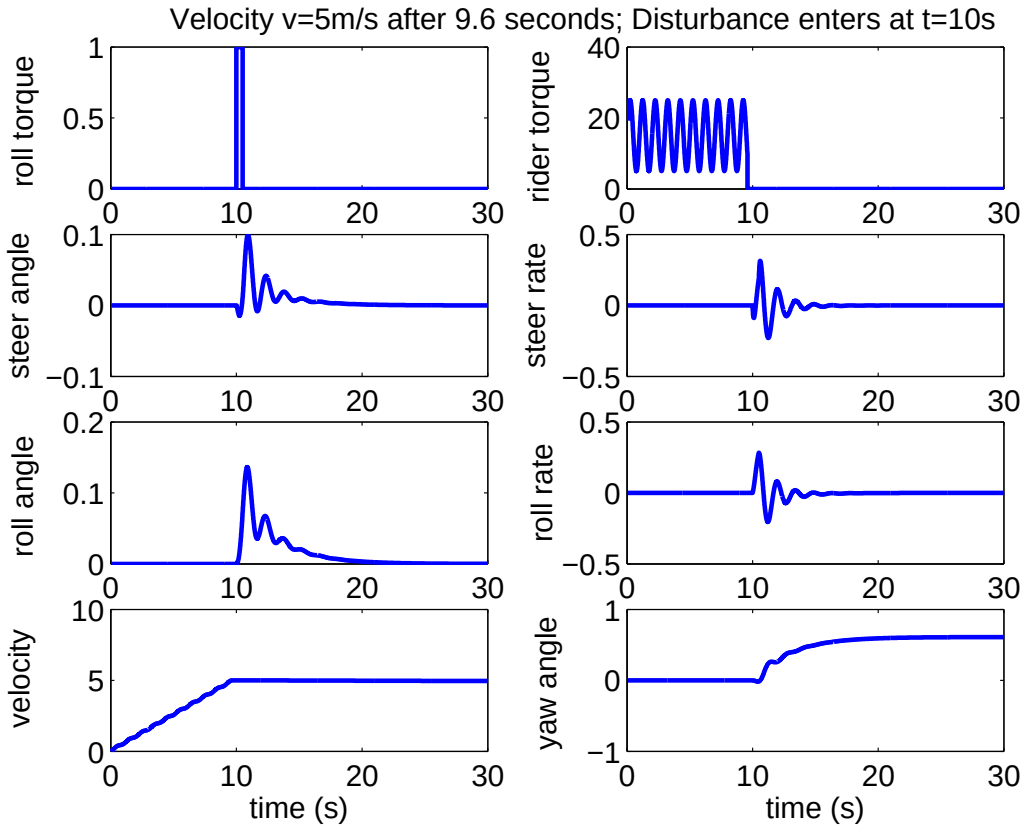

Figure 3.3: The response of the system to a disturbance in the roll dynamics at a constant velocity of 5m/s

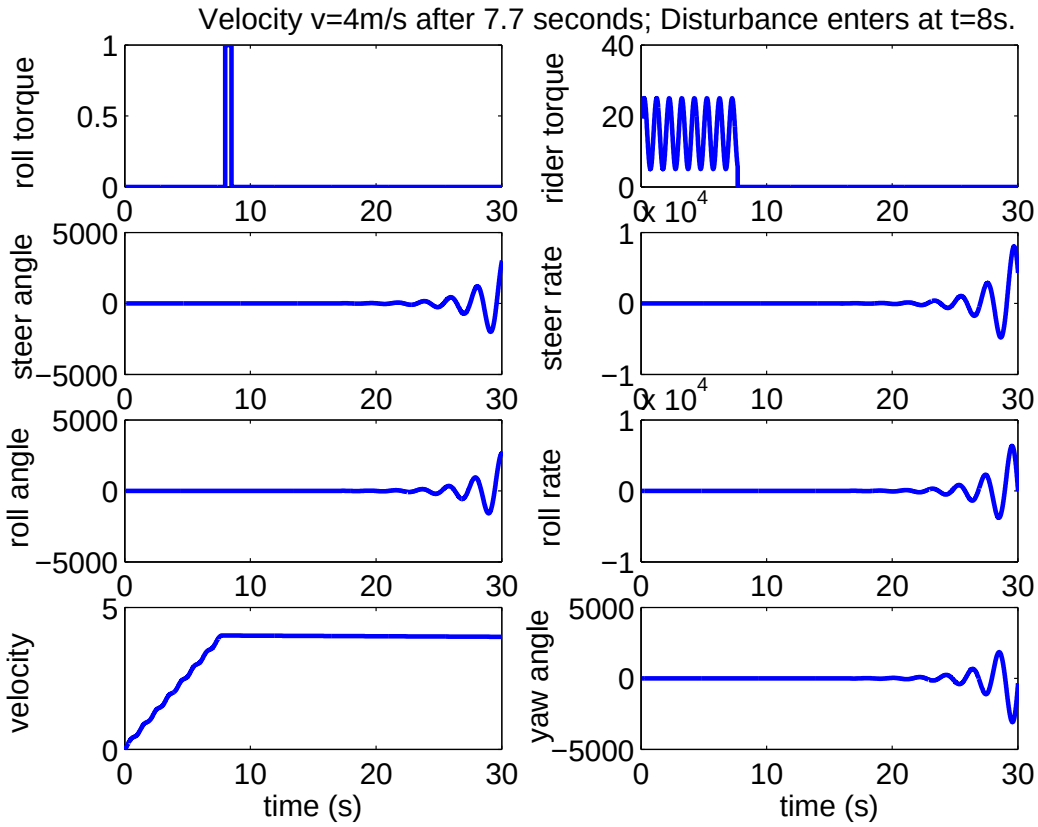

Figure 3.4: The response of the system to a disturbance in the roll dynamics at a constant velocity of 4m/s

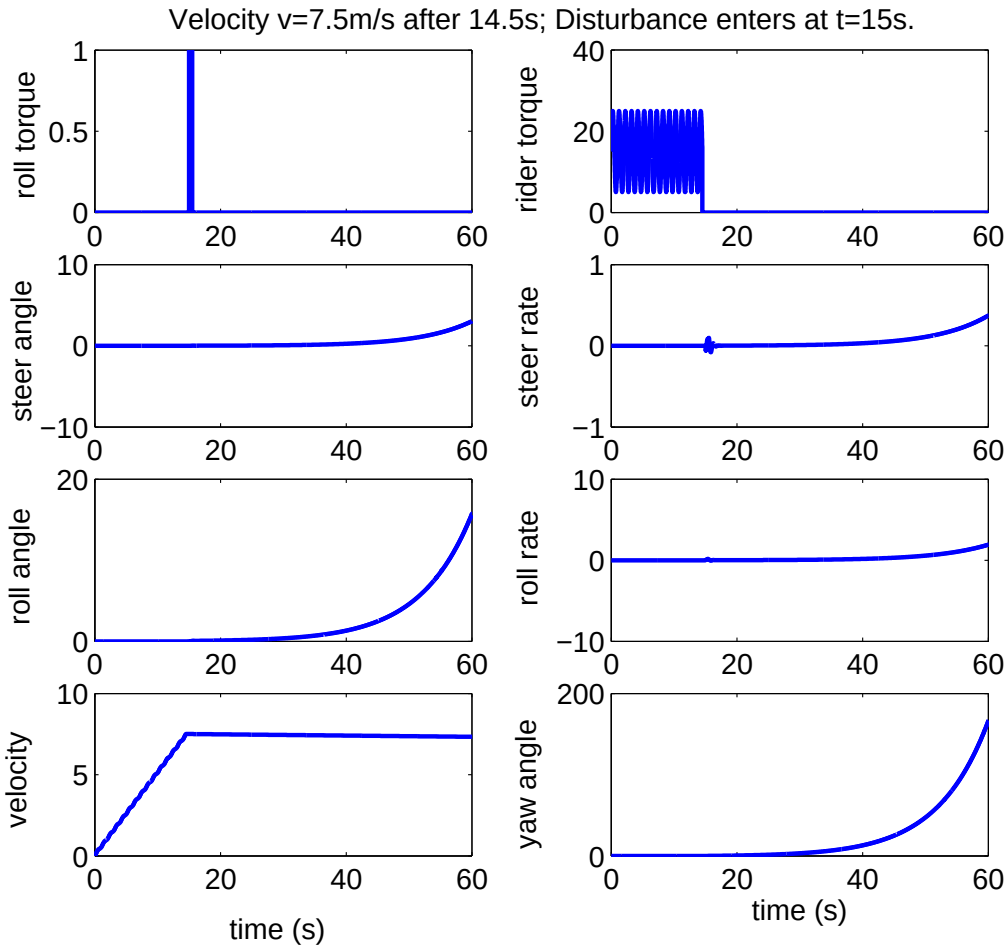

Figure 3.5: The response of the system to a disturbance in the roll dynamics at a constant velocity of 7.5m/s

3.2 EPB system dynamics

The EPB system dynamics are a combination of the bicycle's longitudinal dynamics and the motor dynamics. The two parts are coupled through the bicycle's front wheel velocity. In Subsection 3.2.1, we will introduce the bicycle's longitudinal dynamics. Subsection 3.2.2 is about the front wheel motor dynamics. Subsection 3.2.3 combines the previous two subsections and suggests the EPB system dynamics that we will use for intelligent power-assist controller design.

3.2.1 Bicycle longitudinal dynamics

The bicycle longitudinal dynamics can be derived from Newton's second law of motion

$$\begin{aligned}\left(m_T + I_R/r_R^2 + I_F/r_F^2\right)\frac{dv}{dt} &= -D_{aero} - D_{static-roll} \\ &-D_{dynamic-roll} - m_T g\sin\alpha + F_h + F_m,\end{aligned} \tag{3.2}$$

where $D_{static-roll} = C_{sr}\cdot m_T \cdot g\cdot\cos\alpha$ and $D_{dynamic-roll} = C_{dr}\cdot v$ are the static and dynamic rolling resistances, respectively; $D_{aero} = 1/2\cdot C_w\cdot\rho_{air}\cdot A\cdot(v+v_{wind})^2$ is the aerodynamic drag force caused by the wind. Physical meanings for all the variables and coefficients in (3.2) are summarized in Table 3.1.

We notice that the aerodynamic drag force is nonlinear and is usually negligible in low speed riding and mild head wind condition. We employ the following notations

$$M = m_T + I_R/r_R^2 + I_F/r_F^2; D = C_{dr}, \tag{3.3}$$

and denote the environmental disturbance as

$$d = -D_{static-roll} - m_T g\sin\alpha. \tag{3.4}$$

Equation (3.4) is the environmental disturbance that we will estimate and reject using a robust DOB. Notice that the gravity drag accounts for a major part of the environmental disturbance. With Eqs. (3.3) and (3.4), the bicycle longitudinal dynamics can be expressed as

$$M\frac{dv}{dt} = -D\cdot v + d + F_h + F_m. \tag{3.5}$$

Table 3.1: Variable Meanings in Bicycle Longitudinal Dynamics

Variable	Physical meaning
m_T	Total mass of the bicycle system (including the cyclist)
I_R	Mass moment of inertia of the rear wheel
I_F	Mass moment of inertia of the front wheel
r_R	Radius of the rear wheel
r_F	Radius of the front wheel
v	Velocity of the bicycle
g	Gravitational constant
α	Slope of the road
F_h	Thrust (propelling force) input from human
F_m	Thrust (propelling force) input from motor
C_{sr}	Static rolling resistance coefficient
C_{dr}	Dynamic rolling resistance coefficient
C_w	Aerodynamic drag coefficient
ρ_{air}	Air density
A	Reference area of the bicycle-cyclist system
v_{wind}	Head wind velocity (opposite bicycle velocity direction)

If we express (3.5) in terms of the angular velocity ω of the front wheel (where the hub motor is located), it becomes

$$M \cdot r_F \frac{d\omega}{dt} = -D \cdot r_F \cdot \omega + d + F_h + F_m. \tag{3.6}$$

The motor dynamics and the bicycle longitudinal dynamics will later be correlated through the front wheel angular velocity.

3.2.2 Motor dynamics

The equations governing the dynamics of a motor are as follows

$$U_{amp} = i \cdot R + U_b = i \cdot R + K_b \cdot \omega, \tag{3.7}$$

$$T = K_t \cdot i = J\frac{d\omega}{dt} + B \cdot \omega + T_m. \tag{3.8}$$

Equation (3.7) describes the electrical behavior of a motor[1], where U_{amp} is the amplified drive voltage applied to the motor, i and R are the armature current and

[1]Here we ignored the inductance in the circuit.

the motor resistance, respectively. U_b is the back-emf and K_b is the back-emf constant. Equation (3.8) represents the mechanical behavior of a motor, where T is the mechanical torque on the shaft converted from the armature current. These two quantities are connected through the torque constant K_t. J and B are the inertia and the friction coefficient of the motor. T_m is the torque that is applied to the load. In our system, it is the torque applied through the front-wheel hub motor to propel the bicycle. T_m is related to the propelling force F_m in (3.6) through the relation

$$T_m = F_m \cdot r_F. \tag{3.9}$$

3.2.3 EPB system dynamics – the combined system dynamics

Using (3.6) and (3.9), we get

$$T_m = F_m \cdot r_F = r_F \cdot \left(M \cdot r_F \frac{d\omega}{dt} + D \cdot r_F \cdot \omega - d - F_h \right). \tag{3.10}$$

Equation (3.10) is the load torque in the motor dynamics (3.8). Substitute (3.10) into (3.8), we have

$$T = J\frac{d\omega}{dt} + B \cdot \omega + r_F \cdot \left(M \cdot r_F \frac{d\omega}{dt} + D \cdot r_F \cdot \omega - d - F_h \right). \tag{3.11}$$

On the other hand,

$$T = K_t \cdot i = K_t \cdot (U_{amp} - K_b \cdot \omega) / R. \tag{3.12}$$

Notice that the amplified voltage U_{amp} applied to the motor is related to the voltage U applied to the motor driver through the following equation

$$U_{amp} = K \cdot U, \tag{3.13}$$

where K is the amplification coefficient of the motor driver.

Combining (3.11), (3.12) and (3.13), we have the following dynamic model of the bicycle's front wheel angular velocity:

$$\begin{aligned} \frac{K \cdot K_t}{R \cdot r_F} U + d + F_h = &\left(\frac{J}{r_F} + M \cdot r_F \right) \frac{d\omega}{dt} \\ &+ \left(\frac{B}{r_F} + \frac{K_b \cdot K_t}{R \cdot r_F} + D \cdot r_F \right) \omega. \end{aligned} \tag{3.14}$$

To simplify the expression, we use the following notations

$$J_{eq} = \frac{J}{r_F} + M \cdot r_F, B_{eq} = \frac{B}{r_F} + \frac{K_b \cdot K_t}{R \cdot r_F} + D \cdot r_F, N = \frac{K \cdot K_t}{R \cdot r_F},$$

and (3.14) becomes

$$N \cdot U + d + F_h = J_{eq}\frac{d\omega}{dt} + B_{eq}\omega. \tag{3.15}$$

Equation (3.15) is the combined dynamic model of the whole system including the bicycle and the motor. It is a first order system with three inputs: F_h from the human; $N \cdot U$ from the motor; and d from the environment. Figure 3.6 shows the block diagram of the system.

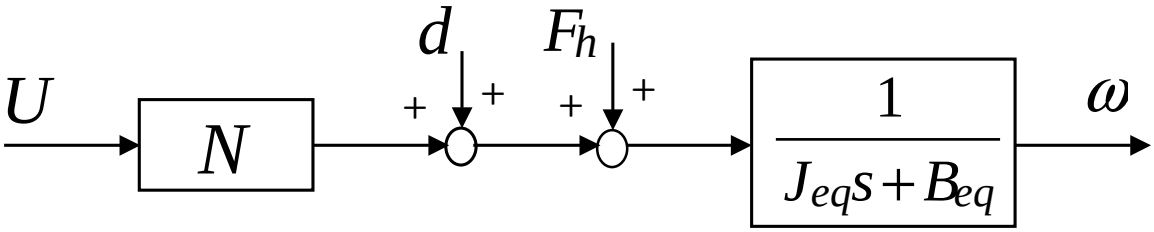

Figure 3.6: Block diagram of combined system (bicycle and motor)

3.3 Motor system identification and bicycle parameters

Values of the parameters in the combined system dynamics model have to be known for further intelligent power-assist controller design and simulation. Parameter values in this dissertation are for the experimental EPB, a Giant Suede E model, that we have acquired for the project. Frequency domain least squares fitting is used for identifying the motor parameters in Eqs. (3.7) and (3.8), while direct measurements of the experimental bicycle provide the bicycle parameters in (3.2).

3.3.1 Motor system identification

If the load $T_m = 0$, the transfer function of the motor can be derived from Eqs. (3.7) and (3.8)

$$G_m = \frac{\Omega(s)}{U(s)} = \frac{K \cdot K_t}{RJs + RB + K_b K_t}, \tag{3.16}$$

where $\Omega(s)$ and $U(s)$ are the Laplace transforms of the angular velocity ω and the motor input voltage U, respectively. Random input $u = 0.3+0.1z$ was used as stimuli, where $z \sim N(0,1)$. The measured frequency response is drawn as the solid line in Fig. 3.7. We fit the measured frequency response with a first order system and get the least-square fitted model as the dotted line in Fig. 3.7. The identified model is

$$G_m = \frac{18.36}{s + 0.5}. \tag{3.17}$$

In (3.16), $K = 10$ is known. $R = 0.4\Omega$ is measured from the motor. $K_t = 0.257962N \cdot m/A$ is calculated through a group of tests on different motor input voltages and the corresponding static output torques. We assume that $K_b = K_t$. Then the two unknown parameters J and B can be calculated using the identified parameters in (3.17). The values of motor model parameters are listed in Table 3.2.

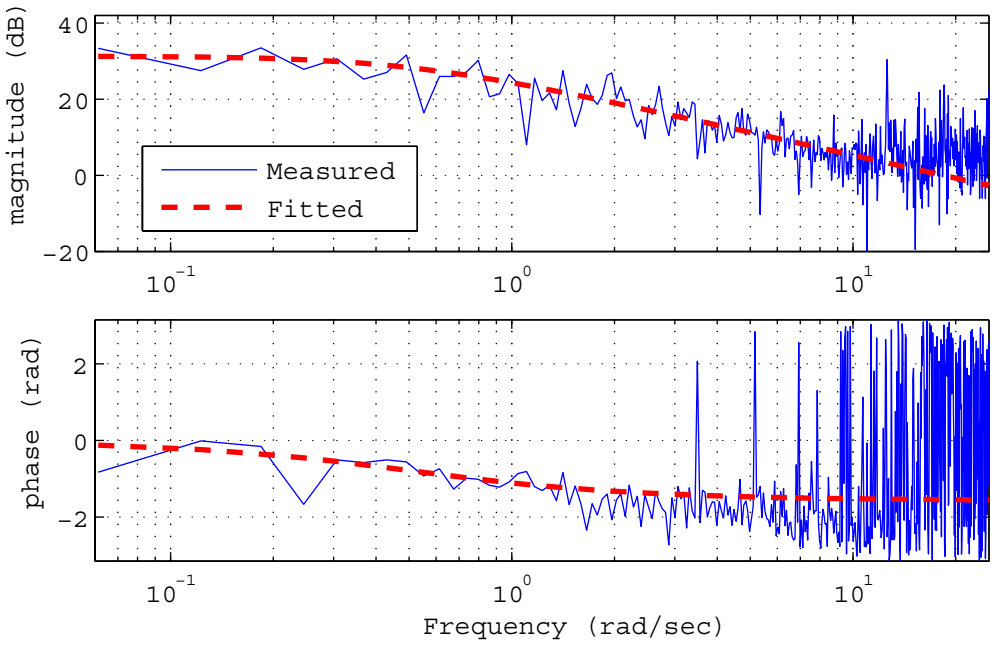

Figure 3.7: Motor dynamics frequency identification

3.3.2 Bicycle parameters

The related bicycle parameters that we will use in analysis are listed in Table 3.3.

Table 3.2: Nominal values for motor parameters

Motor parameter	Value
R	0.4Ω
K	10
K_t	$2.58 \times 10^{-1} N \cdot m/A$
K_b	$2.58 \times 10^{-1} V \cdot s/rad$
J	$3.51 \times 10^{-1} N \cdot m \cdot s^2/rad$
B	$9.27 \times 10^{-3} N \cdot m \cdot s/rad$

Table 3.3: Bicycle parameter values

Bicycle parameter	Value
I_R	$0.12 kgm^2$
I_F	$0.28 kgm^2$
r_R	$0.3m$
r_F	$0.35m$
g	$9.81 N/kg$
C_{sr}	0.0029
C_{dr}	$0.1004 N \cdot s/m$

Chapter 4

Environmental Disturbance Rejection

In the uphill riding situation, the gravity's component force that acts against the bike's forward motion along the slope direction becomes the major drag force for the bicycle. As we have seen in Chapter 3, operating in the low speed range requires high frequency stabilizing steering torque and thus is more difficult for the rider. To help the cyclist ride easier in this situation, we want to remove the effect of the gravity drag on the bicycle system with the assistance from the motor. The gravity drag force along with other friction force can be considered as a disturbance input to the EPB system. The disturbance observer (DOB) technique is an effective method to remove such kind of disturbance input. In this chapter, a robust DOB design will be introduced to reject the disturbance input and make uphill riding feel the same as level ground riding to the cyclist. Robust designs can guarantee system stability and performance in the presence of uncertainties, which naturally exist in an EPB system (or almost every practical system). Hardware saturation is another big concern for every practical system. In the EPB experimental system, the front wheel hub motor poses input voltage saturation which limits the DOB's compensation capability. Modifications to the robust DOB design are needed to address the motor saturation issue. In Section 4.1, we will give a basic introduction to the DOB design technique. Section 4.2 introduces the DOB structure that we use for the environmental disturbance rejection. Section 4.3 describes the robust H-infinity design that we used in choosing the Q-filter for the DOB. Section 4.4 shows the experimental results which confirmed

the effectiveness of the robust DOB design for environmental disturbance rejection. In Section 4.5, an anti-windup robust DOB design will be introduced which can provide robust environmental disturbance rejection within the motor limit. Experimental results of the anti-windup design will also be shown.

4.1 Background introduction on disturbance observer

The disturbance observer (DOB) technique was first introduced in 1987 by Ohnishi [22] [23] and later refined in 1991 by Umeno and Hori [24]. It has become one of the most popular techniques used in high accuracy motion control applications [25] [26], especially for disturbance rejection in motion control systems [27]. It can also be used for robust control problems where uncertainties and model mismatches are considered as an equivalent disturbance input. In motion control applications, the disturbance observer can be applied to both the velocity feedback loop and the position feedback loop, although implementation in the velocity feedback loop is considered to be simpler than that in the position feedback loop. Usually, if major uncertainties and disturbances are removed by DOB in the velocity feedback loop, the position feedback loop can be easily stabilized with satisfactory performance using linear feedback control theory. In practice, DOB is sometimes used as an add-on controller to remove unwanted disturbances within certain frequency range, in addition to the basic stabilizing controller.

In this dissertation, we will consider disturbance observer design for the type of systems where the disturbance input and the system input have the same transfer function to the system output. The mismatch between the actual plant and the plant model can also be deemed as an equivalent disturbance input to the system. Such a system with an input disturbance can be expressed as in Eq. (4.1), where $G(s)$ represents the actual transfer function (i.e., the plant) from the input (disturbance) to the output. $U(s)$ and $D(s)$ are the system input and disturbance input in the Laplace domain, respectively. $V(s)$ is the system output. The system block diagram is shown in Fig. 4.1.

$$V(s) = G(s)[U(s) + D(s)]. \tag{4.1}$$

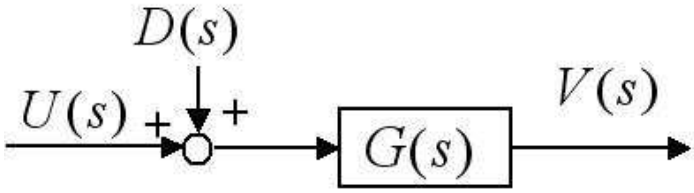

Figure 4.1: System block diagram

In practice, the model that we use to describe the actual plant can not ever fully embody all the dynamic properties of the plant, no matter how we obtained the model. The mismatch between the two can be considered as an equivalent disturbance input and DOB can be used to compensate for its effect. We sometimes call the model used for robust controller design the nominal model. Once DOB effectively removes the disturbance input (the mismatch between the actual plant and the plant model), the relationship between the overall system output and the input can resemble that of the nominal plant model. This way, we can force the actual plant to mimic the dynamic properties of the nominal plant model with reasonable DOB design. Nagata and Tomizuka [28] used a DOB design and realized desired plant behavior in an engine torque control application through taking the desired plant model as the nominal plant model.

For the system described in Eq. (4.1), we denote the nominal plant model as $G_n(s)$. The general DOB structure is shown in Fig. 4.2. The part above the dashed line

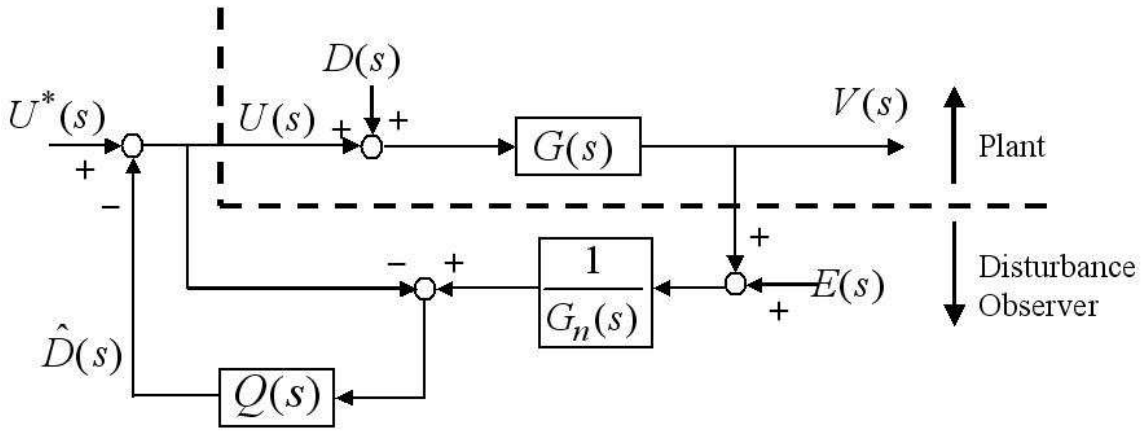

Figure 4.2: General DOB structure

represents the actual plant with an external input $U(s)$ and a disturbance input

$D(s)$. The part below the dashed line represents the DOB structure. $E(s)$ is the measurement noise and $\hat{D}(s)$ is the disturbance estimation. Intuitively, if we process the plant output by the exact plant inverse, we should get back the original plant input. The plant input consists of the external input and the disturbance input. If the exact amount of the external input is known, an estimate of the disturbance amount can be obtained. By subtracting the estimated disturbance estimate from the plant's external input, we can cancel the disturbance and eliminate the disturbance's impact on the plant. In reality, however, the plant model is always different from the actual plant and we can only pass the plant output through the inverse of the nominal plant model, as shown in Fig. 4.2. Notice that $1/G_n(s)$ is usually unrealizable and we need to add the filter $Q(s)$ to make $Q(s)/G_n(s)$ realizable, i.e., the order of the denominator greater than or equal to the order of the numerator. The design of the Q-filter usually is the most important part in DOB design. As we will see later on, it is related to a lot of contradicting criteria and requires trade-off considerations.

To understand how DOB works, let us first suppose that $Q(s) = 1$ for all frequencies in Fig. 4.2. Then we have the following expression.

$$U(s) = U^*(s) - \left[\frac{G(s)}{G_n(s)}[U(s) + D(s)] + \frac{1}{G_n(s)}E(s) - U(s)\right]. \tag{4.2}$$

Solving Eq. (4.2) for $U(s)$, we get

$$U(s) = \frac{G_n(s)}{G(s)}U^*(s) - D(s) - \frac{1}{G(s)}E(s). \tag{4.3}$$

Therefore, the plant output $V(s)$ can be expressed as

$$V(s) = G_n(s)U^*(s) - E(s). \tag{4.4}$$

Notice that now the input-output relationship between $U^*(s)$ and $V(s)$ are characterized by the nominal plant model $G_n(s)$. Furthermore, if the output measurement is noise free, $E(s)$ disappears from Eq. (4.4) and the system performs exactly as the nominal plant model.

Given the above expressions, we can obtain the disturbance estimation $\hat{D}(s)$ as follows

$$\hat{D}(s) = \left(\frac{G_n(s)}{G(s)} - 1\right)U(s) + \frac{1}{G(s)}E(s) + \frac{G(s)}{G_n(s)}D(s). \tag{4.5}$$

If the nominal plant model $G_n(s)$ is the same as the actual plant $G(s)$, and the output measurement is noise free ($E(s)$=0), we have $\hat{D}(s) = D(s)$, meaning that the

disturbance estimation is the same as the disturbance itself. This is the reason that the structure in Fig. 4.2 is called the disturbance observer. In the presence of model mismatch, the difference between the two is included in the disturbance estimation as shown in Eq. (4.5).

However, the Q-filter can not be equal to one for all frequencies, since $1/G_n(s)$ is unrealizable and we have to make $Q(s)/G_n(s)$ proper by letting the relative order of $Q(s)$ greater than or equal to that of $G_n(s)$. If we drop the assumption of $Q(s) = 1$, the output of the system shown in Fig. 4.2 can be expressed as follows.

$$V(s) = G_{uv}U^*(s) + G_{dv}(s)D(s) + G_{ev}(s)E(s), \tag{4.6}$$

where

$$\begin{aligned} G_{uv}(s) &= \frac{G(s)G_n(s)}{G_n(s) + (G(s) - G_n(s))Q(s)}, \\ G_{dv}(s) &= \frac{G(s)G_n(s)(1 - Q(s))}{G_n(s) + (G(s) - G_n(s))Q(s)}, \\ G_{ev}(s) &= -\frac{G(s)Q(s)}{G_n(s) + (G(s) - G_n(s))Q(s)}. \end{aligned} \tag{4.7}$$

As we can see from Eqs. (4.6) and (4.7), if $Q(s) \approx 1$, the three transfer functions from the input $U(s)$, the disturbance $D(s)$ and the measurement noise $E(s)$ to the output $V(s)$ become

$$G_{uv}(s) \approx G_n(s), G_{dv}(s) \approx 0, G_{ev}(s) \approx -1. \tag{4.8}$$

This is exactly the relationship shown in Eq. (4.4). On the other hand, if $Q(s) \approx 0$, the three transfer functions become

$$G_{uv}(s) \approx G(s), G_{dv}(s) \approx G(s), G_{ev}(s) \approx 0, \tag{4.9}$$

which make Eq. (4.6) the open loop dynamics.

From the above observations, we can see that for the frequencies where the disturbance is prominent, the Q-filter's magnitude should be close to 1 to make $G_{dv}(s)$ close to zero. For the frequencies where the measurement noise is large, the Q-filter's magnitude should be close to zero to make $G_{ev}(s)$ close to zero. Usually, the disturbances exist in the low frequency range and the measurement noise exists in the high frequency range. Notice that the Q-filter need to be close to zero in the high frequency

range also because of the fact that the relative order of $Q(s)$ should be greater than or equal to that of $G_n(s)$. Such situation makes a low-pass type of Q-filter a sensible choice. In fact, most of the DOB applications adopt low-pass Q-filter designs. However, there are also applications where a band-pass type of Q-filter is selected to filter out the narrow-band disturbance which exists in the mid-high frequency range [10]. Such a band-pass Q-filter design can strengthen the signal-to-noise ratio when the dominant disturbance is blended in a broad band disturbance spectrum. The resulting DOB can remove the dominant disturbance component more effectively. In our EPB application, a low-pass type Q-filter is chosen and the selection of its cut-off frequency is related to both stability and performance criteria, such as, response time, noise rejection, robust stability, etc.

4.2 DOB structure

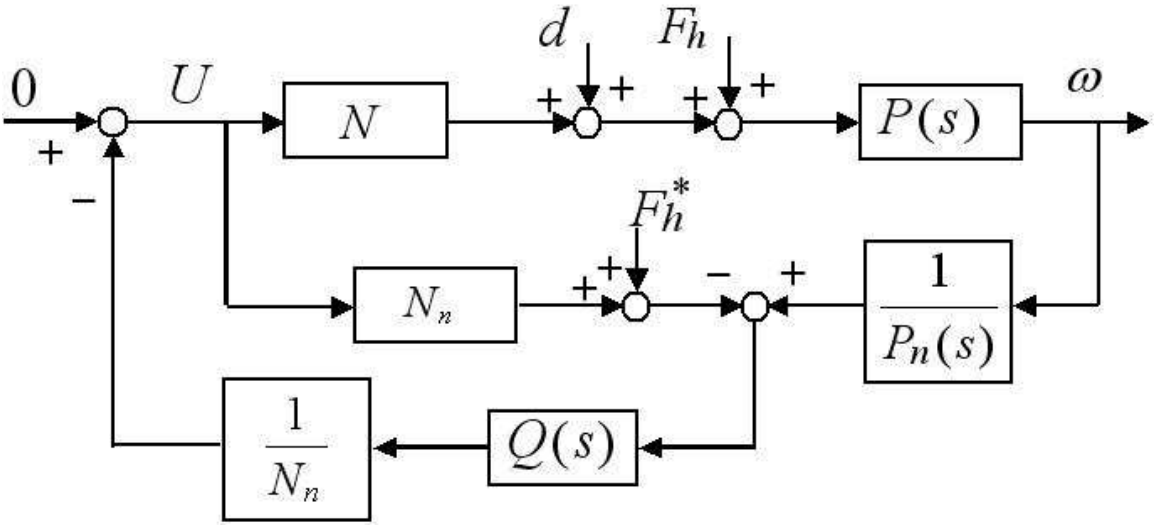

Figure 4.3: A DOB design for the system in Fig. 3.6

A DOB for the estimation and rejection of the environmental disturbance can be constructed as in Fig. 4.3, where $P(s) = 1/(J_{eq}s + B_{eq})$. Notice that in the original plant (Fig. 3.6), the rider's input force comes into the system at the same location as the environmental disturbance does. If we were to use a traditional DOB design without any modifications, the human input F_h would also be canceled out by the DOB. To avoid the cancellation of F_h by DOB, we add the measured human input F_h^*

in the DOB structure, as shown in Fig. 4.3. If $P(s) = P_n(s)$, $z = F_h + d + N \cdot u$. If, in addition, the measured human input is exactly the same as the real human input, i.e. $F_h^* = F_h$, then the added signal F_h^* will cancel out F_h contained in signal z and the detected disturbance signal $\hat{d}$ does not contain F_h. Even though $F_h^* \neq F_h$ in the actual system because of the existence of measurement noise, the difference between the two is usually small and the proposed structure assures that the human's pedaling input is not canceled by DOB.

The transfer function from the disturbance d to the angular velocity ω can be calculated with the aid of a series of block diagram transformations as shown in Fig. 4.4. From Fig 4(c), we get

$$T_{d\to\omega}(s) = \frac{(1 - Q(s))P(s)N_nP_n(s)}{N_nP_n(s) + Q(s)(NP(s) - N_nP_n(s))}. \tag{4.10}$$

If Q(s) is close to 1, then the value of $(1 - Q(s))$ is close to 0. The influence of the disturbance can be almost completely canceled. Thus, we have to design Q-filter such that its value is close to 1 at the frequencies where the disturbance is nonzero. For our system, the disturbance d is at low frequencies. Therefore, the Q-filter should be of the form of a low-pass filter.

4.3 H-infinity design

4.3.1 Uncertain variables in the system

Because of limitations in measurement precision, there exist uncertainties in the motor torque constant K_t, the motor inertia J, the friction constant B and the back-emf constant K_b. The coefficient $D = C_{dr}$ is the dynamic rolling resistance. Its value depends on the road condition and the tire inflation condition. It will vary a lot from hard ground to soft ground and from fully inflated tires to deflated tires, which constitutes a source of uncertainty. The most uncertain parameter in the sense of pure value changes in our model is the weight of the rider, which can have a great influence to the system's stability. In the following section, we will combine these uncertainties into one multiplicative uncertainty of the system and use it for the robust DOB design.

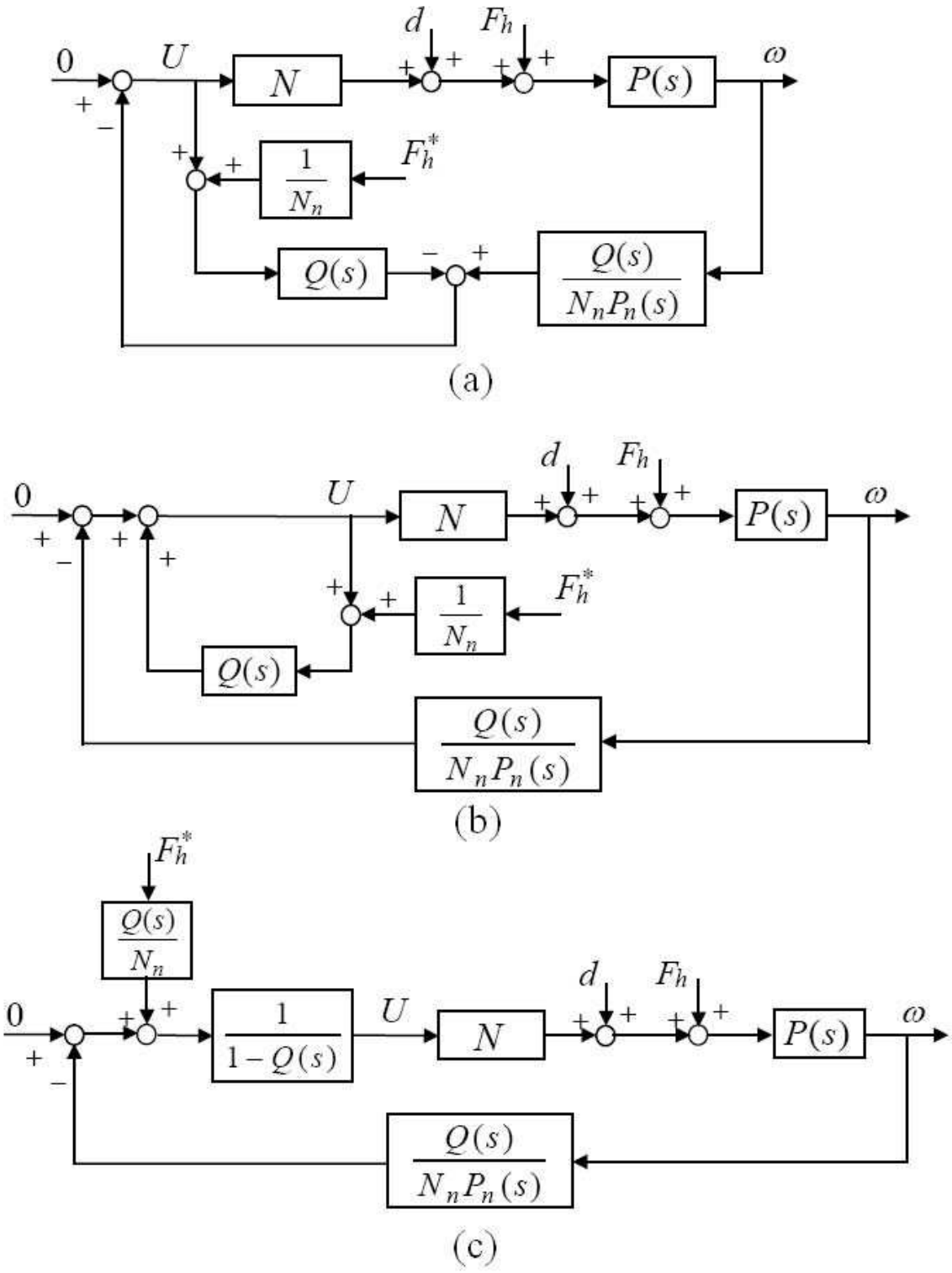

Figure 4.4: Sequential block diagram transformation

4.3.2 Calculate the multiplicative uncertainty bound

In designing robust controllers, we usually combine different sources of uncertainties into a multiplicative or additive uncertainty and find a lumped uncertainty upper bound as the worst case scenario. Here we choose the multiplicative uncertainty of the form

$$G(s) = G_n(s)\left(1 + w_I(s)\Delta_I(s)\right); |\Delta_I(j\omega)| \leq 1, \forall\omega, \tag{4.11}$$

where $G_n(s)$ is the nominal plant model and $G(s)$ represents a group of possible plants that deviate no more than the uncertainty bound $w_I(s)$ around the nominal model. $\Delta_I(s)$ represents all stable transfer functions with $|\Delta_I(j\omega)| \leq 1$ at all frequencies. For our plant, $G(s) = NP(s), G_n(s) = N_nP_n(s)$.

We use the following values as the nominal values of the uncertain parameters:

$$\begin{aligned} K_{tn} &= 2.58 \times 10^{-1} N \cdot m/A; \\ J_n &= 3.51 \times 10^{-1} N \cdot m \cdot s^2/rad; \\ B_n &= 9.27 \times 10^{-3} N \cdot m \cdot s/rad; \\ m_{Tn} &= 110kg; D_n = 1.00 \times 10^{-1} N \cdot s/m, \end{aligned} \tag{4.12}$$

where K_{tn}, J_n and B_n are the motor parameters identified through the motor system identification; m_{Tn} is the total nominal mass of the bicycle and the rider, and it is assumed to be $110kg$. Since the bicycle used in our experiment weighs around $30kg$, the nominal weight of the rider is assumed to be $80kg$. Notice that D_n is the nominal value for the dynamic rolling resistance C_{dr} of the bicycle and it is suggested by [29] that the nominal value can be taken as $D_n = 1.00 \times 10^{-1} N \cdot s/m$. We consider $\pm 20\%$ changes in K_{tn}, J_n, B_n and D_n. According to [30], the average mass for a large man is 141 kilograms, while the average mass for a skinny man is 47.18 kilograms. The corresponding average masses for women are 88.45 kilograms and 43.09 kilograms. We choose the range of human mass to be considered as [40kg, 140kg], which makes the range of m_T to be [70kg, 170kg]. The ranges for all the uncertain parameters are

listed below:

$$\begin{aligned} K_t &\in [2.06 \times 10^{-1}, 3.10 \times 10^{-1}] N \cdot m/A; \\ J &\in [2.81^{-1}, 4.21 \times 10^{-1}] N \cdot m \cdot s^2/rad; \\ B &\in [7.42 \times 10^{-3}, 1.11 \times 10^{-2}] N \cdot m \cdot s/rad; \\ m_T &\in [70, 170] kg; \\ D &\in [8.00 \times 10^{-2}, 1.20 \times 10^{-1}] N \cdot s/m. \end{aligned} \tag{4.13}$$

Through sampling a large amount of possible plants within the above ranges using MATLAB Robust Control Toolbox's "usample" command, we propose the uncertainty bound as

$$w_I(s) = \frac{50s + 0.25}{55.56s + 1}, \tag{4.14}$$

which is drawn in Fig. 4.5. The solid lines represent 30 possible bode plots for

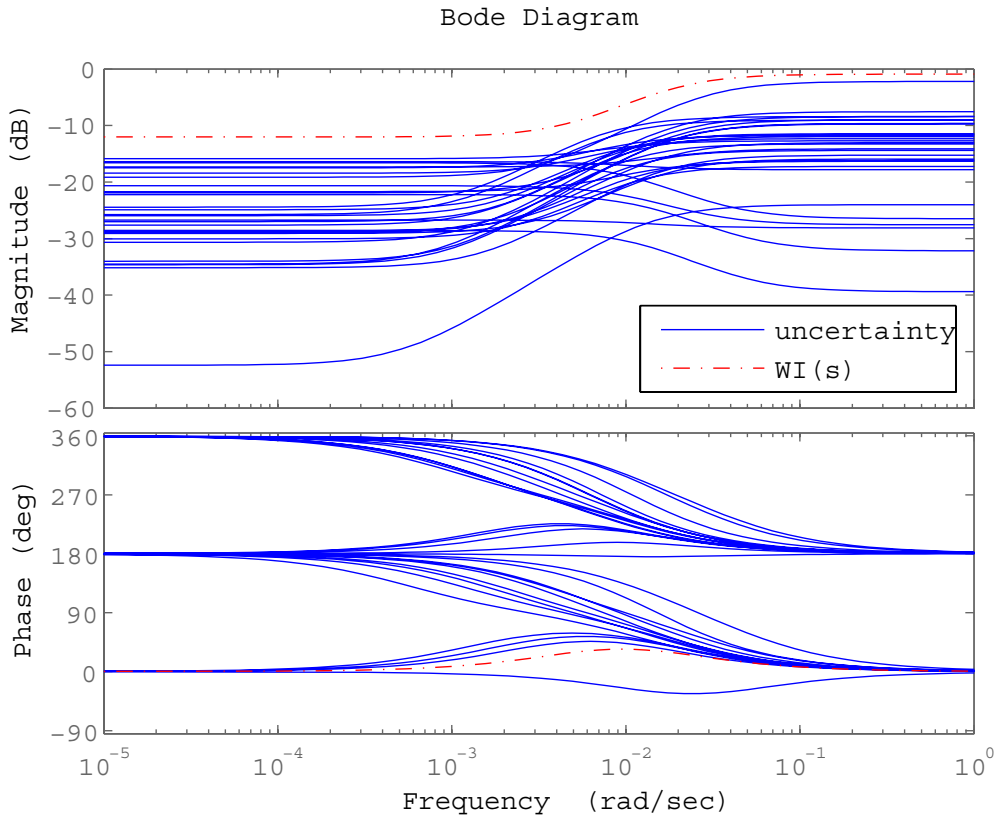

Figure 4.5: Test on the uncertainty bound $w_I(s)$

$[G(s)-G_n(s)]/G_n(s)$ corresponding to 30 possible plants. The dash-dot line represents the proposed uncertainty bound $w_I(s)$, which has $w_I(s) \geq [G(s) - G_n(s)]/G_n(s), \forall s$.

4.3.3 Robust stability criterion for the uncertain plant

For a system with multiplicative uncertainty as shown in Fig. 4.6, the loop transfer

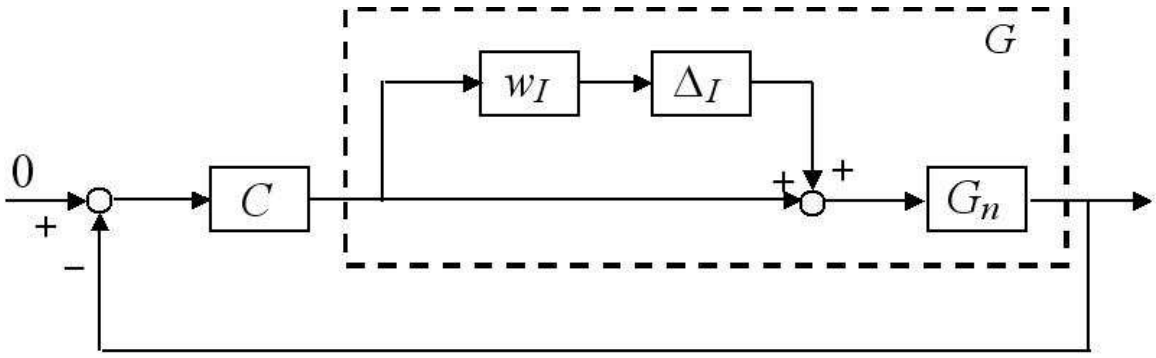

Figure 4.6: Plant with multiplicative uncertainty

function is

$$L = GC = G_nC(1 + w_I\Delta_I) = L_n + w_IL_n\Delta_I, \tag{4.15}$$

where $|\Delta_I(j\omega)| \leq 1, \forall\omega$; $L_n = G_nC$ is the nominal loop transfer function. If we assume that the nominal closed-loop system is stable, the Nyquist stability condition tells us that the robust stability of the perturbed system can be guaranteed if L does not encircle the point (-1,0). From Fig. 4.7, we can see that this condition can be satisfied if

$$|w_I(j\omega)L_n(j\omega)| < |1 + L_n(j\omega)|, \forall\omega. \tag{4.16}$$

The above condition is the same as

$$\|w_I(s)T_n(s)\|_\infty < 1, \tag{4.17}$$

where $T_n(s) = L_n(s)/[1 + L_n(s)]$ is the nominal complimentary sensitivity function.

From the transformed block diagram in Fig. 4.4, we can see that the controller and the nominal plant for our system can be expressed as

$$C(s) = \frac{Q(s)}{[1 - Q(s)]N_nP_n(s)};$$
$$G_n(s) = N_nP_n(s). \tag{4.18}$$

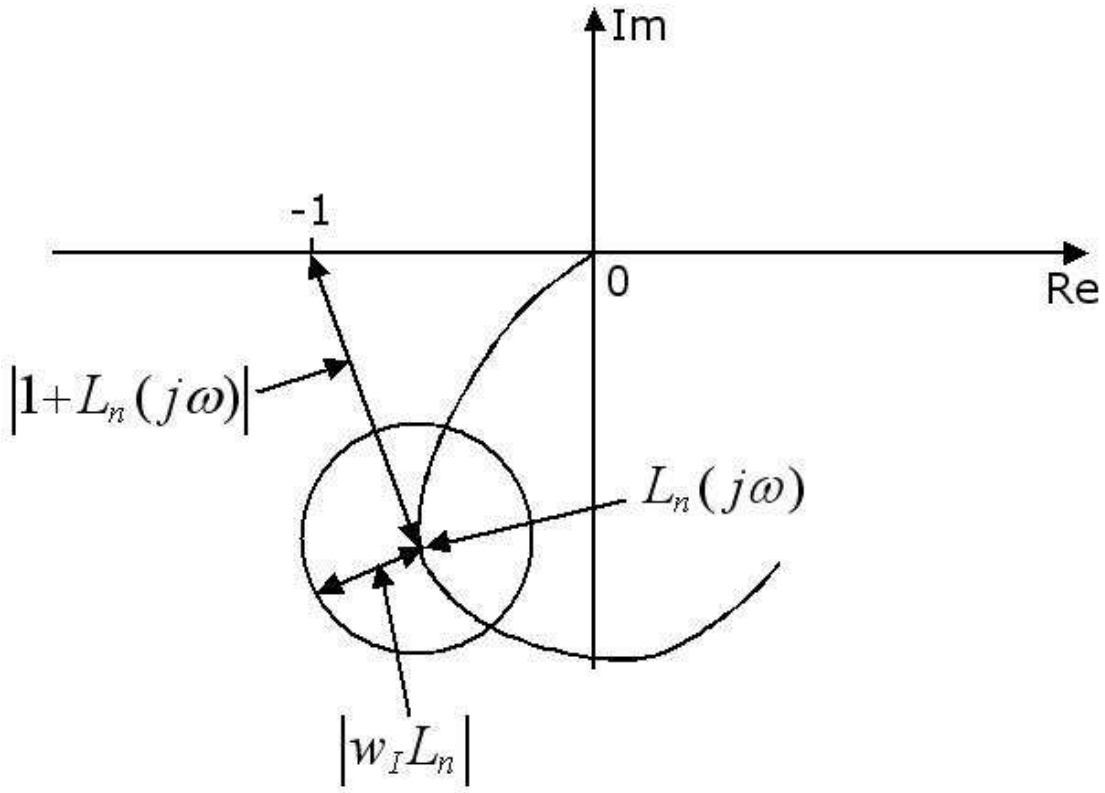

Figure 4.7: Pictorial interpretation of the robust stability condition

The nominal loop transfer function is

$$L_n(s) = C(s)G_n(s) = \frac{Q(s)N_nP_n(s)}{[1-Q(s)]N_nP_n(s)} = \frac{Q(s)}{1-Q(s)}. \tag{4.19}$$

The nominal complimentary sensitivity function can then be calculated as

$$T_n(s) = \frac{L_n(s)}{1+L_n(s)} = Q(s). \tag{4.20}$$

From (4.17), we know that the robust stability criterion for our system is

$$\|w_I(s)Q(s)\|_\infty < 1, \tag{4.21}$$

which is equivalent to

$$|Q(j\omega)| < 1/|w_I(j\omega)|, \forall\omega. \tag{4.22}$$

4.3.4 Q-filter design

The essence of disturbance observer design is selecting an appropriate Q-filter. Besides the robust stability criterion stated above, Q-filter design also involves other factors, such as response time and noise rejection. For the EPB system, it is important to consider the following items in the DOB design.

1. Robust stability: $|Q(j\omega)| < 1/|w_I(j\omega)|, \forall\omega$.
2. Properness: $Q(s)/[N_nP_n(s)]$ is realizable, i.e. proper.
3. Disturbance rejection: $Q(s) = 1$ around the frequencies where the disturbance $d \neq 0$ (i.e. low frequencies).
4. Fast response: The response time of the disturbance observer depends on the bandwidth of the Q-filter. Fast response means large Q-filter bandwidth.
5. Good noise rejection: High frequency measurement noise[1]exists in the velocity measurement. The transfer function from the measurement noise to the control input is $T_{noise\to u}(s) = -Q(s)/[N_nP_n(s)]$. Good noise rejection means low Q-filter bandwidth and fast roll-off at high frequencies.

[1]Measurement noise is not shown in Fig. 4.3 or any other transformed figures. However, measurement noise does exist and it enters the system through the angular velocity measurement right before the block $1/P_n(s)$ in Fig. 4.3.

6. Robustness to unmodeled dynamics: Unmodeled dynamics exist in high frequencies and robustness requires low-gain at high frequencies, which means low bandwidth of the Q-filter.

7. Easy implementation: Although higher order Q-filters have faster roll-off at high frequencies providing better noise rejection and robustness, an excessively high order Q-filter can be too complicated to implement in real-time.

Based on the above design criteria, we chose the Q-filter to be a second order low-pass filter

$$Q(s) = \frac{1}{(s+1)^2}, \tag{4.23}$$

which achieves an acceptable trade-off among all the factors mentioned above. Figure 4.8 shows that the robust stability criterion in (4.22) was satisfied with the chosen Q-filter in (4.23).

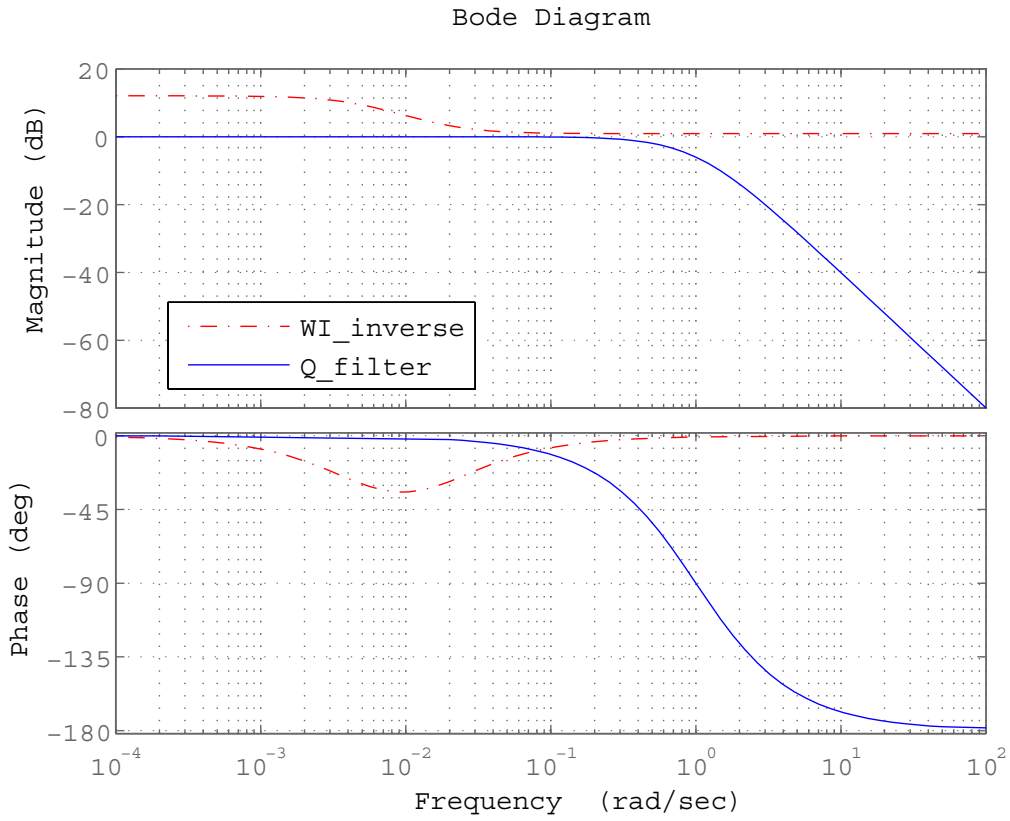

Figure 4.8: Robust stability criterion

4.4 Experimental results

The efficiency of the proposed robust disturbance observer was tested through real road tests on an EPB. Note that we did not introduce any proportional power assistance into the system, i.e., no other assistance was provided to the rider except the environmental disturbance compensation from the DOB. The experimental bicycle was modified from a commercially available EPB. The torque sensor was mounted inside the crankset system and it measures the instantaneous human pedaling torque. The velocity measurements came from the encoder inside the front wheel hub motor. The encoder has a resolution of 243 pulses per revolution. Differentiation was used to get the angular velocity measurement from the encoder signal. As one can expect, the differentiation induced high frequency noise in the velocity measurement as shown in the first plot in Fig. 4.9. As stated in the previous section, lowering the Q-filter bandwidth can solve this problem. The DOB was implemented with LabVIEW on a laptop, which was carried with the bicycle during the experiment. The sampling frequency of the controller was set to $10Hz$.

The road test was done on a slope of about 3 degrees. The weight of the cyclist was 65 kilograms. Based on nominal values of the uncertain parameters, we calculated the nominal environmental disturbance as $d = -51.47N$. Using the nominal value of N, we get the nominal steady state motor input $u_{ssn} = |d| / N_n = 2.79volt$. As shown in the experimental results in Fig. 4.9, the steady state motor input is around 2 volt. This shows a good agreement with the expected nominal value. The small mismatch was caused by the inaccuracy of the nominal parameter values.

The experimental results showed that the robust DOB was able to catch up with the slope changes and compensate for the environmental disturbance. With the DOB power-assistance, riding uphill feels like riding on level ground to the cyclist. The human torque input in the second plot of Fig. 4.9 shows that the human input becomes close to zero after 10 seconds, which corresponds to the behavior of coasting on level ground at a certain speed level. We should mention that since the lumped uncertainty bound was used in the Q-filter design, the resulting closed-loop performance might be conservative.

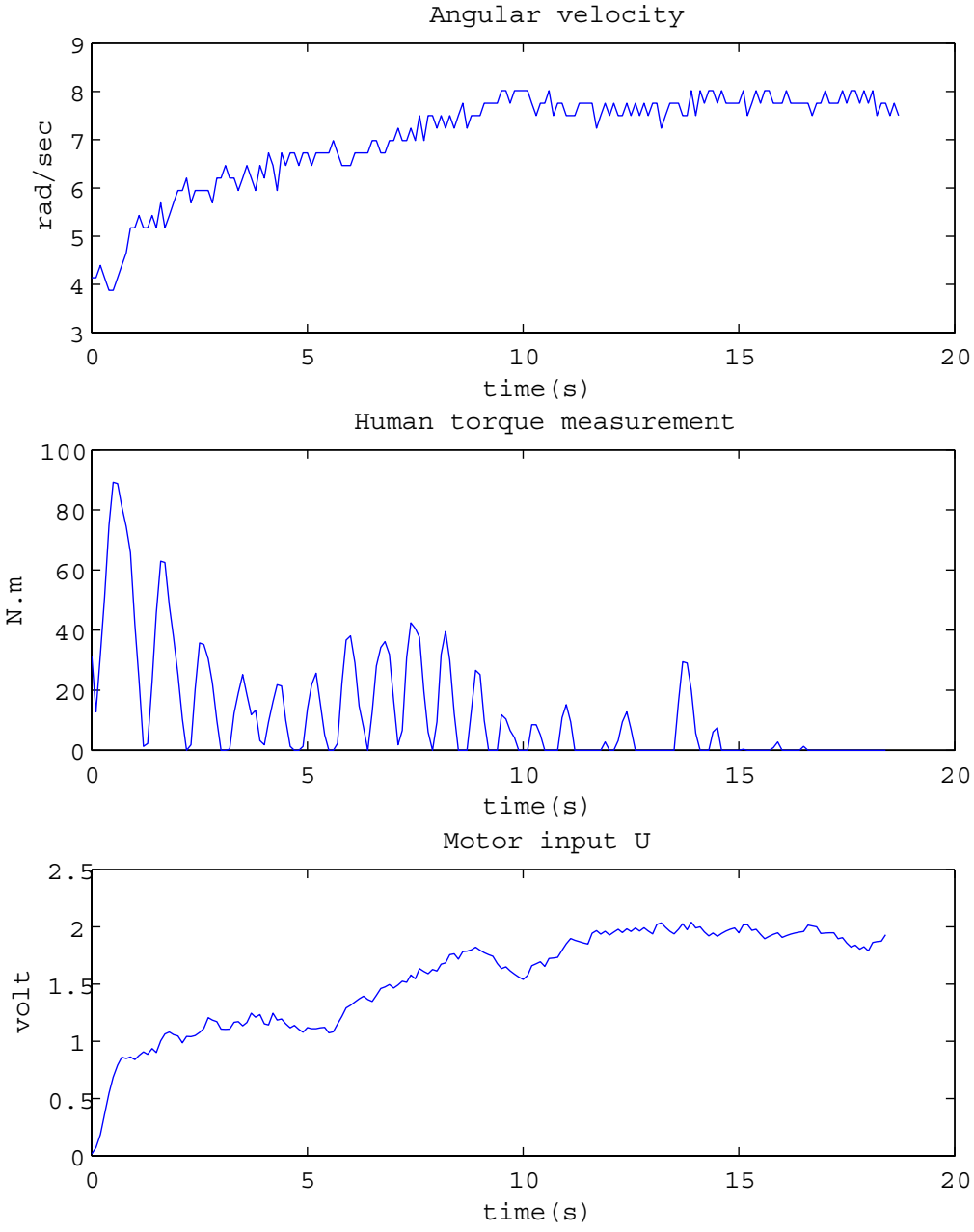

Figure 4.9: Real road experimental results

4.5 Robust DOB anti-windup design and experimental results

The front-wheel hub motor has an input saturation at 5 volts due to the motor drive's design and the motor's capability. Actuator windup will occur if the DOB structure shown in Fig. 4.3 is used and the motor control input exceeds 5 volts. To avoid the unwanted phenomenon, we employ the modified DOB structure shown in Fig. 4.10. The "actual saturation" block in the figure represents the actual motor saturation

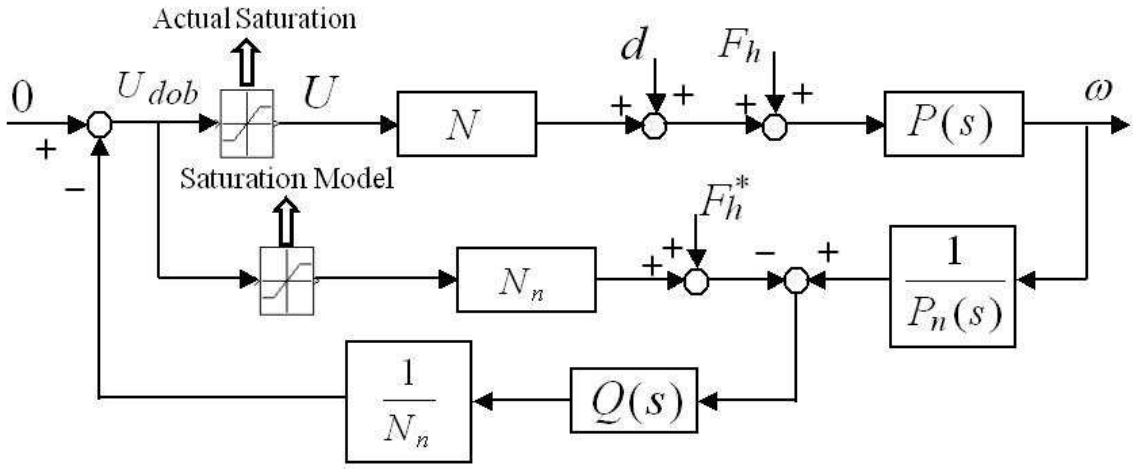

Figure 4.10: Modified DOB structure with motor input saturation

existed in the experimental EB system. Note that although this block physically exists in the experimental system, we still include a saturation block from 0 to 5 volts in the controller structure (after the calculated DOB signal U_{dob}) to protect the motor and motor drive. The "saturation model" block is introduced so that the DOB takes the real motor input into the calculation of the environmental disturbance. The modified DOB structure can estimate the level of environmental disturbance in the EB system in the presence of motor input saturation, and apply corresponding assistance through the hub motor within the motor's capability, i.e., avoiding the motor's input saturation. Figure 4.11 shows the real road experimental results with the modified DOB power-assistance scheme when motor saturation exists. We can see that the DOB picked up the disturbance level quickly and the motor input saturated after around 4 seconds. Although the estimated disturbance level should require motor input at around 10 volts, as shown in the third plot of Fig. 4.11, the motor can only

help with the maximum input of 5 volt. The experimental results showed that the modified DOB worked in the presence of motor input saturation.

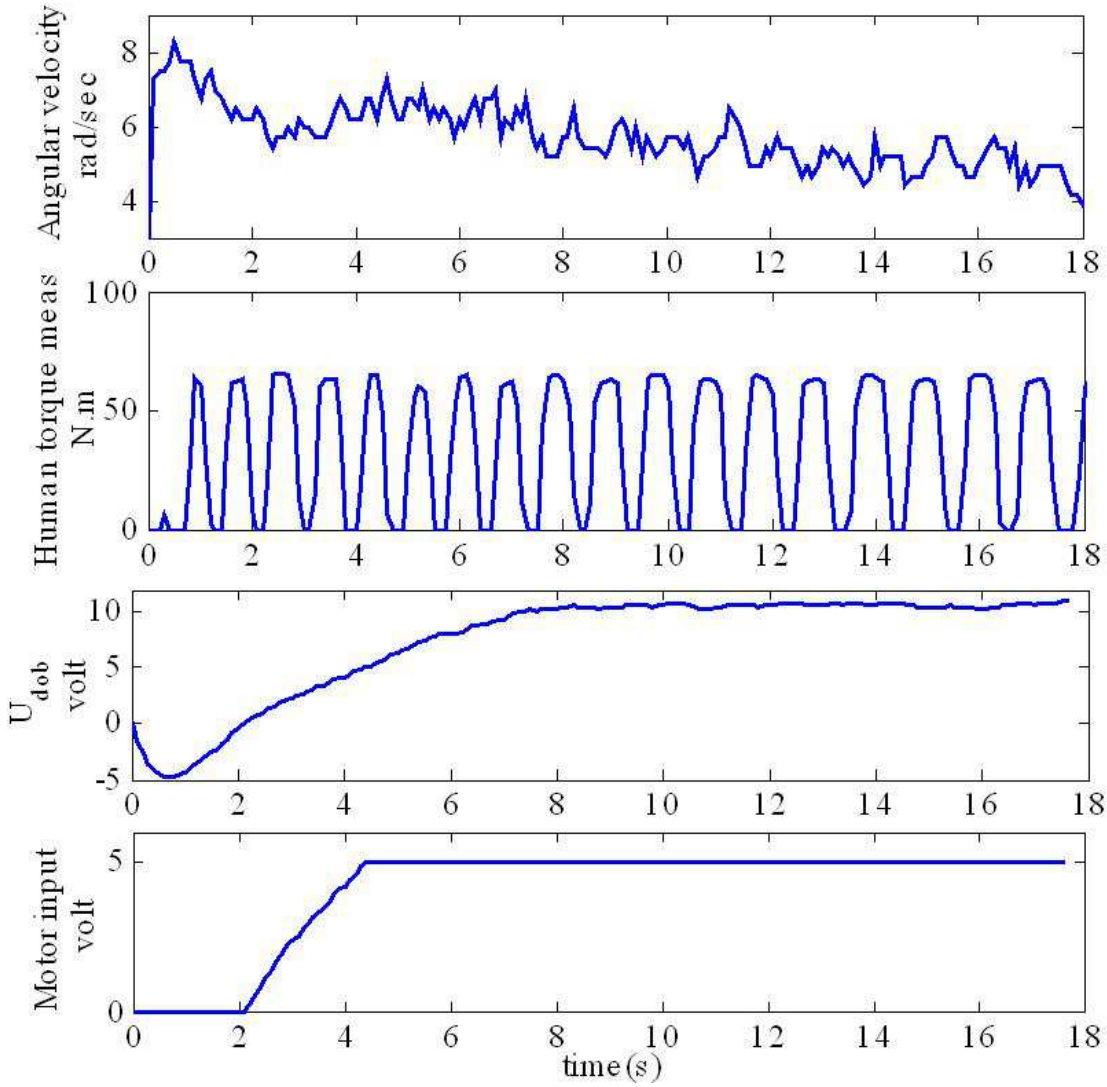

Figure 4.11: Experimental results with modified DOB

Chapter 5

Non-Uniform Human Input Compensation

As we have discussed in Chapter 4, the traditional proportional power-assist scheme (usually 1:1 power-assistance) may not be sufficient in providing a smooth and comfortable ride during uphill riding. The robust DOB approach that we introduced in Chapter 4 can detect and compensate for the environmental drag force (which contains gravity as a major part) experienced in uphill riding. This scheme provided extra flexibility compared with the proportional power-assistance scheme in the uphill riding situation. However, neither of the two schemes addressed the issue of uncomfortable uphill riding caused by the non-smooth velocity and acceleration profiles. Due to the design of the crankset on a bicycle, the torque input from human traces a sinusoidal-like pattern by nature. The human input torque reaches its local maximum (minimum) twice during a complete pedal cycle. As shown in Fig. 5.1, the maximum torque is achieved at or around the horizontal positions, and the local minimum torque is achieved at or around the vertical positions. Figure 5.2 shows a real-time measurement profile of the human input torque during uphill riding. Note that the bicycle started on level ground and continued with uphill riding after around 50 seconds. We can see that during uphill riding, the peak torque value is at least 5 or more times the minimum torque value. This huge fluctuation will in turn cause big fluctuation in the bicycle's longitudinal acceleration and velocity, as shown in Eq. (3.2). The non-smoothness in velocity and acceleration becomes more noticeable during uphill riding, and thus, causes discomfort. We propose that

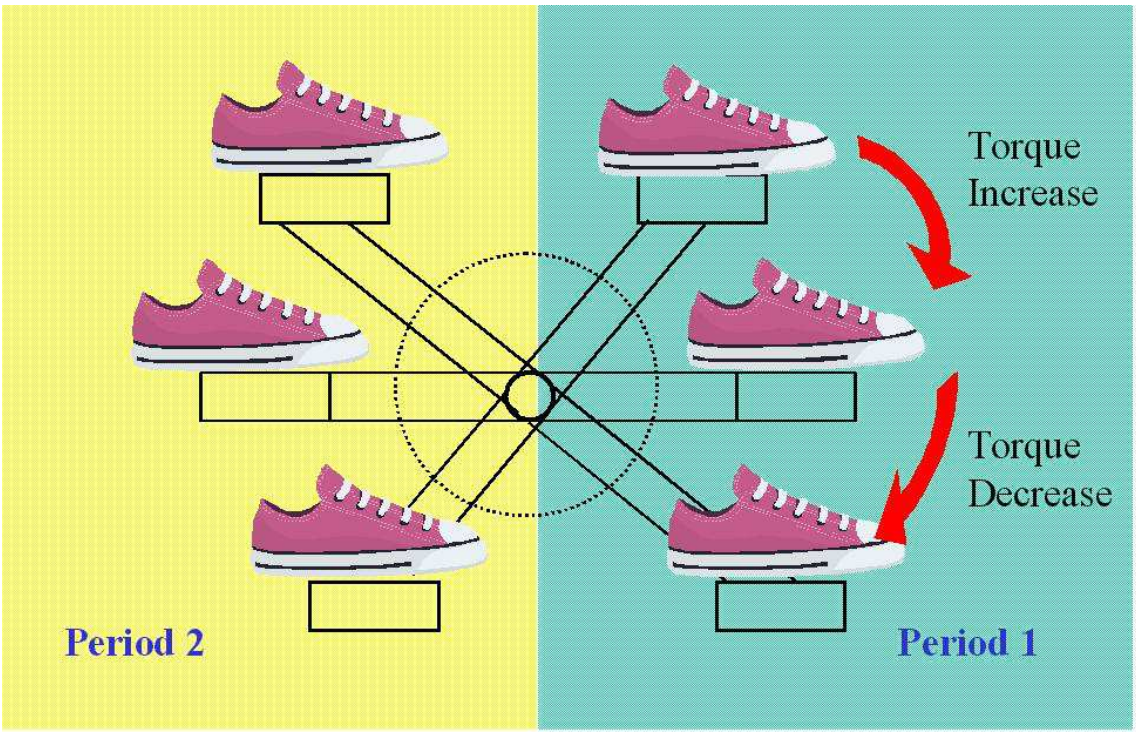

Figure 5.1: Human torque input changes during a complete pedal cycle

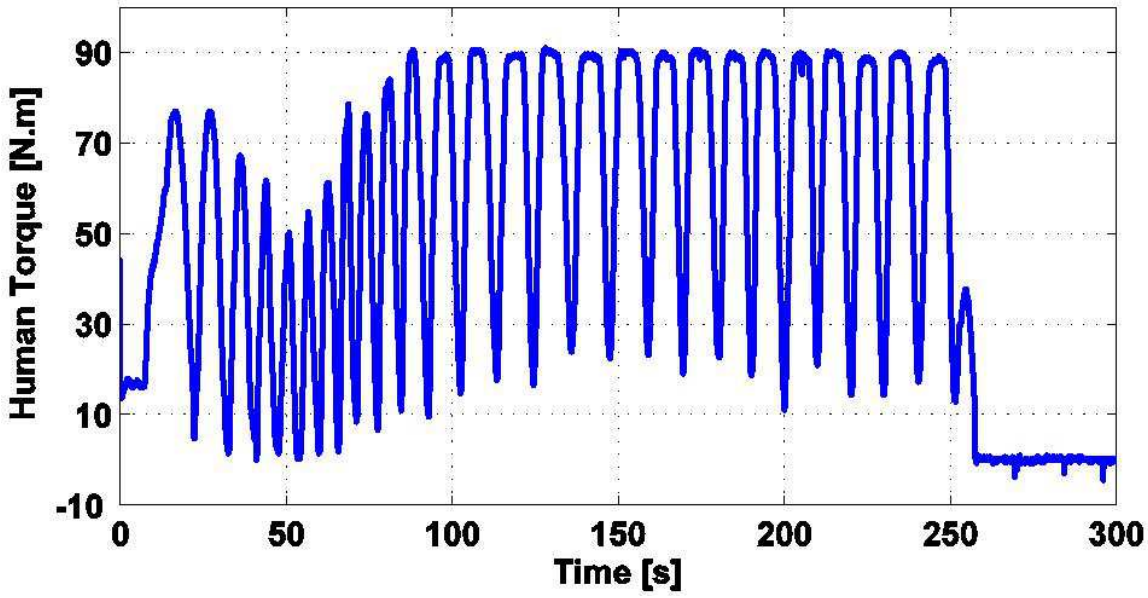

Figure 5.2: Real-time measurement profile of the human input torque during uphill riding

through applying repetitive control based power-assist schemes, we can compensate for the sinusoidal-like oscillation in the velocity and acceleration profiles and ease the discomfort.

Repetitive control is often used for periodic disturbance rejection and/or periodic reference signal tracking. It has been successfully applied in many motion control problems involving rotary motions, such as hard disk drives [16] [31] [32] and Compact Disc players [17] [33]. It has also been applied to noncircular motion control applications [18] [34]. A more general review of the methods to deal with periodic disturbances and recent applications of repetitive control can be found in Tomizuka [1]. Repetitive controllers are designed based on the internal model principle (IMP) [35]. Through incorporating the internal model of the disturbance signal in the controller denominator, repetitive controllers pose an infinitely high gain at the disturbance frequency in the open loop frequency response, and, thus, reject the repetitive disturbance.

In this chapter, we model the human input as a signal with non-zero DC component and use repetitive control to reject the oscillatory sinusoidal-like part of the signal, while augmenting the DC part of the human input. We consider two ways of modeling the sinusoidal-like signal in the human input, i.e., one as a sinusoidal signal, and the other as a nonsinusoidal but periodic signal. These two modeling methods give different internal models for the oscillatory component of the human's torque input. To be specific, when modeled as a sinusoidal signal, the oscillation source has an internal model of $1 - 2cos\omega_h q^{-1} + q^{-2}$, where q^{-1} is a backward shift operation and ω_h is the frequency of the sinusoid. The internal model for a non-sinusoidal periodic signal is $1 - q^{-N}$, where N is the period of the periodic signal.

The fundamental assumption in the design of repetitive control is that the period of the repetitive signals is known and fixed. In the EPB application, the period is known but not fixed. Since the human input's frequency is changing from time to time while the bicycle is in motion, the above-mentioned models are both time-varying. We deal with the two time-varying internal models in two respective ways. For the sinusoidal model, the changing frequency is considered as a changing parameter, and an adaptive handling manner is adopted. For the nonsinusoidal periodic model, each pedal revolution is sliced into N_s sectors so that the period of the signal in the discrete time domain is N_s and fixed. This way, the sampling period for the repetitive control depends on the pedaling speed and the bicycle dynamics become

time-varying. Repetitive controllers based on the two different internal models will be considered in this chapter and their performance will be compared with simulation results. Furthermore, experimental results for the second method will be shown to verify the effectiveness of the controller design.

5.1 Internal model principle

The principle of including known disturbance modes into the feedback controller structure in order to reject the very disturbance input of concern is called the internal model principle (IMP). It was first introduced by Francis and Wonham in 1975 [35]. The analysis of IMP below follows that in [36].

The internal model principle in continuous time domain can be explained using the feedback control system shown in Fig. 5.3. The system has a disturbance input $D(s) = B_d(s)/A_d(s)$ with known modes $A_d(s)$. In order to achieve asymptotic regulation in this system, i.e., $\lim_{t\to\infty} e(t) = 0$, we have to include the modes of $D(s)$ in the denominator of the controller $G_c(s)$. Note that the plant zeros can not cancel any of the disturbance modes in the controller. If we write $G_p(s) = B_p(s)/A_p(s)$, and

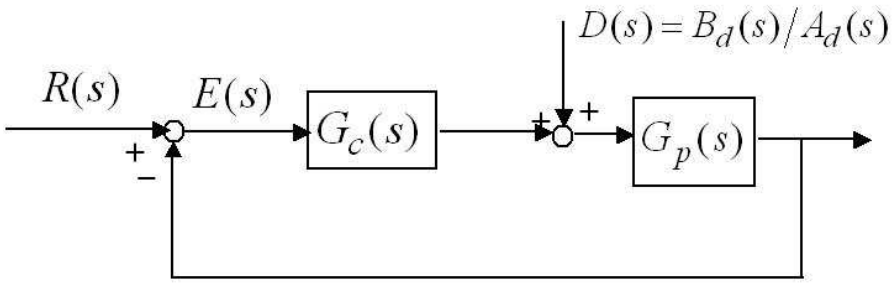

Figure 5.3: Continuous time feedback system with disturbance input $D(s)$

$G_c(s) = B_c(s)/A_c(s)$, the regulation error $E(s)$ can be expressed as

$$\begin{aligned} E(s) &= -\frac{G_p(s)}{1 + G_c(s)G_p(s)} D(s) \\ &= -\frac{B_p(s)A_c(s)}{A_p(s)A_c(s) + B_p(s)B_c(s)} \frac{B_d(s)}{A_d(s)}. \end{aligned} \tag{5.1}$$

Since we have included the disturbance modes in the controller $G_c(s)$'s denominator, $A_c(s)$ can be written as $A_c(s) = A'_c(s)A_d(s)$. Therefore, the error response becomes

$$E(s) = -\frac{B_p(s)A'_c(s)B_d(s)}{A_p(s)A_c(s) + B_p(s)B_c(s)} \tag{5.2}$$

If the controller is well designed and can make the closed loop system asymptotically stable, $E(s)$ contains all the asymptotically stable modes and the error $e(t)$ can converge to zero.

Since our controller design is carried out in the discrete time domain, we also need to consider the internal model principle in the discrete time domain. Let us consider the regulation of a controlled plant with a disturbance input $d(k)$ of the following type.

$$A_d(z^{-1})d(k) = 0 \tag{5.3}$$

Examples of such disturbances include:

1. $(1 - z^{-1})d(k) = 0$ for constant disturbances ($d(k)$=constant).
2. $(1-2\cos\omega z^{-1}+z^{-2})d(k) = 0$ for sinusoidal disturbances ($d(k) = sin(\omega k), cos(\omega k)$).
3. $(1-z^{-N})d(k) = 0$ for periodic disturbances with a period of N ($d(k) = d(k-N)$).

Notice that the disturbance is regarded as the output of a system with a characteristic polynomial of $A_d(z^{-1})$. That is, $D(z^{-1}) = B_d(z^{-1})/A_d(z^{-1})$. Let us expressed the plant as

$$G_p(z^{-1}) = \frac{z^{-d}B_p(z^{-1})}{A_p(z^{-1})}, \tag{5.4}$$

where z^{-d} represents a d-step delay. With the controller $G_c(z^{-1})$ expressed as

$$G_c(z^{-1}) = \frac{S(z^{-1}}{A_d(z^{-1})R(z^{-1})}, \tag{5.5}$$

the closed loop transfer function from the disturbance $D(z^{-1})$ to the error $E(z^{-1})$ is

$$\begin{aligned} G_{de}(z^{-1}) &= -\frac{G_p(z^{-1})}{1 + G_p(z^{-1})G_c(z^{-1})} \\ &= -\frac{z^{-d}B_p(z^{-1})/A_p(z^{-1})}{1 + (S(z^{-1})/A_d(z^{-1})R(z^{-1})) \cdot (z^{-d}B_p(z^{-1})/A_p(z^{-1}))} \\ &= -\frac{z^{-d}A_d(z^{-1})R(z^{-1})B_p(z^{-1})}{A_d(z^{-1})R(z^{-1})A_p(z^{-1}) + z^{-d}S(z^{-1})B_p(z^{-1})}. \end{aligned} \tag{5.6}$$

Therefore, the error

$$E(z^{-1}) = G_{de}(z^{-1})D(z^{-1}) = -\frac{z^{-d}R(z^{-1})B_p(z^{-1})B_d(z^{-1})}{A_d(z^{-1})R(z^{-1})A_p(z^{-1}) + z^{-d}S(z^{-1})B_p(z^{-1})}. \quad (5.7)$$

Notice that the denominator in Eq. (5.1) is the characteristic polynomial. If we properly place the closed loop poles so that all of them are inside the unit circle, then the closed loop system is asymptotically stable and the error $e(k)$ converges to zero over time. This means that asymptotic regulation of the plant is achieved under the presence of the disturbance satisfying $A_d(z^{-1})d(k) = 0$. The disturbance is asymptotically rejected. Notice that the internal model of the disturbance is included in the controller structure. This is the internal model principle in discrete time domain.

5.2 Repetitive control introduction[1]

Consider a discrete time system described by

$$\begin{aligned} A(q^{-1})y(k) &= q^{-d}B(q^{-1})[u(k) + w(k)], \\ A(q^{-1}) &= 1 + a_1q^{-1} + \cdots + a_nq^{-n}, \\ B(q^{-1}) &= b_0 + b_1q^{-1} + \cdots + b_mq^{-m}, \end{aligned} \quad (5.8)$$

where u and y are the input and output, respectively. q^{-1} is a one-step delay operator, and d is the total number of pure delays in the system. w is a period disturbance signal, which we want to reject using a repetitive controller.

For our EPB system, w is the fluctuating component in the human torque input. We decompose the human input into two parts, i.e.

$$F_h(t) = F_{ave}(t) + F_{fluct}(t), \quad (5.9)$$

where $F_{ave}(t)$ is the local average of the varying torque and $F_{fluct}(t)$ represents the torque variations around the average. Note that $F_{ave}(t)$ and $F_{fluct}(t)$ are both functions of time. In the frequency domain, $F_{ave}(t)$ contains the low frequency components while $F_{fluct}(t)$ consists of the high frequency components of the human input. $F_{ave}(t)$ may be extracted by processing $F_h(t)$ by a low pass filter, and $F_{fluct}(t)$ by a band pass filter to filter out measurement noise and obtain dominant fluctuation frequency

components. For low pass filtering, $F_h(t)$ may be processed by a standard low pass filter or by a box car filter as shown in Eq. (5.10).

$$F_{ave}(t) = \frac{1}{T_b} \int_{t-T_b}^{t} F_h(\tau)\, d\tau \tag{5.10}$$

Alternatively, if either $F_{ave}(t)$ or $F_{fluct}(t)$ is obtained, the other component may be acquired by subtracting the known part from $F_h(t)$. For example,

$$F_{fluct}(t) = F_h(t) - F_{ave}(t), \tag{5.11}$$

if $F_{ave}(t)$ has been obtained by filtering. Note that the discretized $F_{fluct}(k)$ corresponds to $w(k)$ in Eq. (5.8).

If $w(k)$ has a period of N_s, then

$$(1 - q^{-N_s})w(k) = 0. \tag{5.12}$$

Assume that the system in Eq. (5.8) is asymptotically stable and $B(q^{-1})$ can be decomposed into

$$\begin{aligned} B(q^{-1}) &= B^c(q^{-1})B^u(q^{-1}) \\ B^c(q^{-1}) &= b_0 + b_1^c q^{-1} + \cdots + b_{mc}^c q^{-mc} \\ B^u(q^{-1}) &= 1 + b_1^u q^{-1} + \cdots + b_{mu}^u q^{-mu} \end{aligned} \tag{5.13}$$

where $B^c(q^{-1})$ and $B^u(q^{-1})$ contain, respectively, cancellable zeros and uncancellable zeros. $B^u(q^{-1})$ is monic and its order is mu. The control objective is to achieve asymptotic regulation of the output, i.e., $\lim_{k\to\infty} e(k) = 0$, where $e(k) = y_d(k) - y(k)$ and $y_d(k)$ is the constant or periodic desired output with period N_s. A repetitive controller may be constructed with $(1 - q^{-N_s})$ in its denominator based on the IMP. However, this might cause instability due to unmodeled dynamics. Therefore, in practice, a low-pass filter $\mathbf{q}(q, q^{-1})$ is introduced into the internal model to enhance robustness. The robust repetitive controller[18] with a modified internal model isled dynamics. Therefore, in practice, a low-pass filter $\mathbf{q}(q, q^{-1})$ is introduced into the internal model to enhance robustness. The robust repetitive controller[18] with a modified internal model is

$$\begin{aligned} C_R(q) &= \frac{k_r \mathbf{q}(q, q^{-1}) z^{-N_s+d+mu} A(q^{-1})}{(1 - \mathbf{q}(q, q^{-1})q^{-N_s})B^c(q^{-1})b}, \ \mathbf{q}(q, q^{-1}) = \frac{h(q^{-1})h(q)}{h} \\ b &> \max_{\omega\in[0,\pi]} \left|B^u(e^{j\omega})\right|^2, \ h = \max_{\omega\in[0,\pi]} \left|h(e^{j\omega})\right|^2 \end{aligned} \tag{5.14}$$

under the constraint that $\mathbf{q}(q, q^{-1})q^{-N_s+d+mu}$ is causal. If the system modeling uncertainty is defined by

$$r(e^{-j\omega}) = \frac{P_0(e^{-j\omega}) - P(e^{-j\omega})}{P_0(e^{-j\omega})} \tag{5.15}$$

where $P_0(e^{-j\omega})$ represents the nominal dynamics of the system and $P(e^{-j\omega})$ the actual dynamics, q-filter must be selected to satisfy the following condition for robust stability,

$$\left|\frac{1}{r(e^{-j\omega})}\right| \geq \left|\mathbf{q}(e^{j\omega}, e^{-j\omega})\right|. \tag{5.16}$$

Another approach to design a repetitive control based intelligent power-assist algorithm for the EPB is to approximate the human torque fluctuation by a sum of sinusoidal signals

$$F_{fluct}(t) = \Sigma_{i=1}^{m}[a_i \sin(\omega_i t) + b_i \cos(\omega_i t)], \tag{5.17}$$

where $\omega_i = i \cdot \omega_p$ and ω_p is the pedaling frequency. Since sinusoidal signals satisfy

$$(1 - 2\cos(\omega_s T_s)q^{-1} + q^{-2})\sin(\omega_s T_s \cdot k) = 0, \tag{5.18}$$

where ω_s is the frequency in rad/s and T_s is the sampling period, an internal model of the form $1/(1 - 2\cos(\omega_s T_s)q^{-1} + q^{-2})$ can be constructed for repetitive control by utilizing this relation. If m in Eq.(5.17) is chosen to be large and all the frequency components' internal models are included in the repetitive controller, then the resulting controller will have similar disturbance rejection performance as the repetitive controller based on the internal model $1/(1 - q^{-N_s})$.

5.3 Repetitive controller in time domain

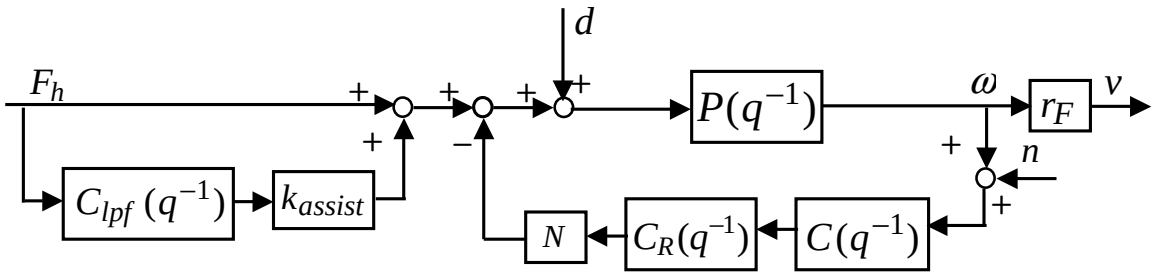

Figure 5.4: Overall repetitive control system structure

In the time domain design, we adopt the sinusoidal approximation idea in Eq.(5.17) and use only the frequency component with $\omega_h = 2 \cdot \omega_p$ to describe the human torque fluctuation. The overall control system structure is shown in Fig. 5.4, where $P(q^{-1})$ is the discretization of $P(s) = 1/(J_{eq}s + B_{eq})$. $C(q^{-1})$ represents a band-pass filter $C_{bpf}(q^{-1})$, which is a discretized version of the band-pass filter

$$C_{bpf}(s) = \frac{0.0025(20s + 1)}{(0.1s + 1)(0.05s + 1)}. \tag{5.19}$$

$C_{lpf}(q^{-1})$ is a discretization of the feedforward low-pass filter

$$C_{lpf}(s) = \frac{1}{10s + 1}. \tag{5.20}$$

The assistive torque is made proportional to the output of $C_{lpf}(q^{-1})$. k_{assist} is set to one, so that the EPB system has approximately two times the original open-loop DC gain of the bicycle, realizing 1:1 assistance at DC.

$$C_R(q^{-1}) = \frac{K_{rr}(1 - aq^{-1})(1 - p_o q^{-1})}{1 - 2\cos\omega_h q^{-1} + q^{-2}} \tag{5.21}$$

is the repetitive controller that is used to reject the sinusoidal disturbance contained in the human input with a frequency of ω_h rad/sample. In this expression, p_o is the pole for the discrete open loop bicycle transfer function, i.e. $P(q^{-1}) = b_o q^{-1}/(1 - p_o q^{-1})$. K_{rr} and a vary with changing ω_h and have the forms $K_{rr} = (2\cos\omega_h - 1)/b_o$ and $a = 0.75/(2\cos\omega_h - 1)$. The changes in the closed loop poles of the overall system with respect to the changing human input frequency ω_h from $\pi/40$ rad/sample to 0.2π rad/sample (the sampling time is 0.1 second) are shown in Fig. 5.5. The closed loop system has five poles. One is located at 0.9987, which coincide with the bicycle's open loop pole. The pair of complex conjugate poles inside the two boxes in Fig. 5.5 does not change very much with respect to changes in ω_h. The other pair shifts away from the real axis while ω_h increases. All the closed loop poles remain stable.

The controller implementation structure is shown in Fig. 5.6, where the feedback and feedforward controller inputs are combine together into one control input u, which is the input to the motor.

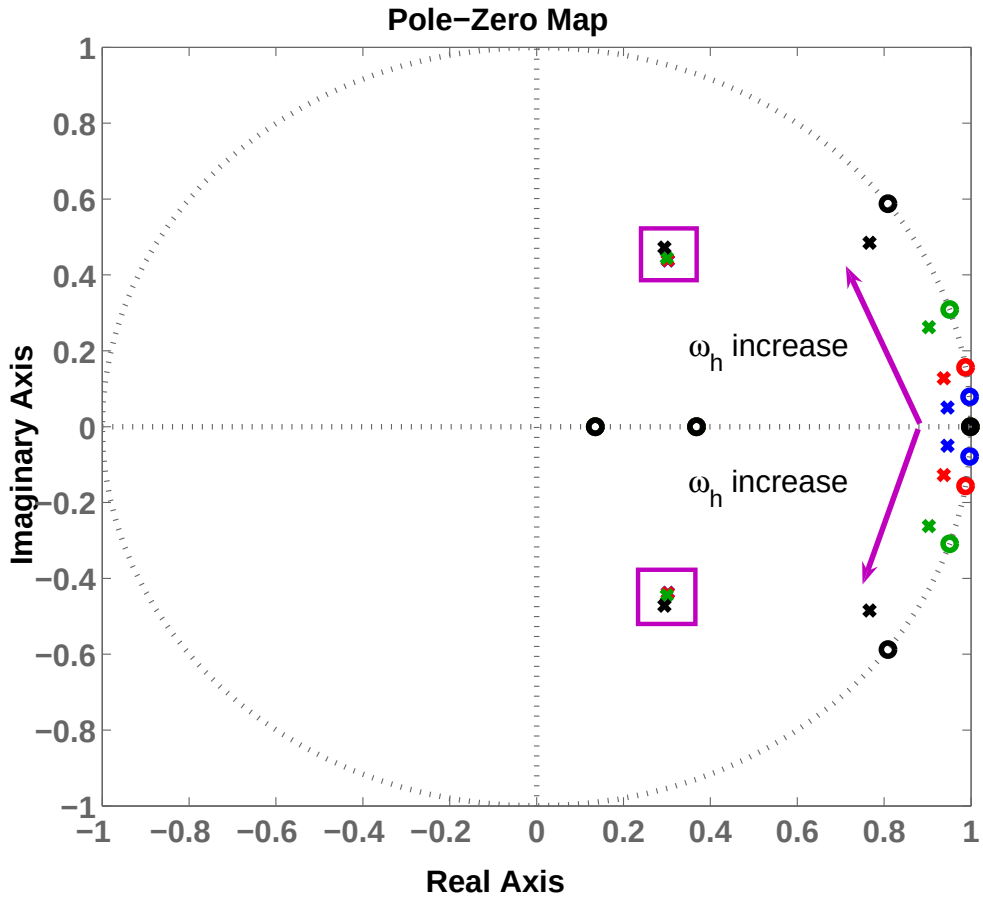

Figure 5.5: Closed loop poles with respect to changing ω_h. The cross marks represent closed loop poles and the circle marks represent closed loop zeros. The blue, red, green, and black colors correspond to the cases where $\omega_h = \pi/40$ rad/sample, $\omega_h = \pi/20$ rad/sample, $\omega_h = \pi/10$ rad/sample, and $\omega_h = \pi/5$ rad/sample, respectively. Note that the sampling time is $T_s = 0.1s$.

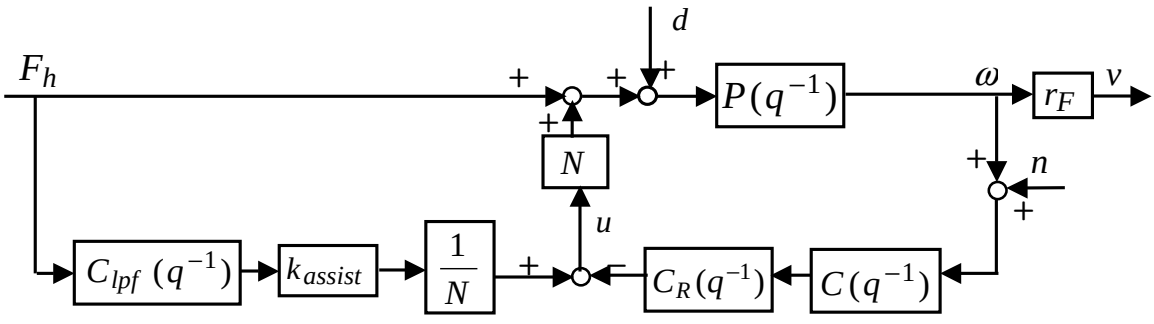

Figure 5.6: Controller implementation structure

5.4 Repetitive controller in pedal-angle domain

When a rider is biking, it is reasonable to assume that the torque generated by the rider is a function of the angle of the pedal's crank. Roughly speaking, we might suppose that the rider's torque is periodic with respect to the pedal angle. Therefore a repetitive controller is better to run in synchronization with the pedal angle. We call a controller synchronized with the pedal angle a controller *in the pedal-angle domain*.

5.4.1 Problems on controller design in pedal-angle domain

Let us consider a digital controller in the pedal-angle domain. Normal digital controllers run with a constant time interval Δt, while controllers in the pedal-angle domain run whenever the increment of the pedal angle reaches a constant angle interval $\Delta\theta$. Therefore, if we consider a digital controller in the pedal-angle domain, the angle interval $\Delta\theta$ is constant, rather than the time interval Δt. The time interval during which the pedal angle passes through $\Delta\theta$ is changing as the angular speed is changing. When the rotational speed is faster (or slower) and the time interval becomes shorter (or longer).

This observation implies that the system dynamics discretized in the pedal-angle domain varies with respect to the pedal-angle even if the systems are time-invariant in the time domain. Thus controllers in the pedal-angle domain should be designed for time-varying systems. There are several ways to deal with time-varying systems and this paper selected a robust control approach.

5.4.2 Uncertainty estimation

It is important for robust controller designs to estimate the uncertainty bound tightly to avoid overly conservative controllers. From (3.15), the bicycle dynamics can be represented by a stable first-order system.

$$\dot{x} = -\alpha x + \beta u \tag{5.22}$$

where x is a scalar state variable, u is a scalar input, and α and β are system parameters and positive. We use Δt as the nominal time interval and δ as the deviation of

the time interval from Δt. Human biking speed is limited when riding uphill. It is thus reasonable to assume that there is a minimum time interval associated with the given $\Delta\theta$. Now, we set the nominal time interval Δt as the minimum time interval under the assumption, and then δ is always greater than or equal to 0. Note that the overall time interval is represented by $\Delta t + \delta$.

The input value of u during each time interval is considered as a constant, and the discretized system of (5.22) with the time interval $\Delta t + \delta$ is given by

$$x_{k+1} = e^{-\alpha(\Delta t+\delta)} x_k + \frac{\beta}{\alpha}\left(1 - e^{-\alpha(\Delta t+\delta)}\right) u_k. \tag{5.23}$$

The transfer function of (5.23), $P(q^{-1}, \delta)$, and the nominal transfer function $P_n(q^{-1})$ with $\delta = 0$ are, respectively, defined by

$$P(q,\delta) = \frac{\beta/\alpha(1 - e^{-\alpha(\Delta T+\delta)})}{(q - e^{-\alpha(\Delta t+\delta)})},\ P(q) = \frac{\beta/\alpha(1 - e^{-\alpha\Delta T})}{(q - e^{-\alpha\Delta t})}. \tag{5.24}$$

The difference between $P(e^{j\omega}, \delta)$ and $P_n(e^{j\omega})$ in the frequency domain $\omega \in [0, 2\pi)$ is defined as

$$\begin{aligned} |P_e(e^{j\omega})| &= \left|\frac{P_n(e^{j\omega}) - P(e^{j\omega},\delta)}{P_n(e^{j\omega})}\right| = |\bar{r}(e^{j\omega})|\bar{\gamma}(\delta) \\ \bar{r}(e^{j\omega},\delta) &= \left|\frac{e^{j\omega} - 1}{e^{j\omega} - e^{-\alpha(\Delta t+\delta)}}\right|,\ \bar{\gamma}(\delta) = \frac{e^{-\alpha\Delta t}(1 - e^{-\alpha\delta})}{1 - e^{-\alpha\Delta t}}. \end{aligned} \tag{5.25}$$

Note that $|P_e(e^{j\omega})| \to 0$ as $\delta \to 0$, and

$$\lim_{\delta\to\infty} |P_e(e^{j\omega})| = \left|\frac{e^{j\omega} - 1}{e^{j\omega}}\right| \frac{e^{-\alpha\Delta t}}{1 - e^{-\alpha\Delta t}} \tag{5.26}$$

provides the multiplicative uncertainty bound. The part of $|(e^{j\omega} - 1)/e^{j\omega}|$ is not very large in magnitude. However, the total uncertainty bound of (5.26) becomes very large if Δt is small because $e^{-\alpha\Delta t}$ is close to 1. For example, $e^{-\alpha\Delta t}/(1 - e^{-\alpha\Delta t})$ becomes about 10000 with $\alpha = 0.01$ and $\Delta t = 0.01$. If the overall uncertainty in (5.25) is taken into account, the resultant controller might be too conservative. Therefore we need to divide the uncertainty bound of (5.25) into two parts: $\bar{r}(e^{j\omega}, \delta)$ and $\bar{\gamma}(\delta)$, and treat each bound separately.

Fortunately, each time interval $\Delta t + \delta$ can be estimated from the angular velocity ω_k of the crank shaft as $\Delta t + \delta = \Delta\theta/\omega_k$. Therefore δ is a function of ω_k as $\delta(\omega_k)$. This implies that we can also estimate $\bar{\gamma}(\delta)$ from ω_k. Hence a gain-scheduling technique

is utilized to compensate this large gain-fluctuation as shown in the block diagram, Fig. 5.7. The gain scheduled by ω_k, $\gamma(\omega_k)$, is given by

$$\gamma(\omega_k) = \frac{1 - e^{-\alpha\Delta t}}{1 - e^{-\alpha(\Delta t + \delta(\omega_k))}}. \tag{5.27}$$

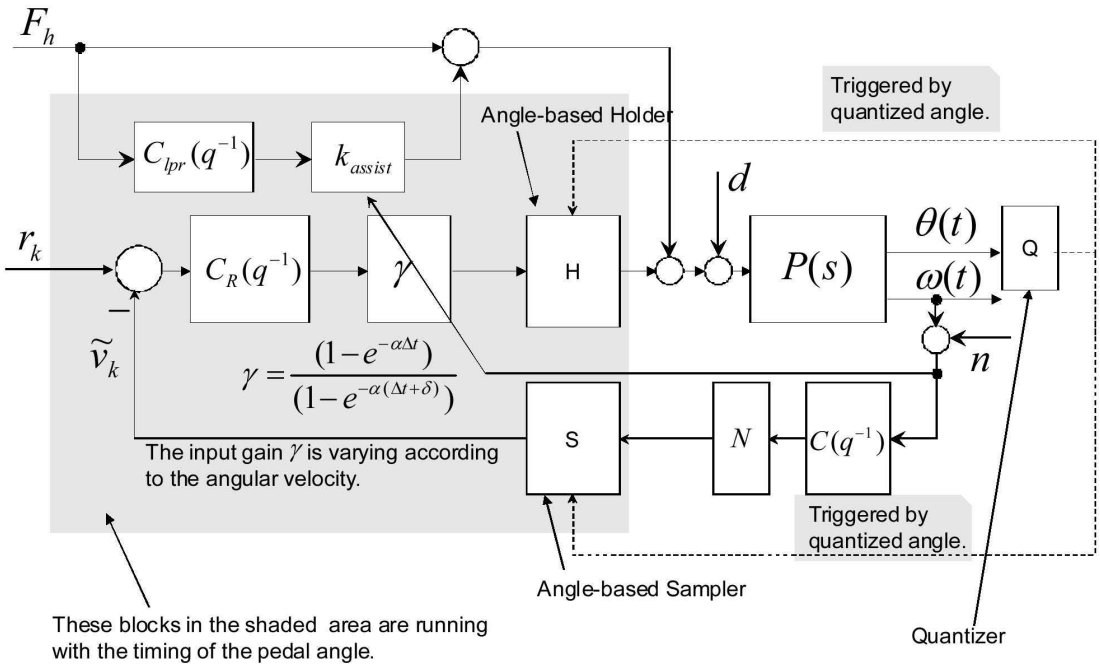

Figure 5.7: Block diagram of the robust repetitive controller in pedal-angle domain

The uncertainty part associated with the dynamics in (5.25) can be dealt with by the robust repetitive controller as summarized in one of the previous sections. Note that

$$\lim_{\Delta t+\delta\to 0} \max_{\omega\in[0,\pi]} \bar{r}(e^{j\omega}, \delta) = 1 \tag{5.28}$$

as shown in Fig. 5.8. Therefore we chose

$$r(q) = \frac{1.6(q - 0.5)}{q - 0.2} \tag{5.29}$$

to cover all the uncertainty variations associated with the sampling fluctuation.

The q-filter should be designed to satisfy (5.16). We fixed the order of the q-filter with $h(q^{-1}) = h_0 + h_1 q^{-1} + h_2 q^{-2}$, and searched the parameters $h_i,\ i = 0, \ldots, 2$ to

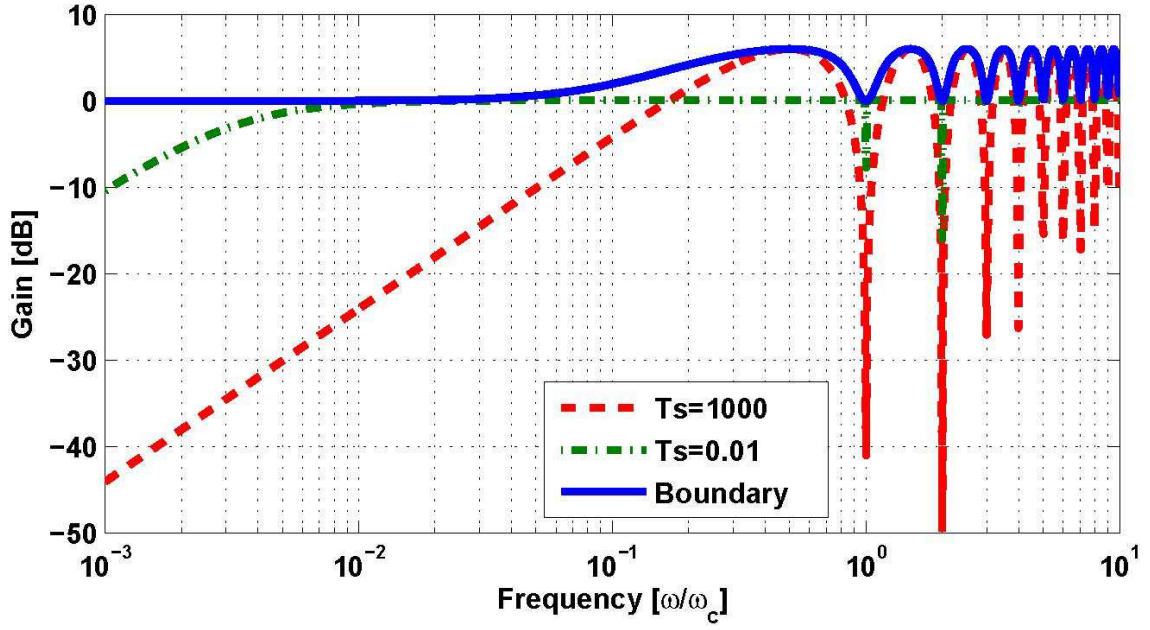

Figure 5.8: Frequency response of the uncertainty associated with the sampling interval fluctuation, $\bar{r}(e^{j\omega}, \delta)$. The blue line shows $|\bar{r}(e^{j\omega}, \delta)|$ with $\Delta t + \delta = 1000$, and the green line with $\Delta t + \delta = 0.01$. The red line shows the uncertainty bound, $|r(e^{j\omega})|$.

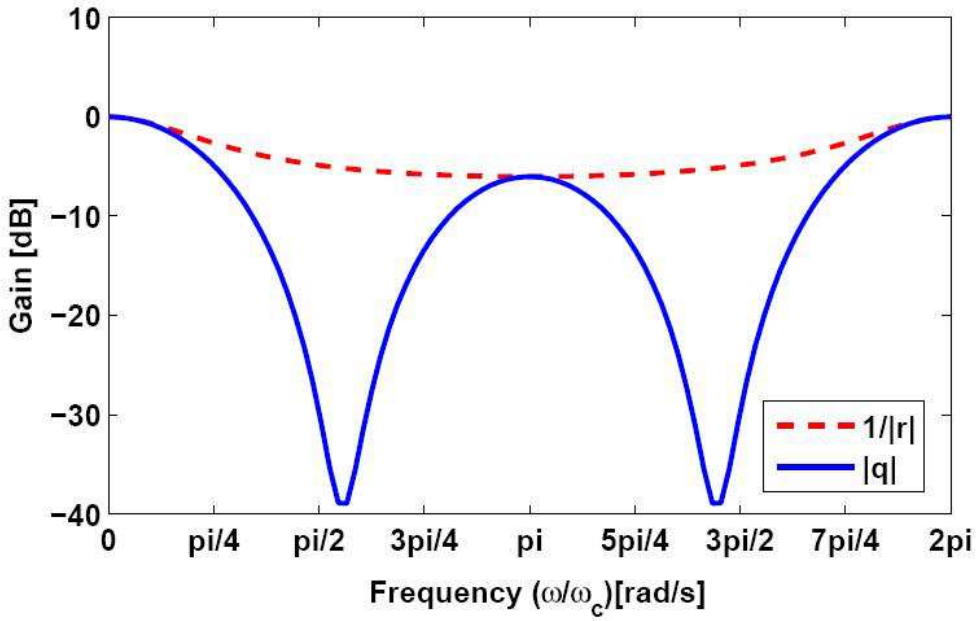

Figure 5.9: The uncertainty bound, $1/|r(e^{j\omega})|$ and the frequency response of the Q-filter.

minimize the square norm of $\sum_{i=0}^{n}(-20\log_{10}|r(e^{j\omega})| - 20\log_{10}|\mathbf{q}(e^{j\omega}, e^{-j\omega})|)^2$ under the constraint (5.16). This nonlinear optimization was performed by MATLAB, and the result is shown in Fig. 5.9. Finally we got a q-filter satisfying the condition,

$$\mathbf{q}(q, q^{-1}) = \frac{q^2 + 0.6968q^1 + 2.181 + 0.6968q^{-1} + q^{-2}}{5.574}. \tag{5.30}$$

Note that this q-filter may be conservative in some regions. If the order of the q-filter increases, a less conservative filter might be obtained.

5.5 Simulations

5.5.1 Human input generation

To imitate the human's pedaling behavior in simulation, we employ a human torque generator designed based on the following observations:

1. The human pedaling angular velocity is related to the bicycle angular velocity.
2. The human input power is limited. As the frequency increases, the human input torque decreases.
3. The human's input power level is dependent on the road condition.

According to [37], human can maintain prolonged pedaling power of about 0.05 horsepower (37.3 watts) with 20-60 rpm pedaling rate. We assume that the human's power level is 37.3 watts for flat surface and 37.3×2 watts for uphill riding. For the simulations conducted in this paper, we assume that the cyclist rides on a flat surface for the first 10 seconds and then goes up a hill of 3 degrees. Fig. 5.10 shows the simulated human input for traditional proportional power-assist controller. Notice that the generated human torque profile has a half-sinusoidal pattern for each pedal stroke. Fig. 5.11 shows the corresponding motor input.

5.5.2 Time domain repetitive controller

The designed time domain repetitive controller is simulated with the half-sinusoidal human input generator. The simulation results for the bicycle velocity are shown

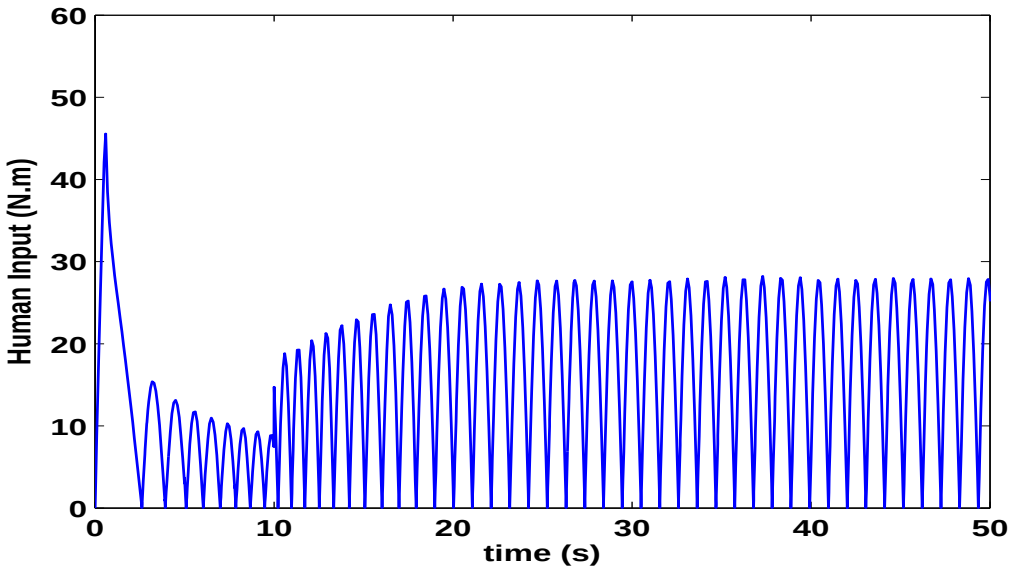

Figure 5.10: Human input for traditional proportional control

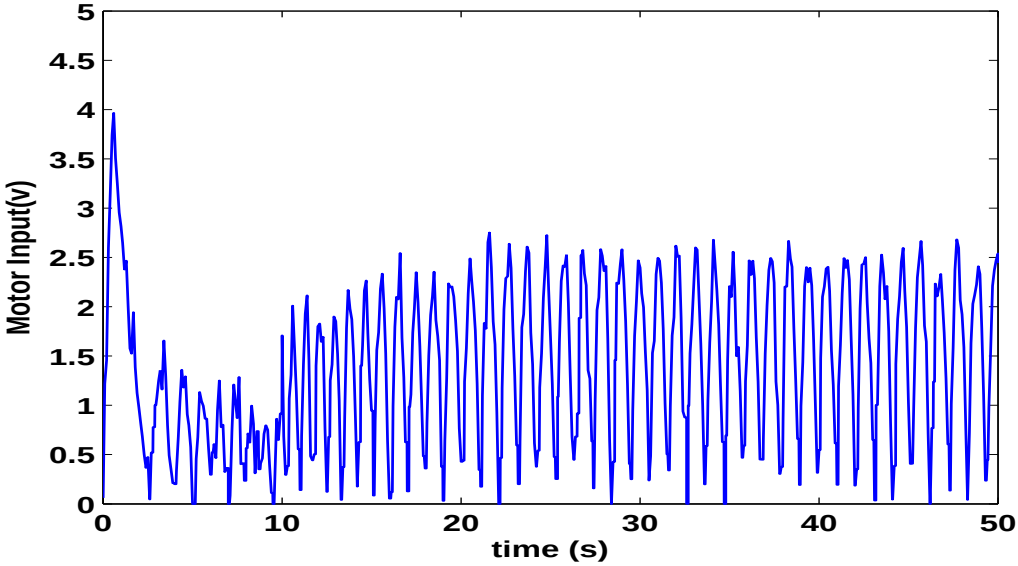

Figure 5.11: Motor input for traditional proportional control

in Fig. 5.12. Since the simulated human torque input is not a single sinusoid, the oscillation in the bicycle velocity can not be completely removed. Since we use the pedal-crank angular velocity measurement as the human pedaling frequency in the repetitive controller, measurement noise also causes inaccuracy. The second plot in Fig. 5.12 shows the magnified velocity profile for the time duration from 50 second to 100 second. We can see that the oscillation in the velocity profile has been greatly reduced with the proposed repetitive controller. The corresponding human torque input and motor input are shown in Figs.5.13 and 5.14. Note that for all the simulation results presented in this paper, a limit of [0v, 5v] has been imposed on the motor input to avoid motor input saturation. The remaining oscillation in the velocity profile is minimal and can barely be noticed by human. The simulation results show that the time domain repetitive controller have good performance in terms of rejecting the oscillation in the velocity profile.

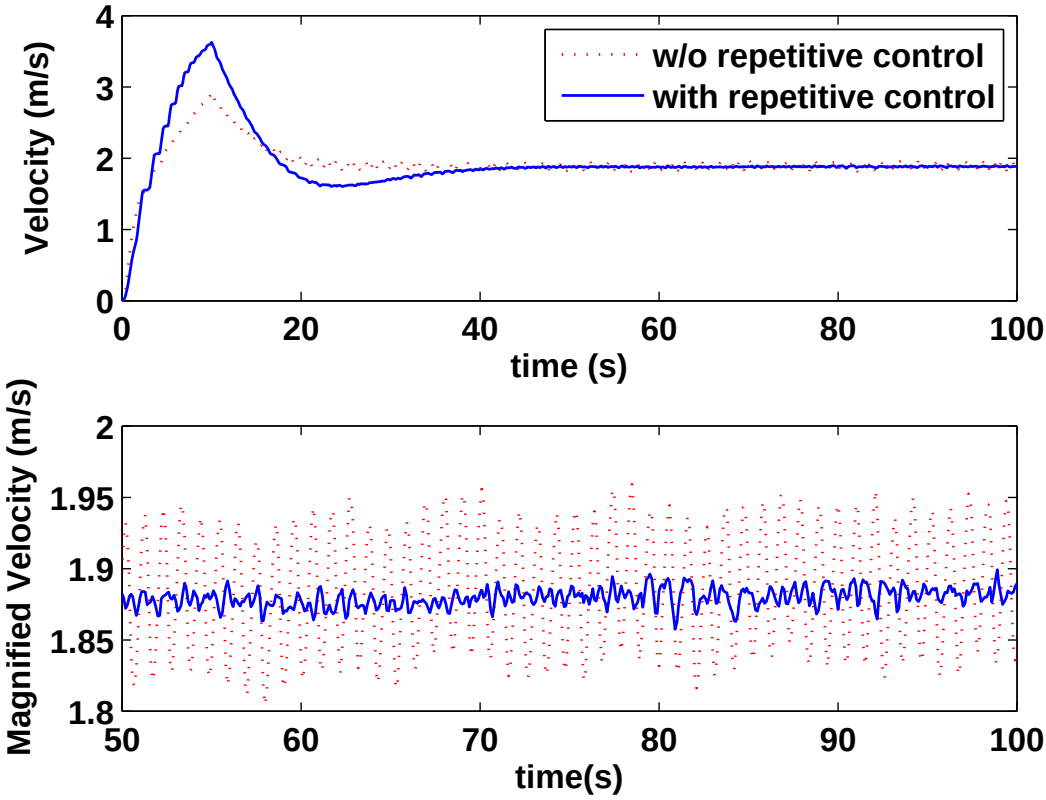

Figure 5.12: Velocity simulation results for the time domain repetitive controller

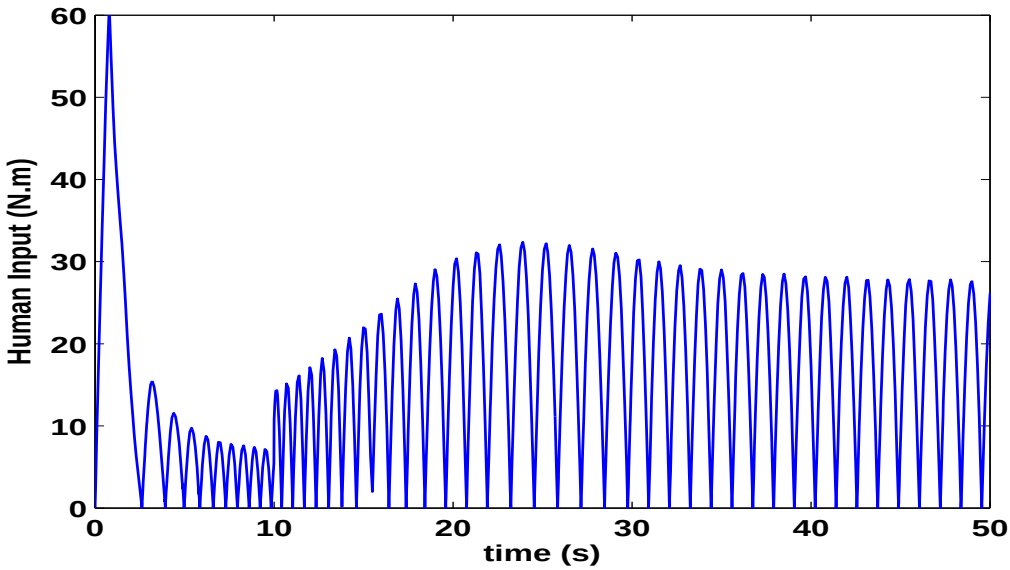

Figure 5.13: Human input for the time domain repetitive controller

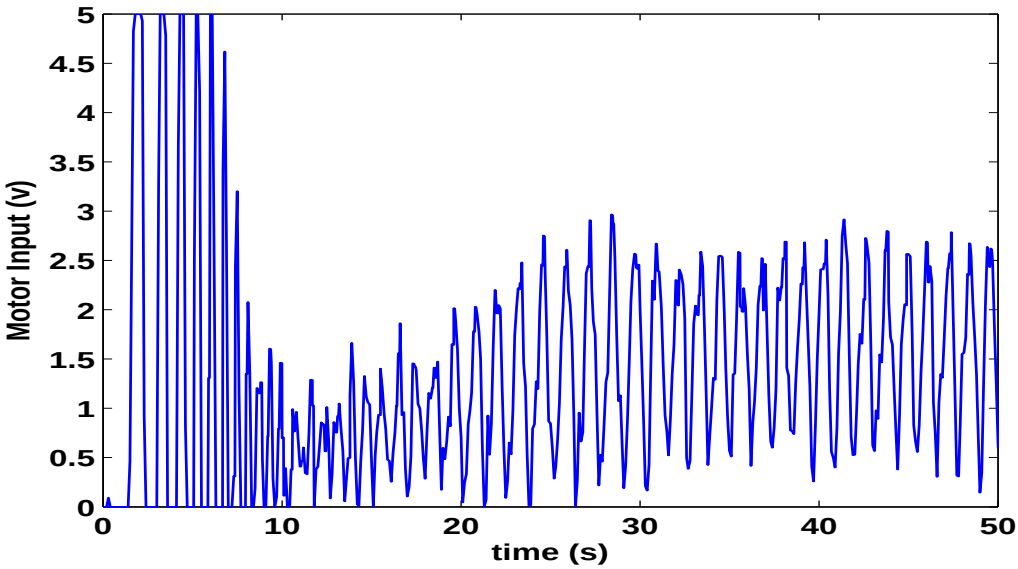

Figure 5.14: Motor input for the time domain repetitive controller

5.5.3 Pedal-angle domain repetitive controller

The effectiveness of the pedal-angle domain robust repetitive controller is also verified through simulation with the half-sinusoidal human input generator. The controller realization structure is very similar to that used in the time domain method shown in Fig. 5.6, except that in the pedal-angle domain case, we use a high-pass filter instead of a band-pass filter to reject the DC gain of the velocity profile and provide the information to be compensated by the repetitive controller. The high-pass filter has the form

$$C_{bpf} = \left(\frac{s}{s+0.35}\right)^4. \tag{5.31}$$

The simulation results for the pedal-angle domain robust repetitive controller are shown in Fig. 5.15 and Fig. 5.17. The second plot in Fig. 5.15 is a magnified version of bicycle angular velocity between 50 second and 100 second. We can see that the pedal-angle domain repetitive control also greatly reduced the oscillation in the bicycle's velocity compared with the case without repetitive control. However, we can also see a slow transient response in the robust-repetitive controller. This unexpected slow transient might be caused by the high-pass filter to eliminate the DC-gain of the velocity profile. The robust repetitive controller is sensitive to the phase-lag of the signals to be compensated, therefore the high-pass filter should have zero phase shift over the range in which the signal is compensated by the controller. This means that we cannot shift the poles of the high-pass filter into the high frequency-domain. Thus, the slow transient is inevitable under this configuration. The improvement of the slow transient will be a future research topic.

5.6 Experimental results

Experiments on the EPB were done to verify the effectiveness of the robust repetitive control based power-assist algorithm. The experiments were carried out on a slope with an inclination of about 9 degrees. For comparison purposes, we considered the case with DC amplification power-assistance based on low pass filtering, as well as the case with DC amplification and robust repetitive control compensation. Note that the structure shown in Fig. 5.7 calculates the amount of assistive motor torque needed to flatten the combined torque profile. In practice, this torque amount may exceed

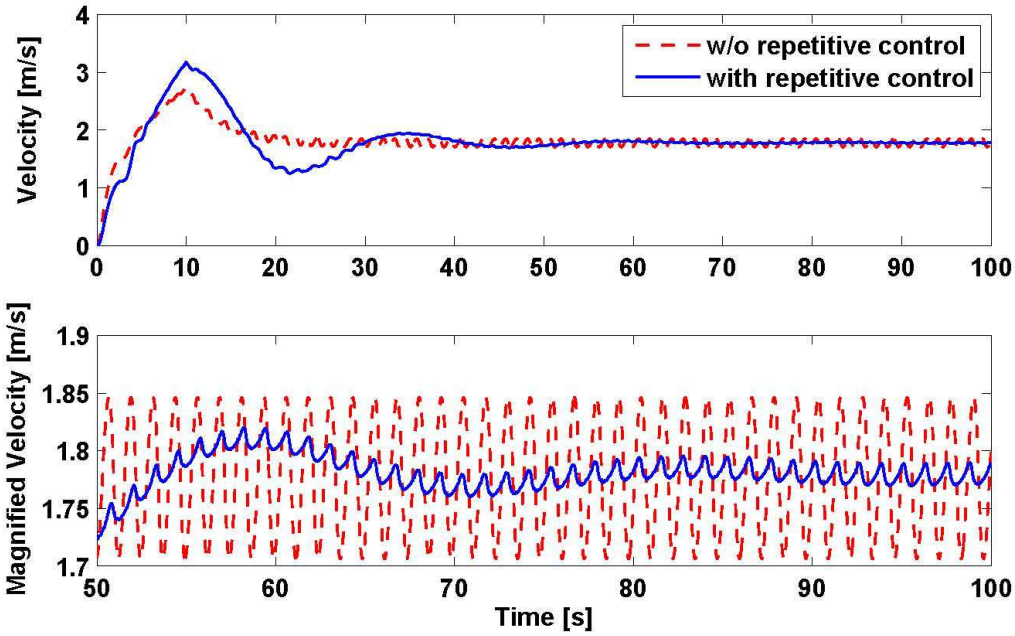

Figure 5.15: Simulation results for the pedal-angle domain repetitive controller

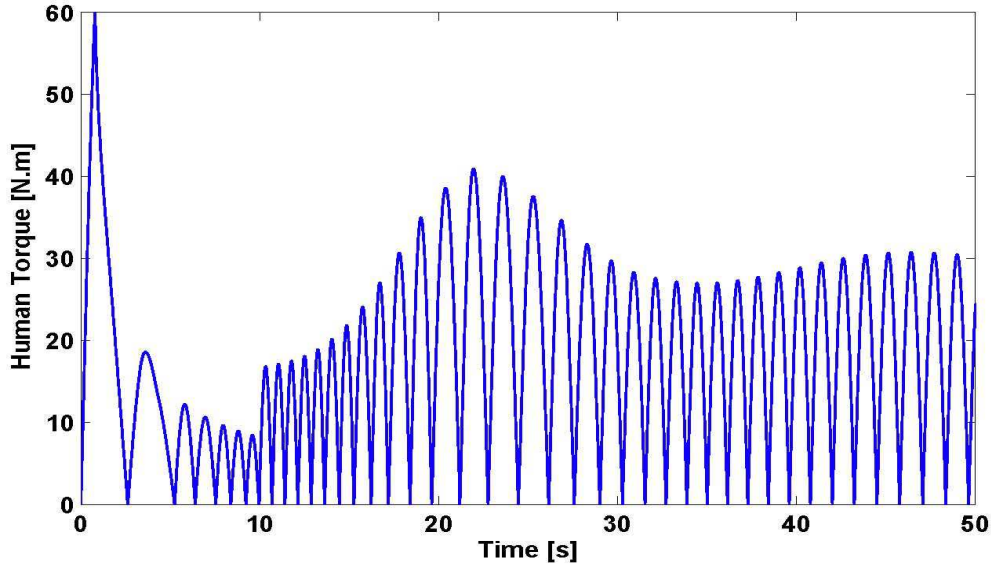

Figure 5.16: Human input for the pedal-angle domain repetitive controller

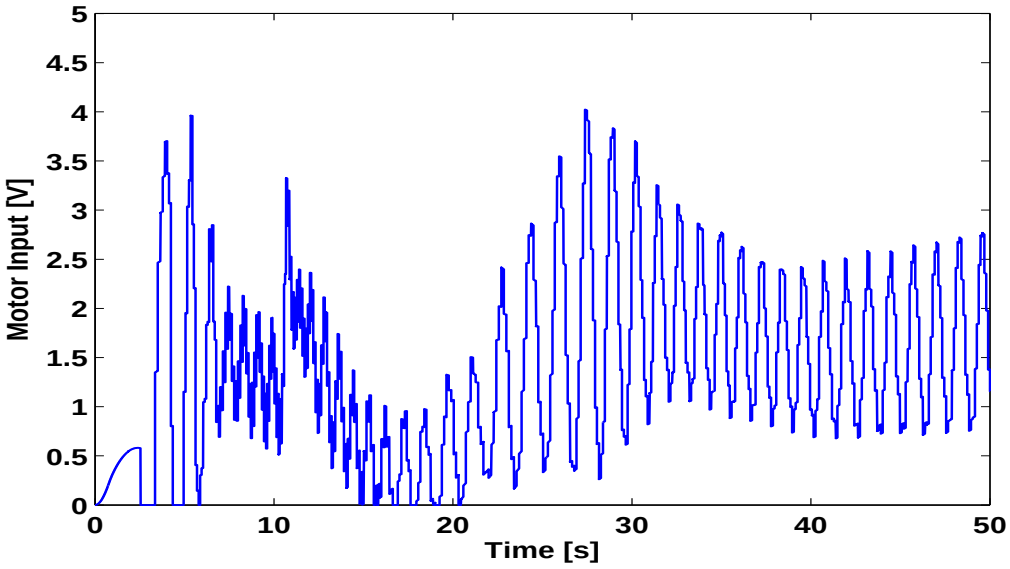

Figure 5.17: Motor input for the pedal-angle domain repetitive controller

the upper limit of the motor's output torque, i.e., the motor input recommended by the robust repetitive controller shown in Fig. 5.7 may exceed the motor input range of $[0V, 5V]$. In the experiments, we apply only 20% of the calculated motor input to avoid motor input saturation. As we can expect, this reduction in the actual applied torque will result in a corresponding reduction in the controller's capability of torque variation compensation. Figure 5.18 shows the comparison of EPB's front wheel angular velocity profiles for the cases with and without robust repeptitive control. The red line shows the case with only the box-car filter DC torque amplification, while the blue line shows the case with both DC torque amplification and robust repetitive control compensation. Note that the horizontal axis in the figure is the pedal angle degrees. The backward red line starting at around 200 degrees means that the cyclist took a backward stroke in the pedal. As we can see from the figure, the amplitude of the variation in the velocity profile is reduced with the repetitive control compensation. Figure 5.19 shows the magnified comparison in the steady state velocity profiles for the two cases in Fig. 5.18. To quantify the effect of the robust repetitive compensation, we calculated the mean and standard deviation of the steady state velocity profiles. Table 5.1 shows these values. We can see that the standard deviation reduced from 0.466 to 0.385, which is a 20% reduction. This number is consistent with the 20% control effort that we supplied through the motor.

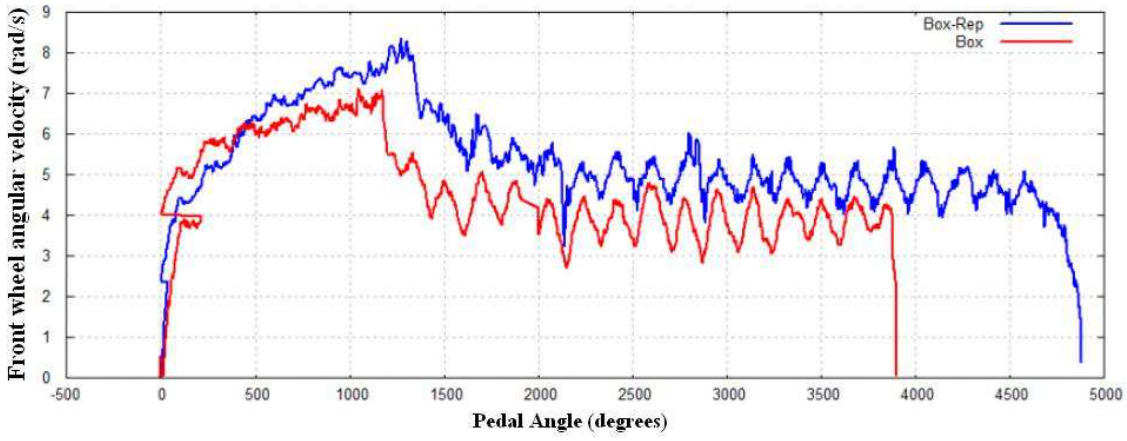

Figure 5.18: Experimental results for the EPB's front wheel angular velocity profiles with and without robust repetitive control

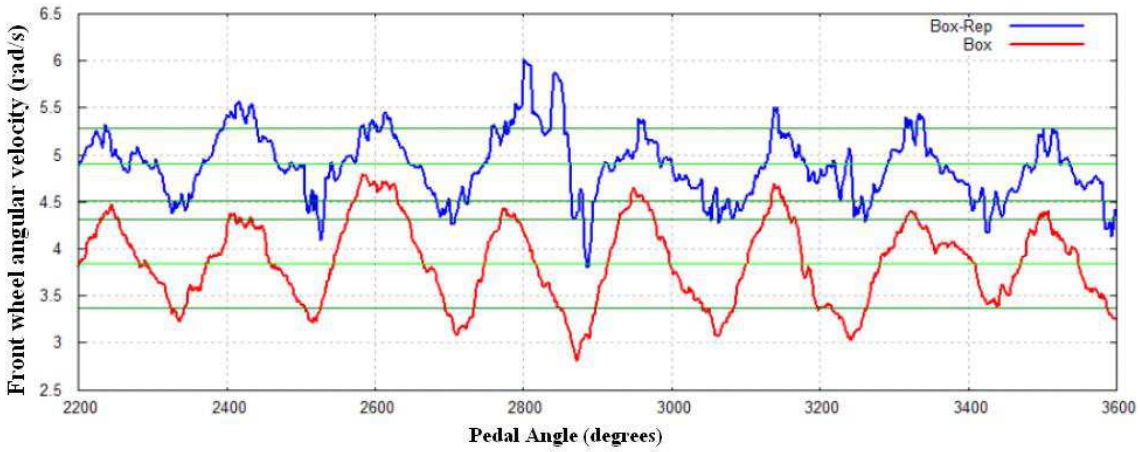

Figure 5.19: Magnified steady state front wheel angular velocity profile for the EPB with and without robust repetitive control

Table 5.1: Mean and standard deviation of steady state EPB velocity profiles

	Mean	Standard deviation
Without repetitive control	3.84	0.466
With repetitive control	4.90	0.385

Figure 5.20 shows the human input thrust forces for the experimental cases with and without repetitive control compensation. Figure 5.21 shows the corresponding motor inputs for the two cases. We can see from the figures that the human input thrust forces are comparable in magnitude in the two cases. However, the motor input for the case with no repetitive compensation but only DC compensation appears to be much flatter and smoother compared to the case with repetitive compensation. As we can expect, the repetitive controller generates an oscillatory input of the same frequency as that of the fluctuant component $F_{fluct}(t)$ in the human input. Figure 5.22 further verified that the generated periodic fluctuation in the motor input does have an inverse phase compared to the human thrust force input. Note that we have normalized the human's input thrust, i.e., divided the thrust force by 140, to make it comparable to the motor input. Figure 5.23 shows the human thrust force and the total combined thrust force (with the human force and motor force added together) for the cases with and without repetitive compensation. The blue lines in the two plots are the human's input thrust force. The red lines represent the combined total force from the human and the motor. We can see that with the repetitive control compensation, the minimum combined force has been effectively increased. It means that for the positions where the human can not provide input force/torque, the motor's torque can fill in and significantly increase the minimum combined torque.

The experimental results shown above verified that the robust repetitive power-assist design in the pedal-angle domain can effectively reduce the fluctuation in the EPB's velocity profile, which is consistent with the simulation results shown in Section 5.5. Therefore, the repetitive control based power-assist algorithm can enhance rider's uphill riding comfort with its inverse phase torque compensation.

Efforts have been made to implement the time-domain adaptive repetitive control based power-assist controller design on the experimental EPB system. However, we did not succeed after several trials. The adaptitive repetitive controller requires

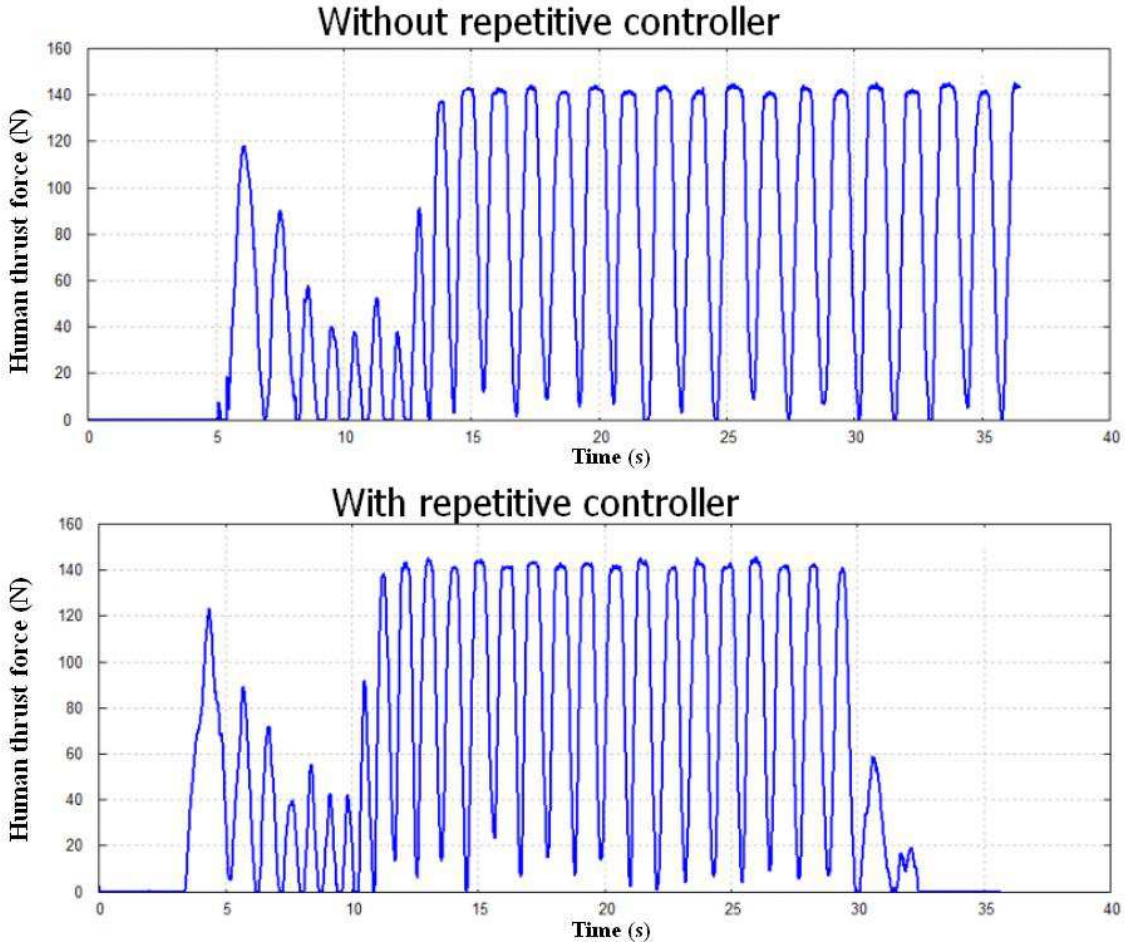

Figure 5.20: Human input thrust force for the EPB with and without robust repetitive control

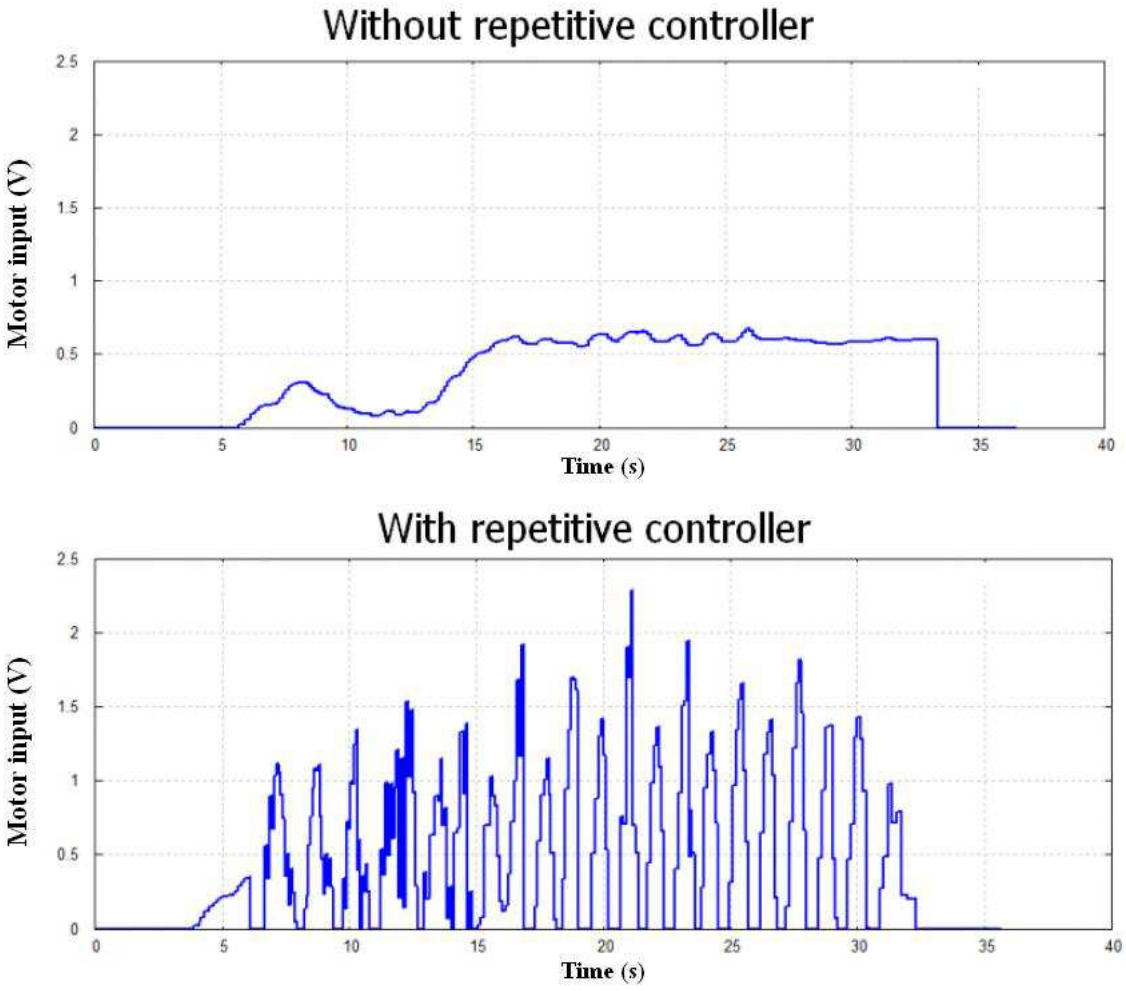

Figure 5.21: Motor input for the EPB with and without robust repetitive control

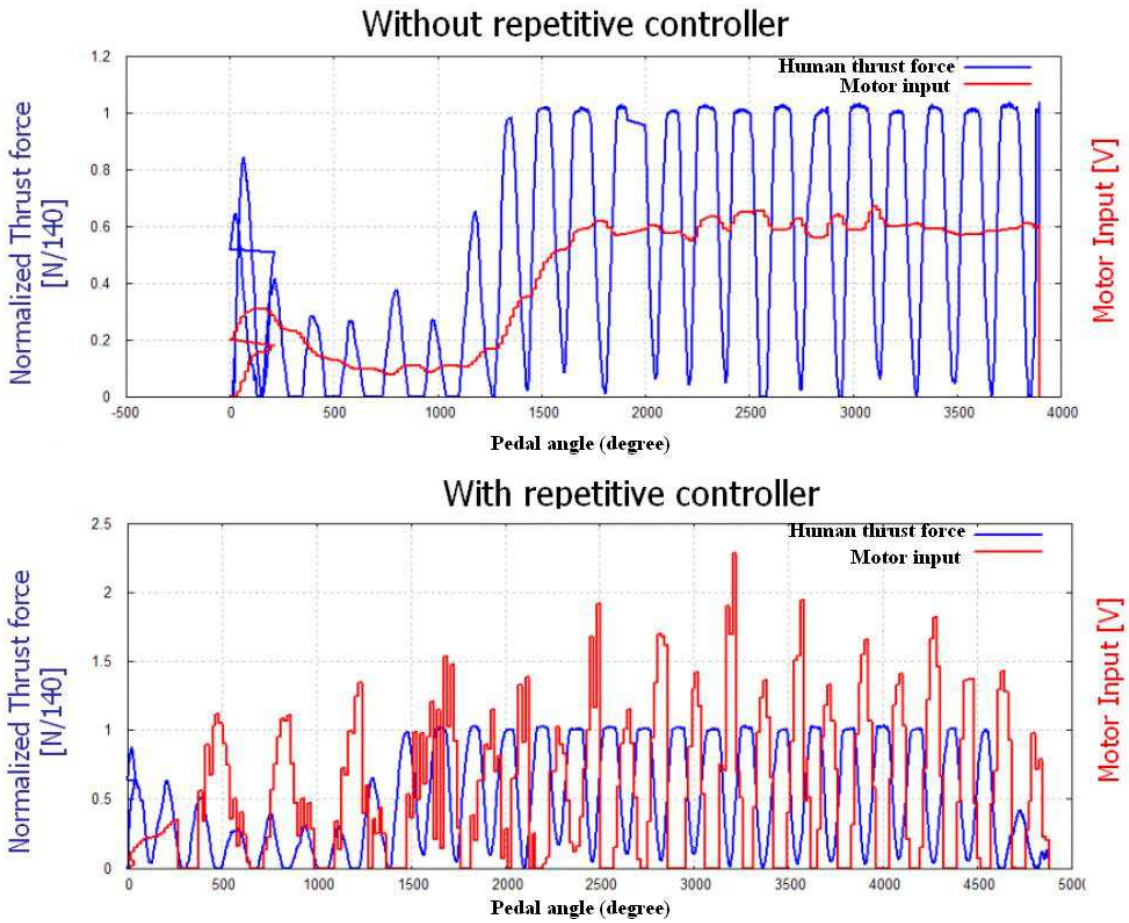

Figure 5.22: Normalized human thrust force and motor input

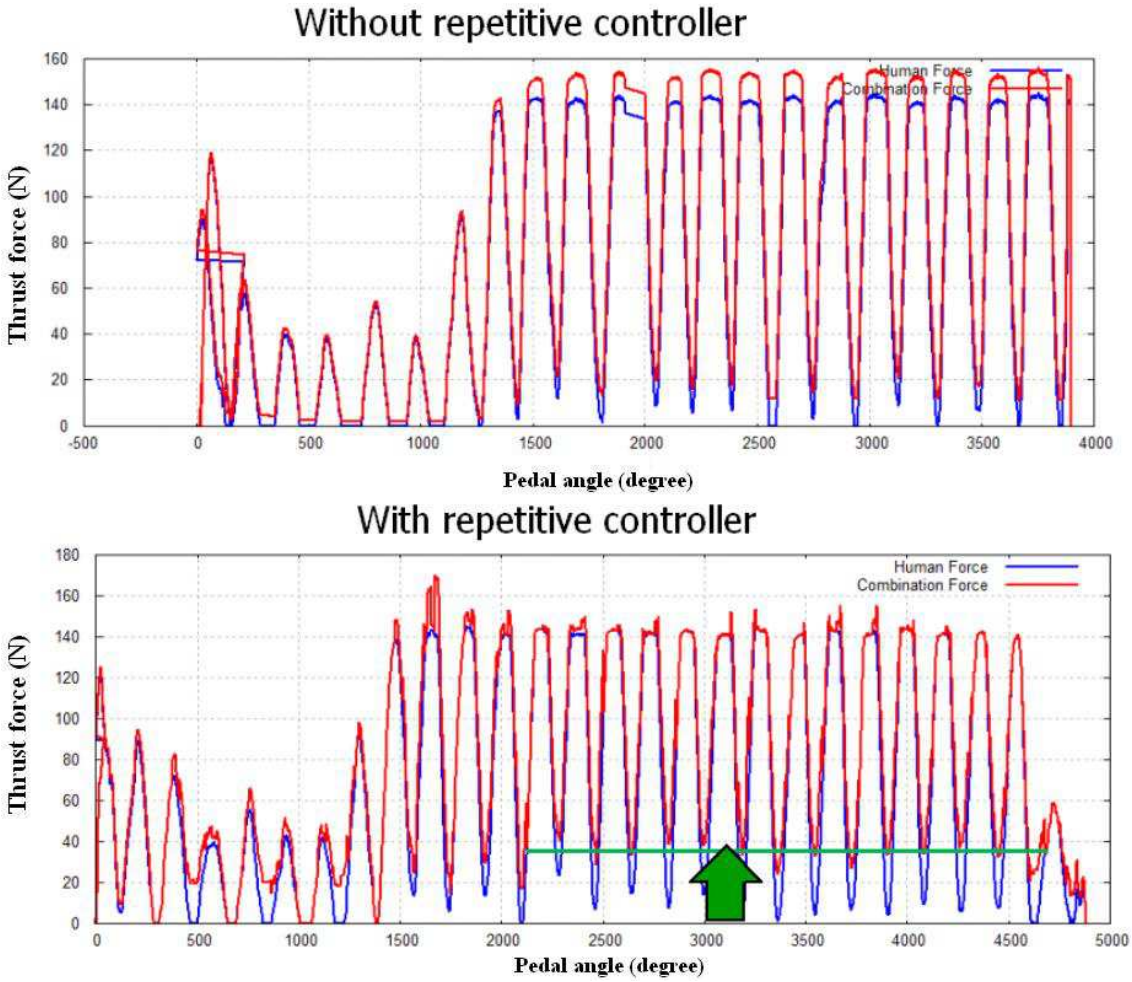

Figure 5.23: Human thrust force and combined thrust force

real-time estimation of the human input frequency ω_h. In our experimental trials, the human input frequency estimate was acquired through differentiating the pedal angle measurement, which comes from an encoder signal. Pure diffentiation invokes high numerical sensitivity, which is not good for experiments. Although filtering techniques can be used to remove the differentiation noise, the response time of the filter makes the frequency estimate not "real-time" anymore. Although the simulation results shown in Subsection 5.5.2 verified that the time-domain adaptitive repetitive controller is effective in removing the oscillation in the velocity and accelleration profiles under half-sinusoidal human input, the real human torque input is hardly sinusoidal and experimental results may not be so satifying as shown by simulation. The pedal-angle domain robust repetitive control based design may be more suitable in this situation, considering implementation feasibility and real human input pattern.

Chapter 6

Conclusions

This dissertation investigates the design and implementation of intelligent power-assist algorithms for electric power-assist bicycles (EPBs). EPBs have extended mobility compared with traditional bicycles because of the extra power (torque) supply from the electric motor. The potential possibility for EPBs to take the place of fuel powered vehicles for mid-range transportations makes them an interesting research subject. How to make EPB rides more comfortable is one of the major concerns in the EPB industry. This dissertation focuses on the uphill riding condition and provides two types of intelligent power-assist algorithms. Intelligent power-assist algorithms are different from traditional proportional power-assist algorithms in that they are more flexible and considers the interaction between the bicycle, the human and the environment.

The first type of intelligent power-assist algorithm is based on robust disturbance observer (DOB) technique. The gravity drag force along with other friction forces constitutes the environmental disturbance input in the EPB system. Most of the times, the proportional power-assistance scheme used in traditional EPBs can not provide sufficient assistive torque to the cyclist when he/she is riding up a steep slope. The disturbance observer based scheme can add flexibility in the power-assist system by estimating and compensating for the environmental disturbance that is present in the EPB system. Robust stability is crucial in this case since it is related to the cyclist safety. By satisfying the robust stability criterion when designing the Q-filter for the DOB, we can guarantee the robust stability of the overall EPB power-assist system in the presence of multiple parametric uncertainties. Hardware limitations

are also a big concern in the EPB system. The major issue in this experimental setup is the motor input saturation. An anti-windup modification was made to the robust DOB design to accommodate this hardware limitation. Experimental results for the cases with and without motor saturation were shown to verify the effectiveness of the power-assist designs.

The second type of intelligent power-assist algorithm is based on repetitive control techniques. Although the robust DOB scheme can provide flexibility to the EPB power-assist system, it does not consider the nonuniform velocity and acceleration profiles that can cause severe discomfort during uphill riding. Due to the mechanical design of the crankset, the human's pedaling torque is periodic and has two local maximum/minimum torque positions in each pedal cycle. The variations in the human's pedaling torque make the human input torque profile nonuniform and the fluctuation becomes more prominent during uphill riding. To address this issue, we considered two different repetitive control based power-assist algorithms. Repetitive control technique is widely used in periodic disturbance rejection and/or periodic reference input regulation. Time domain repetitive control design can be applied when we model the human input as a combination of sinusoids with different frequencies. Since the frequency of the human input will be time-varying, the frequencies in the model will also change over time. An adaptive handling manner is developed in this dissertation. Pedal-angle domain repetitive control design is applicable when we model the human input as a periodic signal with a fixed period of N and a time-varying sampling period T_s. This configuration calls for pedal-angle domain sampling, that is, we take a sample every $2\pi/N$ rad. This way, the system becomes time-varying in the time domain. A robust repetitive design is chosen to compensate for the nonuniform human input in this case. The two repetitive controllers are simulated to verify their effectiveness. Experimental results further confirms the plausibility of the robust repetitive design in the pedal-angle domain.

A great amount of effort was also used in reverse engineering and building the experimental EPB setup. System identification was also done for the EPB's front wheel motor to obtain the values of specific motor parameters. Bicycle's roll and steer angle dynamics were also studied to understand some of the key observations in EPB control. EPB's dynamic model was provided for intelligent power-assist algorithms design purposes.

Bibliography

[1] M. Tomizuka. Dealing with periodic disturbances in controls of mechanical systems. *Annual Reviews in Control*, 32(2):193–199, December 2008.

[2] J.P. Meijaard, J.M. Papadopoulos, A. Ruina, and A.L. Schwab. Linearized dynamics equations for the balance and steer of a bicycle: a benchmark and review. In *Proceedings of the Royal Society A*, volume 463, pages 1955–1982, 2007.

[3] A.L. Schwab, J.P.Meijaard, and J.M. Papadopoulos. Benchmark results on the linearized equations of motion of an uncontrolled bicycle. In *Proceedings of the Second Asian Conference on Multibody Dynamics*, August 2004.

[4] Motorized bicycle. http://en.wikipedia.org/wiki/Motorized_bicycle.

[5] Q. Tu. Overview of the development of electric bicycle technology in japan. *Bicycles in China*, January 2004.

[6] Hybrid vehicle. http://en.wikipedia.org/wiki/Hybrid_vehicle.

[7] Optibike 850xli. http://optibike.com/optibike-850XLi.html.

[8] Golden motor mt-2009. http://www.goldenmotor.com/.

[9] D. Limebeer and R. Sharp. Bicycles, motorcycles, and models. *IEEE Control Systems Magazine*, 26(5):34–61, October 2006.

[10] Q. Zheng and M. Tomizuka. A disturbance observer approach to detecting and rejecting narrow-band disturbances in hard disk drives. In *Proceedings of the 10th International Workshop on Advanced Motion Control*, pages 254–259, Trento, Italy, March 2008.

[11] M.T. White, M. Tomizuka, and C. Smith. Improved track following in magnetic disk drives using a disturbance observer. *IEEE/ASME Transactions on Mechatronics*, 5(1):3–11, March 2000.

[12] H. Yabushita, Y. Hirata, K. Kosuge, and Z. Wang. Environment-adaptive control algorithm of power assisted cycle. In *Proceedings of the 29th Annual Conference of the IEEE Industrial Electronics Society*, volume 2, pages 1962–1968, Roanoke, Virginia, USA, November 2003.

[13] S. Komada, N. Machii, and T. Hori. Control of redundant manipulators considering order of disturbance observer. *IEEE Transactions on Industrial Electronics*, 47(2):413–420, 2000.

[14] J.R. Ryoo, T.Y. Doh, and M.J. Chung. Robust disturbance observer for the track-following control system of an optical disk drive. *Control Engineering Practice*, 12(5):577–585, 2004.

[15] G. Guo, D. Wu, and T.C. Chong. Modified dual-stage controller for dealing with secondary-stage actuator saturation. *IEEE Transaction on Magnetics*, 39(6):3587–3592, November 2003.

[16] K. Chew and M. Tomizuka. Digital control of repetitive errors in disk drive systems. *IEEE Control Systems Magazine*, 10(1):16–20, January 1990.

[17] M. Steinbuch. Repetitive control for systems with uncertain period-time. *Automatica*, 38(12):2103–2109, December 2002.

[18] T. Tsao and M. Tomizuka. Robust adaptive and repetitive digital tracking control and application to a hydraulic servo for noncircular machining. *Journal of Dynamic Systems, Measurement, and Control*, 116(1):24–32, March 1994.

[19] M.G.J.M. (Martijn) Maassen. Intelligent power assisted bicycles – design of a motor driver for the experimental setup. Traineeship report, Technische Universiteit Eindhoven., May 2008.

[20] Magnetostriction. http://en.wikipedia.org/wiki/Magnetostriction.

[21] Bicycle and wheel stability demo. http://ruina.tam.cornell.edu/misc/archive/O3_BikeStability.mov.

[22] K. Ohnishi. A new servo method in mechatronics. *Transaction of Japanese Society of Electrical Engineering*, 107-D:83–86, 1987.

[23] T. Murakami and K. Ohnishi. Advanced motion control in mechatronics - a tutorial. In *Proceedings of the IEEE International Workshop on Intelligent Control*, volume 1, pages SL9–SL17, Istanbul, Turkey, August 1990.

[24] T. Umeno and Y. Hori. Robust speed control of dc servomotors unsing modern two degrees-of-freedom controller design. *IEEE Transaction on Industrial Electronics*, 38(5):363–368, October 1991.

[25] H-S. Lee and M. Tomizuka. Robust digital tracking controllers for high-accuracy positioning system. *IEEE Transaction on Industrial Electronics*, 43(1):48–55, February 1996.

[26] B. Yao, M. Al-Majed, and M. Tomizuka. High performance robust motion control of machine tools: an adaptive robust control approach and comparative experiments. *IEEE/ASME Trans. on Mechatronics*, 2(2):63–76, June 1997.

[27] C. Smith and M. Tomizuka. Shock rejection for repetitive control using a disturbance observer. In *Proceedings of the 35th IEEE Conference of Decision and Control*, pages 2503–2504, Kobe, Japan, December 1996.

[28] T. Nagata and M. Tomizuka. Robust engine torque control by discrete event disturbance observer. In *Proceedings of the 17th World Congress of the International Federation of Automatic Control (IFAO'08)*, pages 9473–9478, Seoul, Korea, July 2008.

[29] E.R. Burke (editor). *High-tech cycling*. Human Kinetics Publishers, 2003.

[30] C. Durney, H. Massoudi, and M. Iskander. *Radiofrequency radiation dosimetry handbook, 4th edition*.

[31] Y. Chen, K. Moore, J. Yu, and T. Zhang. Iterative learning control and repetitive control in hard disk drive industry - a tutorial. In *Proceedings of the 2006 IEEE International Conference on Decision and Control (CDC)*, pages 1–15, San Diego, CA, USA, December 2006.

[32] N. O. Perez Arancibia, C.-Y. Lin, T.-C. Tsao, and S. Gibson. Adaptive-repetitive control of a hard disk drive. In *Proceedings of the 46th IEEE Conference on De-*

cision and Control (CDC), pages 4519–4524, New Orleans, LA, USA, December 2007.

[33] J.-H. Moon, M.-N. Lee, and M. J. Chung. Repetitive control for the track-following servo system of an optical disk drive. *IEEE Transaction on Control Systems Technology*, 6(5):663–670, September 1998.

[34] R. Hanson and T.-C. Tsao. Periodic sampling interval repetitive control and its application to variable spindle speed noncircular turning process. *ASME Journal of Dynamic Systems, Measurement, and Control*, 122.

[35] B. Francis and W. Wonham. The internal model principle for linear multivariable regulators. *Journal of Applied Mathematics and Optimization*, 2.

[36] M. Tomizuka. Me233: advanced control systems class notes.

[37] F. Whitt and D. Wilson. *Bicycling science*. The MIT Press, 1982.